UNIVERSITY OF CALIFORNIA, SAN DIEGO

Electrophoretic Deposition of Highly Efficient Phosphors for White Solid State Lighting using near UV-Emitting LEDs

A dissertation submitted in partial satisfaction of the
requirements for the degree Doctor of Philosophy

in

Materials Science and Engineering

by

Jae Ik Choi

Committee in charge:

Professor Joanna McKittrick, Chair
Professor Jan B. Talbot, Co-Chair
Professor Sungho Jin
Professor Shirley Meng
Professor Deli Wang

2014

The dissertation of Jae Ik Choi is approved, and it is acceptable in quality and form for publication on microfilm and electronically:

Chair

University of California, San Diego

2014

DEDICATION

To my wife, Yusun, two adorable daughters, Amy and Erica, and my parents.

TABLE OF CONTENTS

LIST OF FIGURES

LIST OF TABLES

LIST OF ABBREVIATIONS

CCT	Correlated Colour Temperature
CFL	Compact Fluorescent Lamps
CIE	Commission Internationale de l'Eclairage
CRI	Color Rendering Index
CRT	Cathode Ray Tube
DOE	the U.S. Department of energy
EQE	External Quantum Efficiency
IQE	Internal Quantum Efficiency
HID	High Density Discharge Lamps
LCD	Liquid Crystal Display
LED	Light Emitting Diode
lm	Luminous flux
lm/W	Luminous Efficacy (lumen/watt)
nUV	Near ultraviolet (380-410 nm)
pcLED	Phosphor Converted Light Emitting Diode
PL	Photoluminescence
QE	Quantum Efficiency
RE	Rare Earth Elements
RGB	Red, green, and blue color
RT	Room Temperature
SEM	Scanning electron microscopy
SSL	Solid state lighting
TEM	Transmission electron microscopy
UV	Ultraviolet
XRD	X-ray Diffraction
YAG:Ce	$Y_3Al_5O_{12}:Ce^{3+}$

ACKNOWLEDGEMENTS

First of all, I would like to thank to my advisor, Professor Joanna McKittrick, for her continuous good advice and support throughout the research. I would also like to thank my co-advisor, Professor Jan B. Talbot for her good advice and enthusiasm for this research. This work was supported by the U.S. Department of Energy of Grant DE-EE0002003. I would like to express my special thanks to the members at OSRAM SYLVANIA Central research, Dr. Kailash Mishra, Mark Hannah, Alan Piquette, and Maria Anc for their help throughout the project. I am grateful to the other members of my Ph.D. committee: Prof. Sungho Jin, Prof. Deli Wang, and Prof. Shirley Meng for serving as members of my committee.

Additional thanks are extended to Professor. Gustaf Arrhenius for the assistance and insightful discussion regarding X-ray diffraction, as well as Ryan Anderson for the assistance on Scanning Electron Microscopy and Esther Sluzky for the assistance on EPD bath set-up.

I would like to thank to the previous group member, Dr. Jinkyu Han who is now working at Brookhaven National Laboratory and undergraduate research assistant, Seung-hyo Lee who helped me during the project.

Chapter 5, in full, is a reprint of the material as it will appear in Materials Characterization, Seung-hyo Lee, Jae Ik Choi, Jinkyu Han, Youngjin Kim, Jan B. Talbot, and Joanna McKittrick. The dissertation author contributed the synthesis of the phosphors and characterization.

Chapter 6, in full, is a reprint of the material as it appears in Key Engineering Materials, Jae Ik Choi, Esther Sluzky, Maria Anc, Alan Piquette, Mark. E. Hannah, Kailash C. Mishra, Joanna McKittrick, and Jan B. Talbot, Vol. 507, pp. 149-153 (2012). The dissertation author contributed the experiment of electrophoretic deposition and figure formatting.

Chapter 7, in full, is a reprint of the material as it appears in the Electrochemical Society Journal of Solid State Science and Technology, Jae Ik Choi, Maria Anc, Alan Piquette, Mark. E.

Hannah, Kailash C. Mishra, Joanna McKittrick, and Jan B. Talbot, Vol. 2(7), pp. R153-R159 (2013). The dissertation author was the primary author of this paper.

Chapter 8, in full, is a reprint of the material as it appears in Journal of The Electrochemical Society, Jae Ik Choi, Maria Anc, Alan Piquette, Mark. E. Hannah, Kailash C. Mishra, Jan B. Talbot, and Joanna McKittrick, Vol. 161(3), pp. D111-D117 (2014). The dissertation author was the primary author of this paper.

VITA

2000	Bachelor of Science. Pusan National University, Pusan, South Korea
2002	Master of Science, Korea Advanced Institute of Science and Technology, Daejeon, South Korea
2011	Master of Science, Georgia Institute of Technology, Atlanta, USA
2014	Doctor of Philosophy, University of California, San Diego, USA

Publications

J.I. Choi, E. Sluzky, M. Anc, A. Piquette, M. Hannah, K.C. Mishra, J. McKittrick and J.B. Talbot, "EPD of Phosphors for Display and Solid State Lighting Technologies" Key Engineering Materials Vol. 507, pp 149-153 (2012)

J. McKittrick, J.K. Han, J.I. Choi and J.B. Talbot, "Effect of powder synthesis and processing on luminescence properties," in TMS Proceedings, Materials Processing and Interfaces, eds. K. Morsi, F.D.S. Marquis, J.L. Meyer and A. El-Desouky, John Wiley & Sons, 1, 497-504 (2012). (invited)

J.I. Choi, M. Anc, A. Piquette, M. Hannah, K.C. Mishra, J. McKittrick and J.B. Talbot, "Electrophoretic deposition of phosphors for white solid state lighting using near UV-emitting LEDs" The Electrochemical Society Journal of Solid State Science and Technology Vol. 2(7), pp. R153-R159 (2013)

J.K. Han, J.I. Choi, A. Piquette, M. Hannah, M. Anc, M. Galvez, J. B Talbot and J. McKittrick, "Phosphor Development and Integration for Near-UV LED Solid State Lighting" ECS Journal of Solid State Science and Technology Vol. 2(2), R3138-R3147 (2013)

J. McKittrick, M. Hannah, A. Piquette, J.K. Han, J.I. Choi, M. Anc, M. Galvez, H. Lugauer, J. B. Talbot and K. C. Mishra "Phosphor Selection Considerations for Near-UV LED Solid State Lighting" ECS Journal of Solid State Science and Technology Vol. 2(2), R3119-R3131 (2013)

J.I. Choi, M. Anc, A. Piquette, M. Hannah, K.C. Mishra, J.B. Talbot, and J. McKittrick, "Electrophoretic deposition of nano- and micron-sized $Ba_2SiO_4:Eu^{2+}$ phosphor particle*s*" The Electrochemical Society Vol 161(3), D111-D117 (2014)

S. Lee, J.I. Choi, J.K. Han, Y. Kim, J. B. Talbot, and J. McKittrick, "Comparison of luminescent properties of $Y_2O_3:Eu^{3+}$ and $LaPO_4:Ce^{3+}$, Tb^{3+} phosphors prepared by various synthetic methods" (submitted)

Presentation and posters

J. Talbot, J.I. Choi, E. Sluzky, M. Anc, A. Piquette, M. Hannah, K.C. Mishra and J. McKittrick, "EPD of phosphors for display and solid state lighting technologies", 4th International Conference on Electrophoretic Deposition: Fundamentals and Applications, Oct 2-7, 2011, Puerto Vallarta, Mexico. (keynote address)

J.I. Choi, E. Sluzky, M. Anc, A. Piquette, M. Hannah, K.C. Mishra, J. McKittrick and J. Talbot, "Electrophoretic deposition of phosphors for UV-emitting LEDs", 220th Electrochemical Society Meeting, Oct 9-14, 2011, Boston, MA.

J.I. Choi, G.A. Hirata, M. Hannah, A. Piquette, M. Anc, J. Talbot, K.C. Mishra, and J. McKittrick, "Silicon-based nitride red phosphors for white light emitting diodes (LEDs)", 220th Electrochemical Society Meeting, Oct 9-14, 2011, Boston, MA.

J. Talbot, J.K. Han, J.I. Choi and J. McKittrick, "Recent developments in solid-state lighting materials," ASM Chapter Meeting, San Diego, CA, Oct. 25, 2011 (invited).

J. McKittrick, J.K. Han, J.I. Choi, J.B. Talbot, and K.C. Mishra "Effect of powder synthesis and processing on luminescence properties," in TMS Proceedings, Materials Processing and Interfaces, eds. K. Morsi, F.D.S. Marquis, J.L. Meyer and A. El-Desouky, John Wiley & Sons, 1, 497-504 (2012). (invited)

J.I. Choi, M. Anc, A. Piquette, M. Hannah, K.C. Mishra, J.Talbot and J. McKittirck, "Highly efficient phosphor-converted white light emitting diodes by electrophoretic deposition", 222nd Electrochemical Society Meeting, Oct 7-12, 2012, Honolulu, HI.

J.I. Choi, A. Piquette, M. Hannah, K.C. Mishra, J.Talbot and J. McKittirck, "Synthesis of $Sr_2Si_5N_8:Eu^{2+}$ red-emitting phosphor by induction heating", 222nd Electrochemical Society Meeting, Oct 7-12, 2012, Honolulu, HI.

J.I. Choi, M. Anc, A. Piquette, M. Hannah, K. Mishra, J. Talbot, J. McKittrick, "Comparison of Electrophoretic Deposition of Nano- and Micron-Sized $Ba_2SiO_4:Eu^{2+}$ Phosphor Particles", 224th ECS Meeting, Oct. 27-Nov. 1, 2013, San Francisco, CA.

J.K. Han, J.I. Choi, J. Lee, J. Talbot, and J. McKittrick, "Effect of Synthesis Methods On the Powder Characteristics and Luminescence Properties of Nanophosphors", 224th ECS Meeting, Oct. 27-Nov. 1, 2013, San Francisco, CA.

J. McKittrick, J.K. Han, J.I. Choi, M. Hannah, A. Piquette, M. Anc, J. Talbot, and K. Mishra, "Development of Phosphors for White Emitting Near UV LEDs", 224th ECS Meeting, Oct. 27-Nov. 1, 2013, San Francisco, CA. (invited)

ABSTRACT OF THE DISSERTATION

Electrophoretic Deposition of Highly Efficient Phosphors for White Solid State Lighting using near UV-Emitting LEDs

by

Jae Ik Choi

Doctor of Philosophy in Materials Science and Engineering

University of California, San Diego, 2014

Professor Joanna McKittrick, Chair

Professor Jan B. Talbot, Co-Chair

Electrophoretic deposition (EPD) is a method to deposit particles dispersed in a liquid onto a substrate under the force of an applied electric field, and has been applied for depositing phosphors for application in solid state lighting. The objective is to deposit phosphors in a "remote phosphor" configuration for a UV-LED-based light source for improved white light extraction efficiency. It is demonstrated that EPD can be used to deposit red-, green-, blue-, yellow- and orange-emitting phosphors to generate white light using a near UV-emitting LED by either depositing a phosphor blend or sequentially individual phosphor compositions. The phosphor coverage was excellent, demonstrating that EPD is a viable method to produce

phosphor layers for the "remote phosphor" white light design. The deposition rates of the individual phosphor films were ~1-5 μm/min. The blend depositions composed of both three and four phosphor compositions emit white light located on or near the black body locus on the CIE chromaticity diagram. Phosphor films were also prepared by sequential deposition of red/orange and green/blue compositions, to generate white light. The layered films were flipped over and illuminated in this orientation, which showed approximately the same luminescence characteristics. No change in the reabsorption ratio of green/blue emission by the red/orange phosphor was found regardless of the deposited order of the layered films. These applications of EPD of phosphor for white solid state lighting are promising and effective due to easy tuning of emissive color by varying the phosphor blend compositions.

Although nanoparticles of a variety of materials have been coated by EPD, there have been few direct comparisons of EPD of nano- and micron-sized particles of the same material. Another field of the study was to compare EPD of nano-, nano core/SiO_2 shell and micron-sized $(Ba_{0.97}Eu_{0.03})_2SiO_4$ phosphor particles for application in a near-UV LED-based light source. EPD from an amyl alcohol bath was able to produce uniform films for all particle sizes, whereas uniform films were produced only of micron-sized particles in an isopropyl alcohol bath. A new equation was developed for predicting the deposited mass, considering the change in concentration of particles in the bath from both settling and deposition, showed good agreement with the experimental values.

Chapter 1. Introduction

It is estimated that lighting accounts for 22% of the total US electrical energy use and 7% of the global primary energy expenditure. From the latest available data from the U. S. Department of Energy (DOE), it showed that more than 70 % of electricity used for total lighting is for commercial and residential lighting with 85 % of residential lighting using incandescent lights and fluorescent lamps, as shown in Figure 1.1. [1]. Since most of the energy used for the incandescent lamp is wasted as infrared radiation and mercury in the fluorescent lamps can cause environmental problems, there have been long efforts to improve the efficacy of the technology, as well as developing a more energy efficient light and environmental source to replace incandescent and fluorescent lighting [2].

The beginning of modern lighting technology is generally attributed to the invention of the incandescent lamp by Sir Thomas Edison in 1878 [3]. The color of light produced by a heated metal filament in an incandescent lamp appears close to that of the sun, to which the human eye has been adapted [4]. Objects illuminated under an incandescent light would appear to have a natural color. To determine the "quality" of a light source, one parameter called the color rendering index (CRI) is often used. This index, with a scale of 0 to 100, measures the ability of the light source to accurately display the color of an object compared to a standard illuminant [4]. The incandescent light has a high CRI of about 100, while low pressure sodium lamps have CRI of about 18 [4]. However, about 95% of the electricity used by a typical incandescent light bulb is wasted as heat and infrared radiation, which results in a low luminous efficiency of ~12 lumens per watt (lm/W) [4]. With a tungsten-halogen cycle, halogen incandescent lamps have longer filament lifetimes as the filament evaporation rate is reduced. This also allows the halogen lamps to be at full brightness for longer time and have a comparable CRI relative to the traditional incandescent lamps, resulting in more than twice the efficiency (~30 lm/W) [4]. Unlike

incandescent lamps that generate light via black body radiation of a solid metal at high temperature, gas discharge lamps operate by exciting the inert gas molecules and metal vapor enclosed within the lamp. Fluorescent lamps, low-pressure sodium, mercury, or high pressure metal-halide lamps are all examples of gas discharge lamps with increased efficacy, ~40 lm/W and above, compared to incandescent lamps [4]. These lamps are filled with inert gases and metal vapors, which are excited by electrons emitted by a cathode. Upon returning to the ground state, the excited gas atoms or plasma will emit light that correlate to their discrete excitation energy. This results in separated spectral lines instead of a continuous spectrum like an incandescent lamp. Without a continuous spectrum, gas discharge lamps typically render colors more poorly than incandescent lamps, with a CRI value between 0 and 86 [4]. For example, low pressure sodium lamps have resonance emission lines of sodium around 590 nm, a yellow color. Therefore, the true color of objects cannot be determined under the monochromatic light. Nevertheless, contrast and movement can be perceived faster than with other white light sources. Coupled with its high efficacy (>100 lm/W), low pressure sodium lamps are now mainly used for outdoor and street lighting. The fluorescent lamp is a low pressure mercury discharge lamp, in which the resonance lines are in the UV range (185.0 nm and 253.7 nm). To achieve emission in the visible spectrum, a three-band phosphor is used as a coating, which can be excited to the approximate color rendering to that of the “white light” from incandescent lamps. In high pressure or high intensity discharge (HID) lamps, the spectral lines are generally broader and improve color rendering. The incorporation of various metal-halide salts can further improve the luminous efficacy and color rendering, similar to phosphors that are used for fluorescent lamps [4].

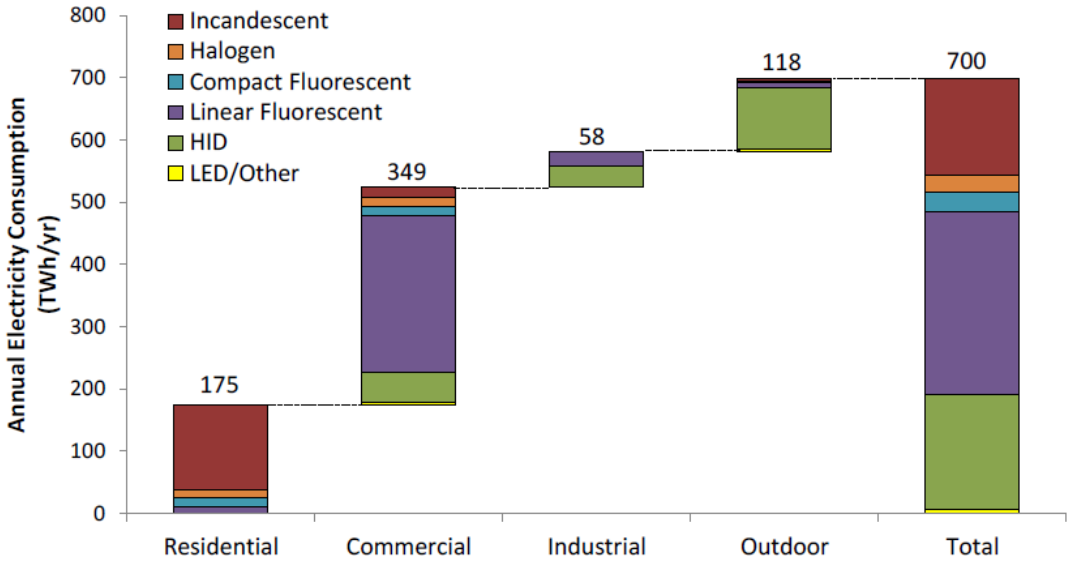

Figure 1.1. Annual energy consumption broken down by sectors and lighting technology [1].

Recently, light emitting diodes (LEDs) have been receiving much attention due to their application as a general illumination light source [5]. Based on wide band gap semiconductors, the active layer of an LED will release photons corresponding to the band gap energy of the semiconductor upon proper excitation. Emissions lines from LEDs are also narrow and discrete, like the emission from gas atoms in a fluorescent lamp. Research on white LEDs is advancing in many respects. For the purpose of general illumination, factors such as reliability, efficiency, color temperature and color rendering are all important considerations for LEDs. Current research is very active on new designs for the LED structure and packaging to improve the light extraction efficiency and reliability of the device, as well as on novel phosphor materials for use in LEDs to improve color rendering. As efficiencies of LEDs continue to improve, the possible applications for LEDs also extend from the traditional small scale indicator lighting and traffic lights, to using white LEDs for automotive headlights, and even general illumination for homes, offices and industries [5, 6].

The goal of this research is to deposit phosphors in a "remote phosphor" configuration for a UV-LED-based light source for improved white light extraction efficiency. Electrophoretic deposition method was used to deposit red-, green-, blue-, yellow- and orange-emitting phosphors to generate white light using a near UV-emitting LED by either depositing a phosphor blend or sequentially individual phosphor compositions. Also, EPD of nano- and micron-sized particles of the same material was compared since there have been few direct comparisons between them. EPD of nano-, nano core/SiO_2 shell and micron-sized $(Ba_{0.97}Eu_{0.03})_2SiO_4$ phosphor particles was evaluated for application in a near-UV LED-based light source. A new equation was developed for predicting the deposited mass, considering the change in concentration of particles in the bath from both settling and deposition

The dissertation is organized as follows: Chapter 2 gives a background on solid state lighting and reviews on the lighting terminology and advantages of near UV LED to generate

white light. Chapter 3 contains an overview of electrophoretic deposition, parameters influencing the process and kinetics and equations of electrophoretic deposition. Chapter 4 details the experimental to prepare phosphor powders with various synthetic methods and the set-up for EPD. Chapter 5 details the morphology and particle size dependent properties of $Y_2O_3:Eu^{3+}$ and $LaPO_4:Ce^{3+}$ phosphors prepared by various synthetic methods. Chapter 6 discusses the EPD of phosphors for display and solid state lighting technologies. Chapter 7 details the electrophoretic deposition of phosphors for white solid state lighting using near UV-emitting LEDs. Chapter 8 compares the electrophoretic deposition of nano- and micron-sized $Ba_2SiO_4:Eu^{2+}$ phosphor particles. Chapters 5, 6, 7, and 8 contain material that has already been published or submitted for publication. Conclusions and recommendations for future work are presented in Chapter 9.

References

1. 2010 U.S. Lighting Market Characterization. Prepared by Navigant Consulting, Inc. for the Department of Energy. Washington D.C. January 2012.

2. J. M. Phillips, Basic Research Needs for Solid-State Lighting: Report of the Basic Sciences Workshop on Solid-State Lighting, Department of Energy Office of Basic Energy Sciences (2006).

3. 2012 K. Nassau, The Physics and Chemistry of Color: The Fifteen Causes of Color, John Wiley & Sons, Inc. (2001).

4. P. Flesch, Light and Light Sources: High-intensity Discharge Lamps, Springer-Verlag, Berlin (2006).

5. E. F. Schubert, "History of Light Emitting Diodes," in Light-emitting Diodes, Cambridge University Press, New York (2006).

6. E. F. Schubert, "White-light Sources Based on LEDs," in Light-emitting Diodes, Cambridge University Press, New York (2006).

Chapter 2. Background and motivation

2.1. Solid state lighting

Since the first demonstration of a practical visible spectrum LED almost 50 years ago by Holonyak and Bevacqua [1], LED technology has been used in simple displays and indicator lamps producing red and green emissions, but also blue and, most important, white. This was possible by the development of the InGaN material system, which was made possible after major breakthroughs in materials technology by Amano in the late 1980s [2]. In 1993, Shuji Nakmura at Nichia Chemical developed the first commercial blue LEDs and white-emitting solid state lighting (SSL) products in combination with a well-known yellow-emitting phosphor YAG:Ce [3]. The LED color ranges depending on the composition of semiconductor as shown in Figure 2.1. [3].

With the potential for much longer lifetimes and lower energy consumption as compared to current lighting technologies, the use of LEDs, has become a promising technology in the lighting industry. U.S. consumers could save ~$42 billion by the year 2025 if new technologies can be adapted that improve energy efficiency by 50% (relative to the 5% efficiency of the incandescent light bulb). This also translates to saving 70 gigawatts of power, which is equivalent to the power generated by 70 one-GW nuclear power plants [4]. A report issued by DOE lists major categories of lighting (incandescent, halogen, fluorescent lights, high intensity discharge lamps (HID)), demonstrated that white-emitting LEDs surpasses the conventional lighting technologies (including incandescent and fluorescent light sources) in energy efficiency, lifetime, and environmental issues as shown in Table 2.1. [5].

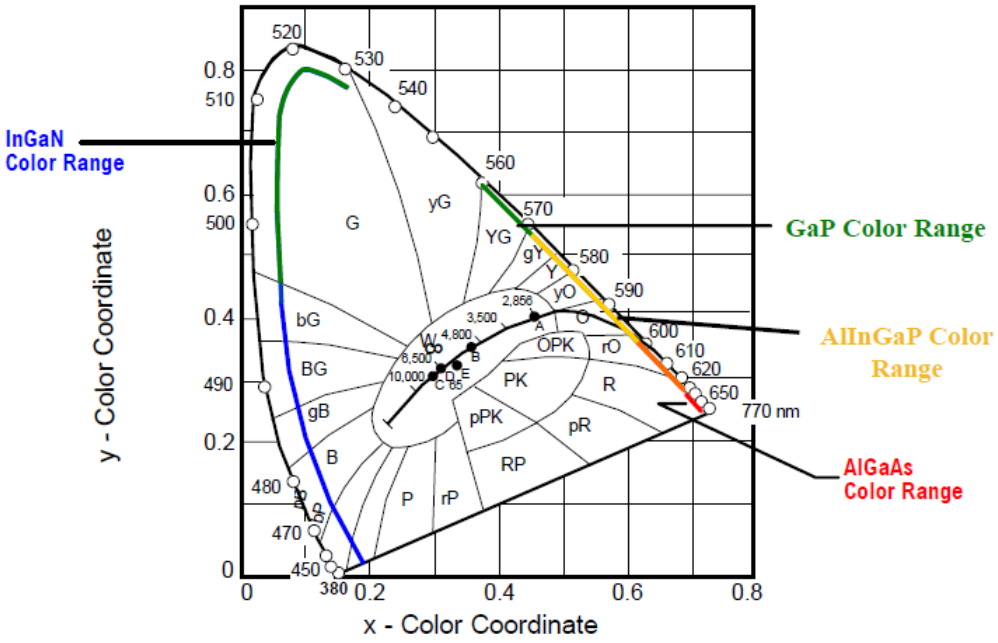

Figure 2.1. Color ranges of LEDs depending on the semiconductor compositions [3].

Table 2.1. Comparison of energy efficiency, luminous efficacy (lumen/watt), lifetime, heat and presence of mercury of commonly available light sources [5].

	Incandescent	Halogen	Compact fluorescent	High intensity discharge	LED
Energy efficiency	Very low	Low	High	High	Very High
Luminous efficacy (Lumen/Watt)	14	24	60-100	65-110	80-140
Lifetime (hours)	1000	2000-3000	6000-10000	20000	50000
Heat	Yes++	Yes++	Yes	Yes	No
Mercury	No	No	Yes	Yes	No

There are two SSL designs that utilize phosphors for white light generation, a blue emitting InGaN chip with yellow emitting phosphor or a near-UV chip with tri- or quadru-blend phosphors. However, blue-emitting LEDs have significant binning problems (lamp to lamp variation for the LED package) and light output increases linearly with increasing driving current, which causes a change in white emission quality. Additionally, the most critical problem for using blue emitting LEDs is the significant current droop at high current, which decreases the internal quantum efficiency (IQE).

During the last few years, hybrid SSL sources using LED dies capable of emitting in the blue (450 nm) or ultraviolet (380-400 nm) region have provided a promising, alternative way of generating white light for general lighting application. Several lighting companies have chosen this approach in preference to color blending with red, green and blue LEDs. In order to build white light sources that excel fluorescent lighting in energy performance and color quality, revolutionary improvements are necessary both in the performance of LED dies to convert electrical energy to visible energy and of phosphors to generate efficaciously visible light with the flexibility to blend these phosphors to generate light sources with the desired efficacy, color rendering index (CRI) and correlated color temperature (CCT).

The basic construction of an LED is a semiconductor p-n junction as shown in Figure 2.2. [6]. The n-type layer uses electron as the majority charge carrier, whereas the p-type layer uses holes as the majority charge carrier. The anode of the LED is connected to a positive terminal and the cathode is connected to a negative terminal, like a conventional diode under forward bias [7]. As a result, electrons in the n-type layer will be repelled toward the depletion zone of the p-n junction, and tunnel through to the p-type layer. Similarly, holes in the p-type layer will be repelled toward the depletion zone and tunnel through to the n-type layer. Then, the movement of these charge carriers under forward bias in the p-n junction produces current flow and voltage drop, providing the necessary power to operate an LED. Typical operating range for an LED is

around 10 – 30 mA and 1.5 – 3 V [8]. As the electrons cross the p-n junction and recombine with holes in the p-type layer, they fall into a lower energy state and releases photons, or light, corresponding to the band gap between the p-type and n-type semiconductor.

The white-emitting LED product, which includes the LED chip, phosphors and the reflector cup for the improvement of efficiency and electrical contacts, is typically encased in an epoxy resin designed for the specific application as shown in Figure 2.3. (a). The chip is soldered to a lead wire serving as the cathode at the bottom of a reflector cup, and the top metal contact is connected to another lead wire serving as the anode. The placement and arrangement of phosphors are crucial for the efficiency of white-emitting LEDs. Phosphor arrangements in white-emitting LEDs are illustrated in Figure 2.3. (b) and (c). Figure 2.3. (b) shows a uniform distribution of phosphor within the reflector cup. The uniform distribution of phosphor limits the efficiency since a large portion of light emitted by the phosphors directly impinges on the LED chip where it can be re-absorbed. If the phosphor is placed at a sufficiently large distance from the LED chip (remote phosphor configuration as shown in Figure 2.3. (c)), the probability of a light ray emanating from the phosphor and directly hitting the low reflectivity LED chip is small, improving the light extraction efficiency. Another advantage of this remote phosphor configuration is that it can reduce the operating temperature of the phosphor. The quantum efficiency of the phosphor tends to decrease with increasing operating temperature. Figure 2.3. (d) shows a commercial blue LED configuration.

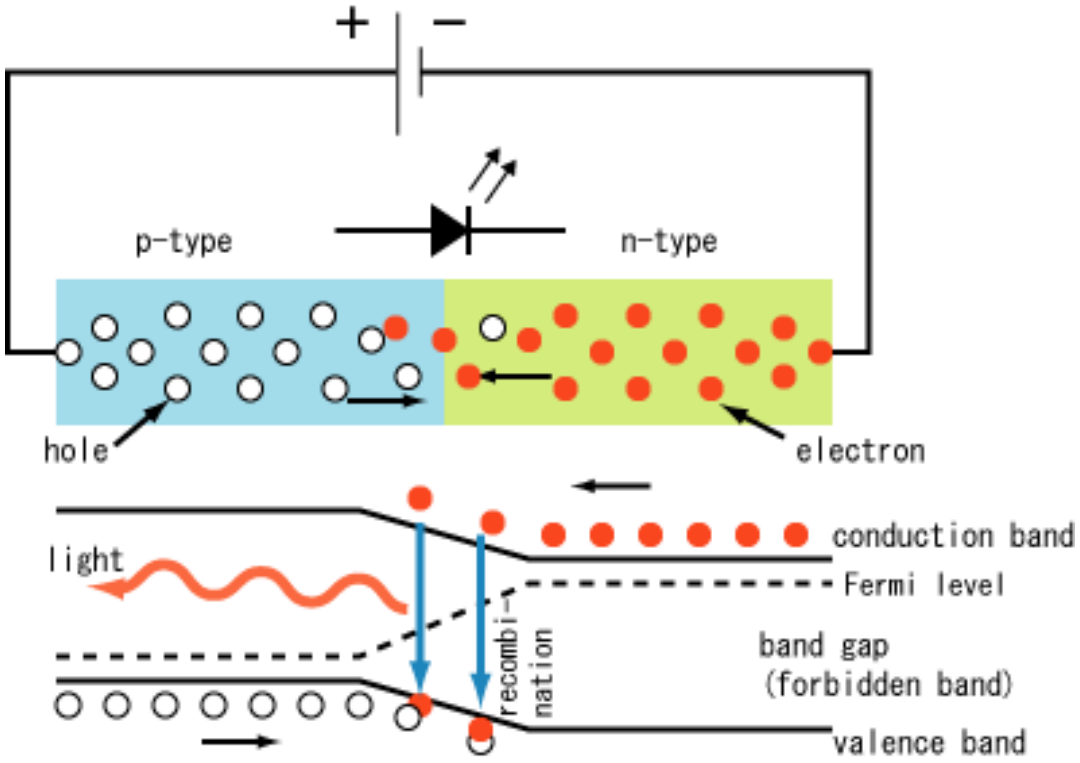

Figure 2.2. Schematics of p-n junction for light emitting diode [6].

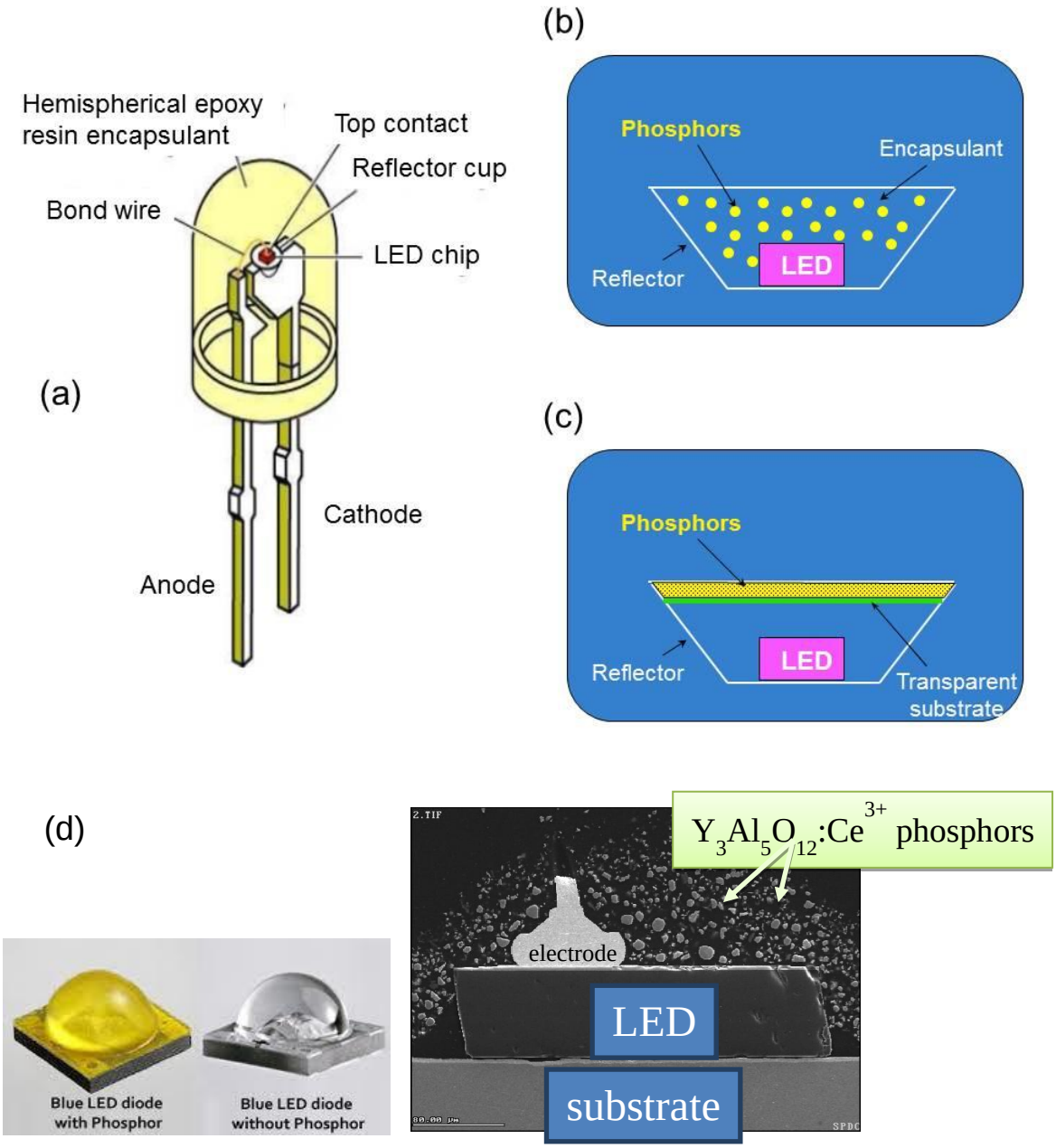

Figure 2.3. LED design and the phosphor package in white LED. (a) Typical LED lamp package. (b) Uniform phosphor distribution directly in reflector cup. (c) Remote phosphor distribution in the package. (d) Commercial blue LED configuration [9].

2.2. White light generation

2.2.1. Basic photometric quantities.

Luminous flux (lm): The luminous flux is the photometric equivalent of the radiant flux in radiometry. It describes the total "light energy" emitted by a light source per unit time as perceived by the human eye. The units for the luminous flux are lumen (lm).

Luminous efficacy (lm/W): The luminous efficacy of radiation describes how well a given quantity of electromagnetic radiation from a source produces visible light: the ratio of luminous flux (lm) to radiant flux (W) and is also determined by the eye sensitivity over the spectral distribution of light having units of lm/W [10]. This indicates the overall luminous efficacy of a source is the product of how well it converts energy to electromagnetic radiation, and how well the emitted radiation is detected by the human eye.

Luminous efficiency (%): the luminous flux has the same units as radiant flux. The luminous efficacy of radiation is then dimensionless. In this case, it is often instead called luminous efficiency, and may be expressed as a percentage. A common choice is to choose units such that the maximum possible efficacy corresponds to an efficiency of 100%. The distinction between *efficacy* and *efficiency* is not always carefully maintained in published sources, so it is not uncommon to see "efficiencies" expressed in lumens per watt, or "efficacies" expressed as a percentage [10].

Color rendering index: The color rendering index (CRI) is a quantitative measure of the ability of a light source to reproduce the colors of various objects in comparison with an ideal or natural light source and has been in wide use in the lighting industry for many years. To get the quantitative value, R_i is defined as the special color rendering index for each color sample and can be calculated using

$$R_i = 100 - 4.6\Delta E_i \quad (1)$$

The R_i value is an indication of color rendering index for each particular color and E_i value is the color difference between these color samples and fourteen reference samples of various colors given by Munsell [11]. The general color rendering index R_a, is given as the average of R_i for the first eight color samples that have medium color saturation. With the maximum value of 100, R_a gives a scale that matches well with the visual impression of color rendering of illuminated scenes. In general, incandescent lamp and daylight is used as the base reference of 100 CRI. Compact fluorescent lamps are graded at 82-86 CRI, which is considered as high quality. CRI is a more important consideration for retail lighting design than it is for office lighting. Any CRI rating of 80 or above is considered as high value and indicates that the source has good color properties. CRI of some conventional light sources are listed in Table 2.2. [12].

Table 2.2. Color rendering index of some light sources [12]

	R_a
Daylight	100
Incandescent/halogen Bulb	100
Cool White Fluorescent	57
Warm White Fluorescent	51
Cool White Deluxe	89
Warm White Deluxe	73
Metal Halide	85
Clear Mercury Vapor	18
Coated Mercury Vapor	49
High Pressure Sodium	24

2.2.2. Quantification of color and color mixing.

Within the region of visible light, the colors can be further specified via the 1931 chromaticity diagram, or the CIE *x*, *y* diagram [13], shown in Figure 2.4. [14]. In the study of color perception, one of the first mathematically defined color spaces is the International Commission on Illumination (CIE) 1931 *XYZ* color space, created by the CIE in 1931 [15, 16]. The CIE color space was derived from a series of experiments done in the late 1920s by William David Wright [17] and John Guild [18]. Their experimental results were combined into the specification of the CIE red, green and blue (RGB) color space, from which the CIE *XYZ* color space was derived. A color space is a three dimensional space; that is, a color is specified by a set of three numbers (the CIE coordinates *X*, *Y*, and *Z*, for example, or other values such as hue, colorfulness, and luminance) which specify the color and brightness of a particular homogeneous visual stimulus. A chromaticity is a color projected into a two dimensional space that ignores brightness. For example, the standard CIE *XYZ* color space projects directly to the corresponding chromaticity space specified by the two chromaticity coordinates known as x and y, creating the familiar chromaticity diagram shown in the Figure 2.4.

All colors visible to the average human eye are contained inside the diagram. The area of the white triangle in Figure 2.4. represents the gamut of color that can be matched by various combinations of red, green, and blue used in color monitors. In color theory, the gamut of a device or process is the portion of the color space that can be represented, or reproduced. The corners of the triangle are the primary colors for this gamut and the primary colors depend on the colors of the phosphors of the monitor. For example, $BaMgAl_{10}O_{17}:Eu^{2+}$ for blue emitting, $ZnSiO_4:Mn^{2+}$ for green emitting, and $Y_2O_3:Eu^{3+}$ for red emitting are widely used as color monitor phosphors and corresponds to point F, G, and H in Figure 2.4., respectively. Using these primary colors (F, G, and H points), all colors inside the triangle including white light can be achieved.

In addition to using chromaticity to define color, for incandescent black bodies, it is also possible to use the color temperature to define its color. As seen in Figure 2.4., the black body curve is in the sequence of black, red, orange, yellow, white, and blue-white, which corresponds to the increasing temperature of an incandescent object as it radiates thermally. When an object is heated to emit light that correspond to the black body curve, its temperature is defined as the color temperature. Therefore, the color temperature of an incandescent light source is the temperature of a body on the black body curve that has the same color or chromaticity on the diagram as the light source. Then, the correlated color temperature (CCT) of a light source is defined as the temperature of the body that is not on the black body curve with a color that is closest to the light source.

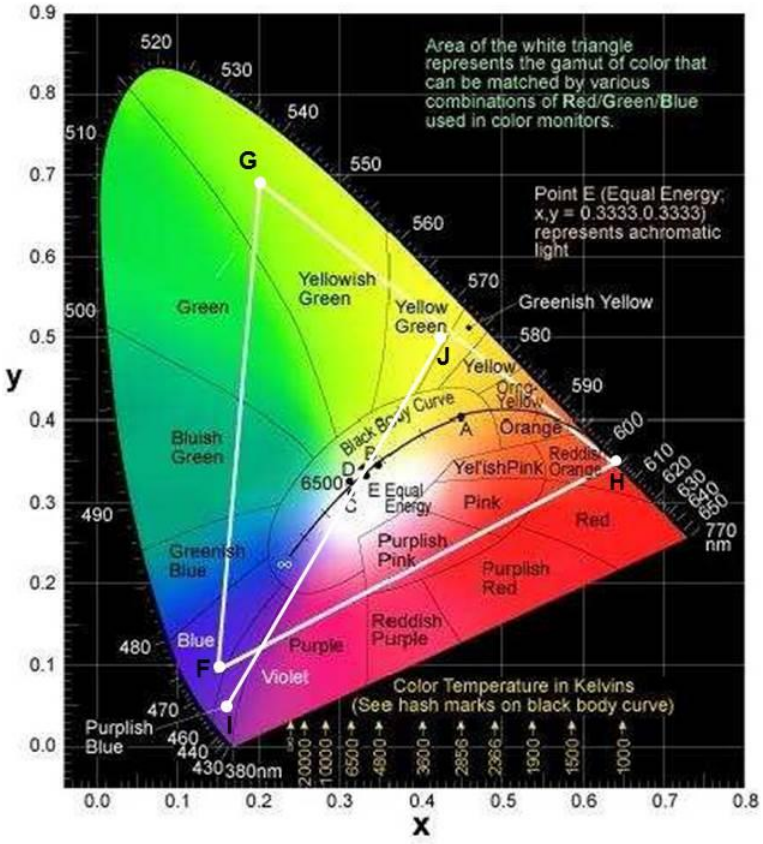

Figure 2.4. The 1931 chromaticity diagram [14]. Triangle represents primary colors used in CRT color monitors.

Typical CCT of the white region in the diagram range between 2500 and 10000 K and lamps with a CCT value below 3200 K are considered ‘warm’ sources, while those with a CCT above 4000 K are considered ‘cool’ in appearance. A warmer light is often used in public areas to promote relaxation, while cooler light is used to enhance concentration in office. Desired CCT for warm white-emitting LEDs is between 3500-4000 K and for cool white-emitting LED is near 6000-6500K [19]. CCT of some light sources are listed in Table 2.3.

Table 2.3. Color temperature of some artificial and natural light sources [19].

Temperature	Source
1,700 K	Match flame
1,850 K	Candle flame, sunset/sunrise
2,700–3,300 K	Incandescent lamps
3,000 K	Soft white compact fluorescent lamps
3,200 K	Studio lamps, photofloods,
4,100–4,150 K	Moonlight, Xenon arc lamp
5,000 K	Horizon daylight
5,000 K	Tubular fluorescent lamps or Cool White/Daylight compact fluorescent lamps (CFL)
5,500–6,000 K	Vertical daylight, electronic flash
6,500 K	Daylight, overcast
5,500–10,500 K	Liquid crystal display (LCD) screen
15,000–27,000 K	Clear blue poleward sky

2.3. Strategies to produce white light LED

For LEDs to be used for white light generation, excellent color rendering and efficacy must be taken into account. However, there is a trade-off between the two critical criteria for white light since color rendering is best achieved by a broadband spectra distributed throughout the visible region, while the efficacy is best achieved by a monochromatic radiation at 555 nm green wavelength where the human eye response reaches its maximum [20]. White light LEDs suitable for high quality lighting application can be generated in a variety of ways. Figure 2.5. shows the schematics of three kinds of approaches for white light generation, which will be discussed.

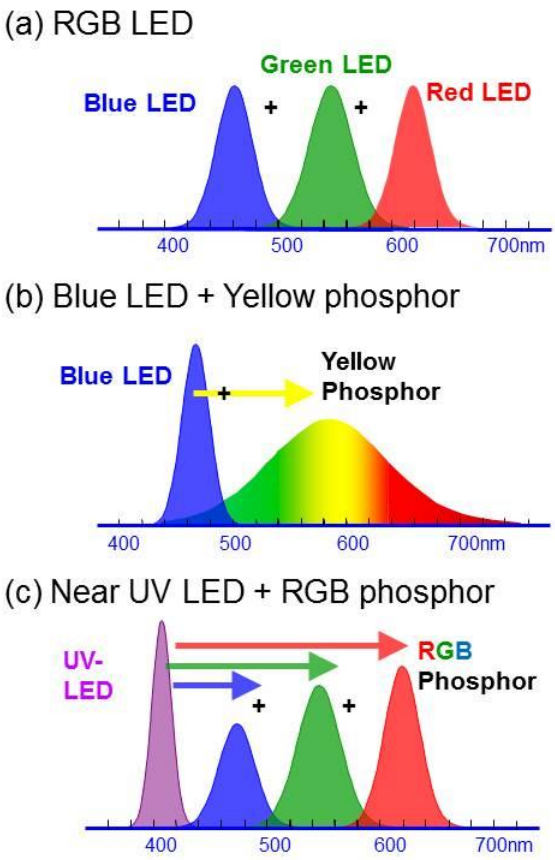

Figure 2.5. Three approaches for white light generation from (a) Blue-, green-, red-emitting LED chips, (b) blue-emitting LED chips and yellow emitting phosphors, and (c) near UV emitting LED and blue-, green-, red-emitting phosphors.

White light generation from blue-, green-, and red-emitting LED chips: White light can be formed by mixing differently colored light; the most common method is to use red, green, and blue (RGB) as shown in Figure 2.5. (a). With this approach for white light generation using currently available LEDs, the generation of white-light can have luminous efficacies of around 120 lm/W but very low color rendering capability [20]. Despite great advantages of this strategy such as excellent versatility and higher efficacies, there are potential issues with this approach: first, the light intensity of LEDs and driving voltages are very likely to vary from diode to diode (binning problem), and the task of tuning individual diodes colors is likely to be difficult. Second, these LEDs are subject to significant change in the color and intensity with variations in temperature which have detrimental effects on the quality of white light. In addition, variation in operating life of different color LEDs. For example, the light output level of AlGaAs-based LEDs (red emitting) is found to decrease by about 50% after 15,000 to 40,000 hours of operation [12]. This effect represents a serious challenge for the quality of LEDs since the white-light color rendering is critically dependent on the relative intensities of the separate red, green, and blue colors. Finally, these white-light sources are also relatively expensive since multiple LED chips are required to produce a single source of white light.

White light generation from blue-emitting LED chips and yellow-emitting phosphors: The alternative and currently commercialized method for white-light generation involves the use of a blue LED and yellow emitting phosphors. Commercially available white LEDs consist of a blue InGaN LED coated with YAG:Ce inorganic phosphor. The InGaN LED generates blue light at a peak wavelength of about 460 nm (Point I in Figure 2.4.), which excites the YAG:Ce^{3+} phosphor to emit yellow light (Point J in Figure 2.4.). The combination of the blue light from the LED and the yellow light from the YAG:Ce^{3+} results in white light. However, there are still several significant problems with this design. First, the light output is not uniform as blue light 'escapes' and is observed at the edges of the diode. Second, the CRI value is still low. As shown

in Figure 2.5. (b), there is a significant ‘gap’ between 450-550 nm where emission intensity is significantly lower than that in other spectral region. Third, the manufacturing steps are complicated since the uniformity of the powder mixture is difficult to achieve in the epoxy. However, there are many companies producing white-emitting LEDs in this way (blue-emitting chips and yellow emitting phosphor), the major ones being OSRAM-Sylvania (Germany/USA), CREE (USA), Nichia (Japan), General Electric (USA), and Philips Lumileds (USA). These LEDs are packaged and used for a variety of applications, e.g. household lighting, warehouse and factory floor lighting, street lighting, backlights for laptops and cell phones, and automotive lighting.

2.4. Advantages and the need for near UV LED solid state lighting.

Another approach is the use of a near-UV (nUV) LED source, which depends entirely on the phosphor blend to generate white light. Both blue and nUV LEDs are based on solid solutions of InN and GaN. As the InN content increases, the external quantum efficiency (EQE) of the LED chip increases accompanied by a red shift of the emitted radiation (Figure. 2.6.) [21]. The specific functional dependence of EQE on wavelength could be due to many factors including processing conditions. At wavelengths longer than 450 nm, the EQE decreases rapidly toward the green part of the spectrum, a phenomenon referred to as the “green gap” in the SSL technology.

At 400-410 nm, the InGaN chips perform as well as the blue chips at low current densities [21]. However, the real advantages of the nUV LEDs lie in less current drooping (Figure. 2.7.) and significantly less binning. In Figure 2.8., from a comparison of same generation blue and nUV LEDs, the crossover occurs at a current density of 35 A/cm^2. This improved efficiency allows the nUV LEDs to produce a greater photon density at higher currents than the blue LEDs helping to compensate for the increased Stokes loss.

In addition, there is more flexibility in the design when the blue portion of the spectrum is generated with phosphors instead of LEDs. Both phosphors and LEDs have tunable peak locations, but phosphors allow more variation in the peak width, which is important for color rendering purposes and lumen equivalence. Also, since the phosphors needed for nUV LEDs do not have to absorb blue light, it is possible to have a white-bodied phosphor blend instead of the typical yellow-orange color of blue LED phosphor blends.

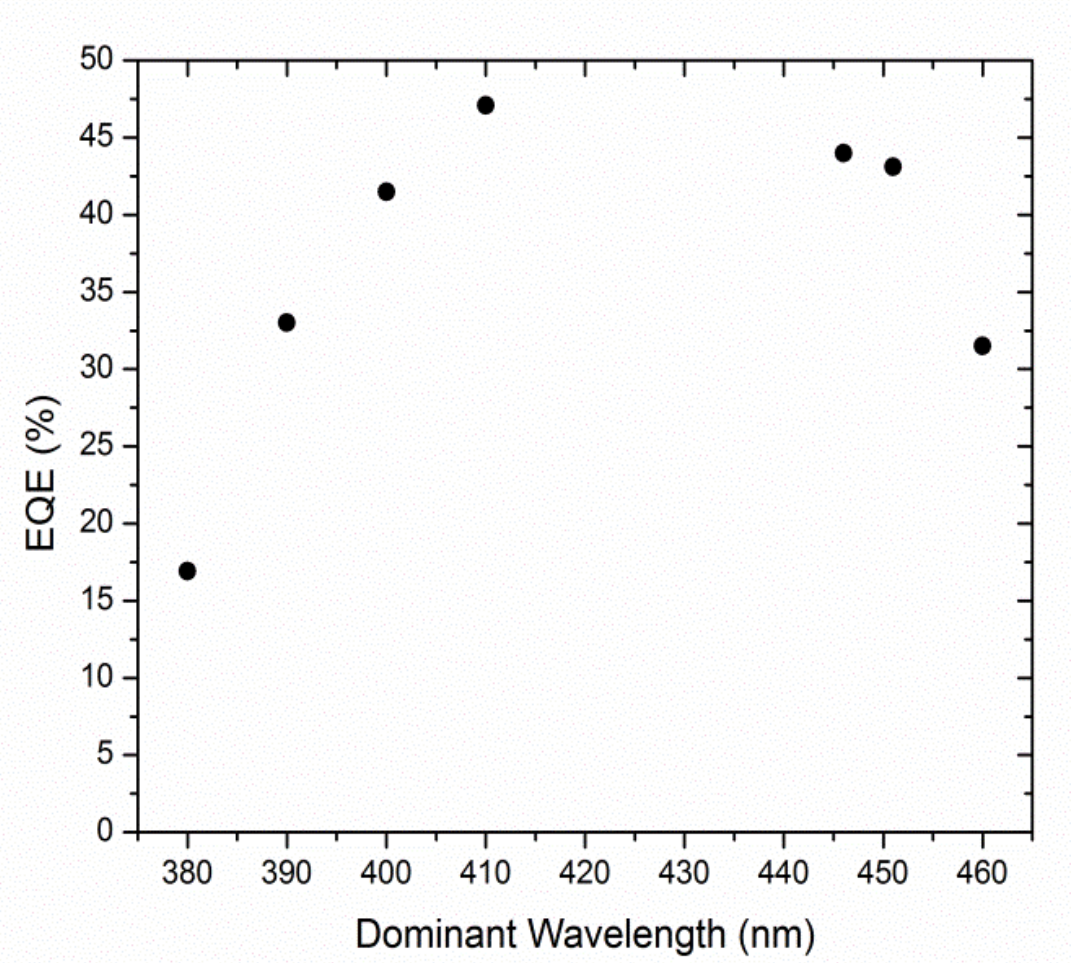

Figure 2.6. External quantum efficiency versus dominant emission wavelength for a selection of InGaN LEDs in identical packages. Each LED was driven with a current density of 35 A/cm^2 [21].

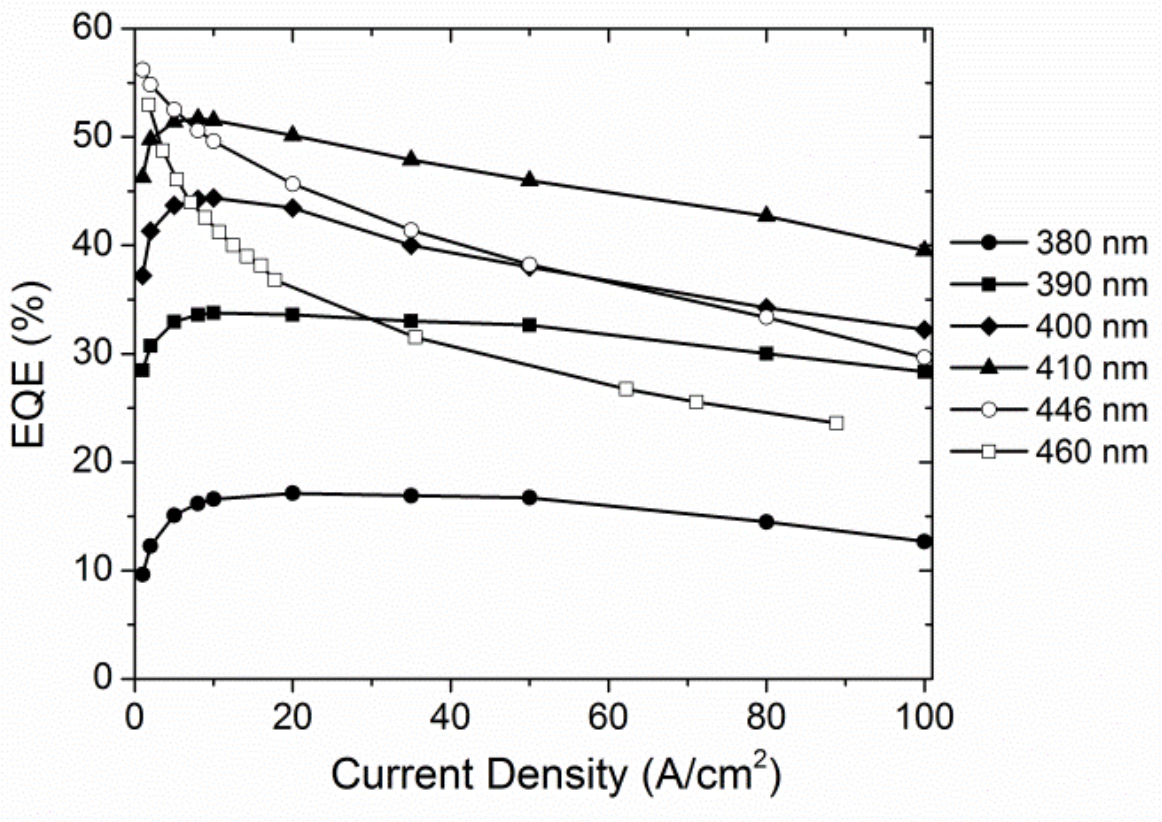

Figure 2.7. External quantum efficiency versus current density for four different nUV chips and two blue chips [21].

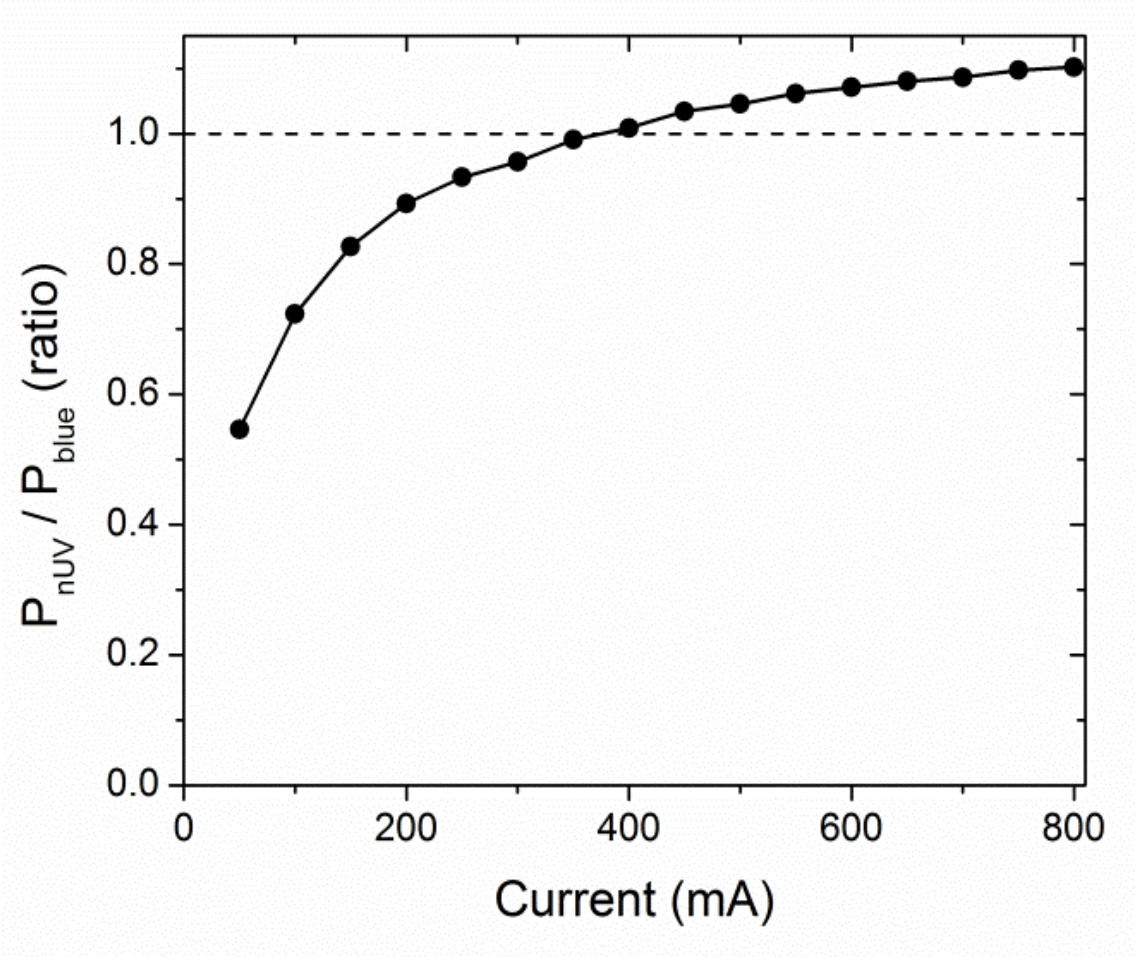

Figure 2.8. Ratio of emitted optical power for nUV (405 nm) and blue LED (450 nm) packages as a function of electrical current, based on instant-on measurements [21].

2.5. Requirement of ideal phosphors for near UV LEDs

There are several basic properties that an ideal nUV phosphor should simultaneously possess. The quantum efficiency (QE) should be as high as possible and the excitation maximum should fall in the range where nUV LED emission is most efficient (380 to 410 nm). It may not be possible to find a blue emitting phosphor that is excitable at wavelengths longer than 410 nm because of the Stokes shift requirements. However, a high QE and the location of the excitation maximum alone are not sufficient; the phosphor must have a high absorption rate in the LED emission range as well. This essentially limits phosphors utilizing transitions forbidden by Laporte's rule, such as transitions within the 4*f*- and 3*d*- manifolds. This severely restricts utilizing line emissions from the trivalent lanthanide ions, which are extensively used in the fluorescent lighting industry. The candidate phosphors are limited to those that are excited through the allowed 4f→5d, n*p*→n*d*, n*s*→n*p* transitions, and host or molecular group transitions. It is no surprise that most of the phosphors identified for nUV LEDs so far are based on Ce^{3+} and Eu^{2+} ions. In order to utilize the narrowband emissions from trivalent lanthanide ions such as Eu^{3+} or Tb^{3+}, it is necessary to explore hosts whose charge transfer transition bands are located near 400 nm (there are not many), or to use appropriate energy transfer schemes. Because of higher photon flux from LEDs, compared to fluorescent lamps, and from Stokes losses, the phosphor layers are expected to operate at elevated temperatures, which require the phosphors to have greater reduced thermal quenching. The phosphor must not degrade chemically or thermally and be free from photo-bleaching. The radiative lifetime of the activator ions should be short (ns-range) in order to reduce saturation effects and nonlinear, non-radiative recombinations due to depletion of the ground state and excited state interactions. Finally, it must be possible to manufacture the phosphor on a large scale in an economical manner. The phosphor should be non-toxic, and the fabrication, use, and disposal of the phosphor should be as environmentally benign as possible.

2.6. Nanophosphors for solid state lighting application

Integration of the phosphors into an LED package has some requirements: narrow size distribution (non-agglomerated) and chemical and thermal stability. If the phosphor particle radii are significantly less than ~400 nm of the exciting radiation (not necessarily in the quantum confinement region), these particles will negligibly scatter visible and UV radiation. This has two effects. First, Raleigh scattering is reduced, thereby increasing extraction efficiency (η_{ext}), which depends on scattering coefficient of phosphor particles and absorption of backscattered UV and visible photons from the phosphor layer by the semiconductor chip and the peripherals for electrical connections. The scattering cross-section of a particle having the complex refractive index of m = n – ik, where n is the real part and k is the extinction coefficient, can be shown to be [22]:

$$C_{scatter} = \frac{8}{3}(\pi a^2)\left(\frac{2\pi a}{\lambda}\right)^4 \left|\left(\frac{m^2-1}{m^2+2}\right)\right| \quad (2)$$

where λ represents the wavelength of radiation and a is the radius. This relationship is referred to as Rayleigh scattering. As the particle size decreases to the sub-micron regime (< 400 nm), $C_{scatter}$ approaches zero and so also does the scattering coefficient of a phosphor layer. Provided the high QE of these phosphor particles can be maintained, scattering from such a phosphor layer would be negligible. It is also clear from the above equation that $C_{scatter}$ depends on k, which increases with increasing activator concentration. This is a manifestation of the Kramer-Konig relationship of imaginary and real parts of the refractive index. Thus, one could reduce scattering by increasing activator concentration, which will also be attempted for optimizing phosphor performance. Second, it will require less phosphor to be used for converting the UV radiation to

visible since the effective path length of the UV photons in the phosphor layer will be reduced, thereby preserving our natural resources (rare earth elements).

However, phosphors in the nano-size regime have poor QE compared to phosphors in the micron-sized range [23, 24]. The reasons behind this have not investigated in a systematic way. A high concentration of surface atoms and defects at the surfaces is regarded as one of the fundamental properties of nanophosphors. They create surface charge-carrier trapping centers, which are analogous to bulk centers, but have a different energy depth. The translational symmetry breakdown and limitation of the free path of electrons by the nanoparticle size alter the selection rules, bring about new optical transitions, increase the oscillator power, and change the luminescence decay time [25]. If the nanoparticle size becomes comparable with the de Broglie wavelength or the Bohr exciton size, quantum confinement effects come into play, changing the forbidden gap width and leading to appearance of new energy levels. The interior could also have a non-uniform distribution of activators across the particle, distorted lattice planes and activators that are not located in the correct environment.

2.7. Phosphor integration

Phosphor arrangements in white-emitting LEDs are illustrated in Figure 2.9. [26]. Figure 2.9.(a) shows a conformal phosphor distribution and Figure. 2.9.(b) shows a uniform distribution of phosphor within the reflector cup, called ‘‘phosphor-in-cup.’’ The placement and arrangement of phosphors is crucial for the efficiency of white LEDs. However, the conformal and phosphor-in-cup distribution limits the efficiency of white LEDs. Since the phosphor re-emits light, a large portion of light emitted by the phosphor directly impinges on the LED chip where the light can be re-absorbed. This issue is critical in the conformal phosphor configuration due to the close proximity of the phosphor and the LED chip. If the phosphor is placed at a sufficiently large distance from the LED chip (remote phosphor configuration), the probability of a light ray

emanating from the phosphor and directly hitting the low reflectivity LED chip is small, then improving the phosphor efficiency. Another advantage of this remote phosphor configuration is that it reduces the operating temperature of the phosphor. Figure 2.9.(c) shows a remote phosphor configuration, in which a phosphor layer of uniform thickness is distributed over the reflector cup. However, there is still a large probability of a light ray being reflected by the reflector cup and being re-absorbed by the LED chip.

Therefore, a new packaging of white LEDs has been proposed as illustrated in Figure 2.9.(d). Diffuse reflectors have an angular distribution of the reflected intensity I given by $I \propto cos\theta$, where θ is the angle of reflection, irrespective of the angle of incidence. Therefore, the light is directed upward, thereby not impinging on the LED chip.

Enhancement of phosphor efficiency was reported for InGaN-based white light-emitting diodes (LEDs) employing a large separation between the primary LED emitter and the wavelength converter coupled with a diffuse reflector cup [26]. Experimental studies show that by placing the phosphor away from the die, the backscattered photons can be extracted and the efficacy can be significantly increased [27].

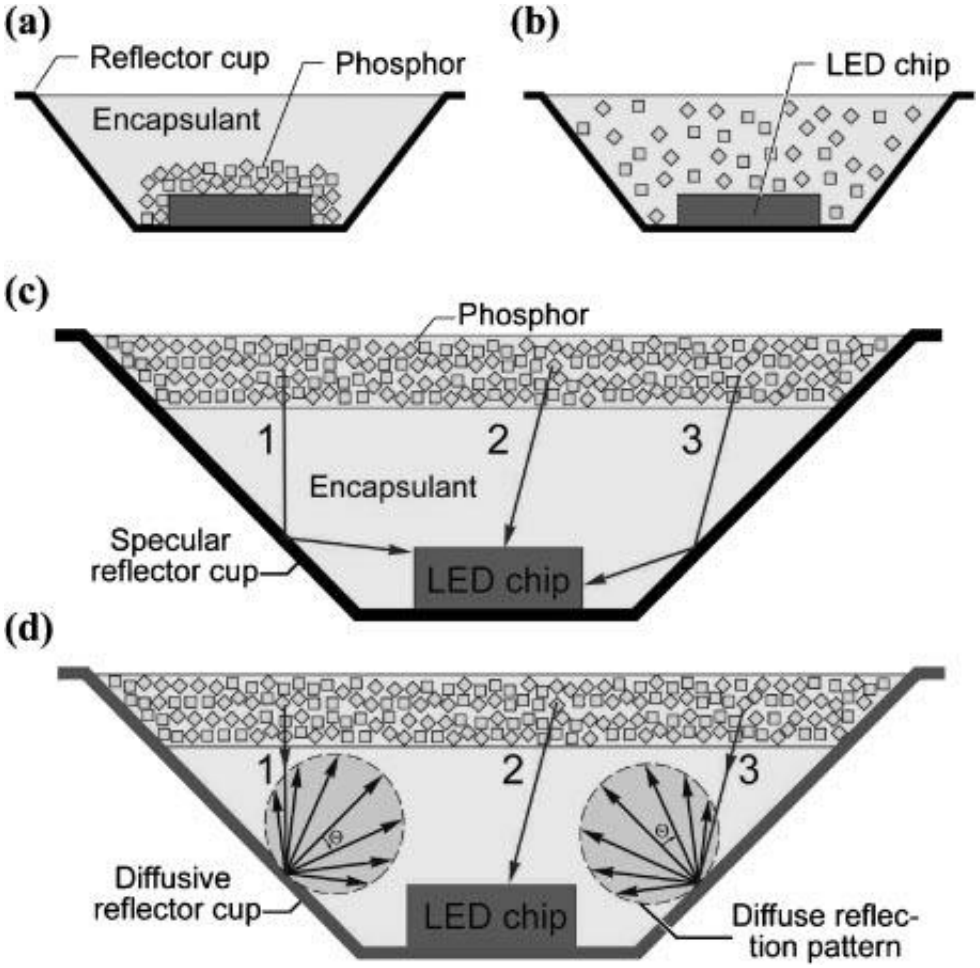

Figure 2.9. Arrangements of phosphor in white LED: (a) Conformal distribution directly on LED chip. (b) Uniform distribution in reflector cup (phosphor-in-cup). (c) Uniform distribution thin layer above LED chip (remote phosphor). (d) Remote phosphor distribution in diffuse reflector [26].

References

1. N. Jr. Holonyak, S.F. Bevaqua, “Coherent (visible) light emission from GaAs P junctions”, Appl. Phys. Lett.:82–83 2956 (1962).

2. H. Amano, N. Sawaki, I. Akasaki, Y. Toyoda. “Metalorganic vapor phase epitaxial growth of a high quality GaN film using an AlN buffer layer”. Appl. Phys. Lett. 48 353–355 (1986).

3. S. Nakamura and G. Fasol, "Applications and Markets for Gallium Nitride Light Emitting Dioes (LEDs) and Lasers," in The Blue Laser Diode: GaN Based Light Emitters and Lasers, p. 8, Springer-Verlag, Berlin (1997)

4. 2010 U.S. Lighting Market Characterization. Prepared by Navigant Consulting, Inc. for the Department of Energy. Washington D.C. January 2012.

5. 2012 Solid-state lighting research and development: Multi-Year Program Plan (2012).

6. http://en.wikipedia.org/wiki/File:PnJunction-LED-E.PNG.

7. R. Haitz, F. Kish, J. Tsao, J. Nelson, “Innovation in Semiconductor Illumination: Opportunities for National Impact” Taylor & Francis Ltd, Hoboken (1999).

8. G. Held, “Introduction to Light Emitting Diode Technology and Applications, Taylor & Francis Ltd, Hoboken (2008).

9. http://dev.emcelettronica.com/xlamp-lighting-class-leds.

10. E. F. Schubert, "High Extraction Efficiency Structures," in Light-emitting Diodes, p. 149, Cambridge University Press, New York (2006).

11. A.H. Munsell “Atlas of the Munsell Color System”, Wadsorth -Howland & Company, Malden, MA (1915).

12. E. D. Jones, “Light emitting diodes for general illumination”, OIDA report, 2001.

13. K. Nassau, “The Physics and Chemistry of Color: The Fifteen Causes of Color”, John Wiley & Sons, Inc. (2001).

14. LEDtronics, C.I.E. 1931 Chromaticity Diagram, Accessed December 21 (2009) <http://www.ledtronics.com/html/1931ChromaticityDiagram.htm>.

15. CIE. Commission internationale de l'Eclairage proceedings, 1931. Cambridge Press, Cambridge (1932).

16. T. Smith, J. Guild, "The C.I.E. colorimetric standards and their use". Transactions of the Optical Society 33, 73–134 (1931).

17. W.D. Wright, "A re-determination of the trichromatic coefficients of the spectral colours". Transactions of the Optical Society 30 141–164 (1928)

18. J. Guild, "The colorimetric properties of the spectrum". Philosophical Transactions of the Royal Society of London (Philosophical Transactions of the Royal Society of London. Series A, Containing Papers of a Mathematical or Physical Character, 230 149–187 (1931).

19. http://en.wikipedia.org/wiki/Color_temperature.

20. I. Moreno, U. Contreras. "Color distribution from multicolor LED arrays". Optics Express 15, 3607–3618 (2007).

21. J. McKittrick, M.E. Hannah, A. Piquette, J.K. Han, J.I. Choi, M. Anc, M. Galvez, H. Lugauer, J.B. Talbot, K.C. Mishra, "Phosphor Selection Considerations for Near-UV LED Solid State Lighting", ECS J. Solid State Sci. Technol. 2 R3119-R3131 (2013).

22. H.C. Van de Hulst, "Light Scattering by Small Particles" John Wiley, New York (1987).

23. J.K. Han, J.I. Choi, M. E. Hannah, A. Piquette, J.B. Talbot, K.C. Mishra, J. McKittrick, "Phosphor development and integration for near-UV LEDs," ECS. J. Solid. State. Sci. Tech 2, R3138-R3147 (2013).

24. K.Y. Jung, C.H. Lee, Y.C. Kang, "Effect of surface area and crystallite size on luminescent intensity of Y_2O_3:Eu phosphor prepared by spray pyrolysis," Mater. Lett., 59 2451-2456 (2005).

25. I.P. Suzdalev, "Physics and Chemie of Nanoclusters, Nanostructures and Nanomaterials", Comkniga, Moscow. (2005).

26. J. Kim, H. Luo, E. F. Schubert, J. Cho, C. Sone and Y. Park, "Strongly Enhanced Phosphor Efficiency in GaInN White Light-Emitting Diodes Using Remote Phosphor Configuration and Diffuse Reflector Cup," Jpn. J. Appl. Phys., Vol. 44, No. 21 (2005).

27. N. Narendran, Y. Gu, J. P. Freyssinier-Nova, and Y. Zhu, "Extracting phosphor-scattered photons to improve white LED efficiency," *phys. stat. sol.* (a) 202, No. 6 (2005).

Chapter 3. Electrophoretic deposition

3.1. Overview of electrophoretic deposition

The electrophoretic deposition (EPD) technique has gained increasing interest due to the high versatility of its use with different materials and cost-effectiveness with simple set-up. The Russian scientist Ruess observed an electric field induced movement of clay particles in water for the first time in 1808, which can be used for EPD, however the first practical use of EPD happened in 1933 when the USA patent was issued regarding the deposition of thoria particles on a platinum cathode as an emitter for electron tube application [1]. Electrophoretic deposition is a colloidal process and has advantages of short process time and a simple apparatus. Compared to other techniques, the EPD process can be used in a variety of applications since it can be modified easily. For example, deposition can be made on flat, cylindrical or any other shaped substrate with just change in the electrode shape and the position in the bath. Also, EPD offers easy control of the thickness and morphology of a deposited film by simple parameters of the deposition time and applied voltage. During EPD, charged powder particles, dispersed or suspended in a liquid medium are attracted and deposited to a conductive substrate of opposite charge by the aid of the electric field. There are two types of electrophoretic deposition depending on which electrode on which to deposit. When the particles are positively charged, the deposition occurs on the cathode and the process is called cathodic electrophoretic deposition. On the other hand, when the particles are charged negatively and the charged particles are deposited on positive electrode (anode) is called anodic electrophoretic deposition. By suitable modification of the surface charge on the particles, either of these two modes of deposition is possible. Figure 3.1. shows a schematic illustration of the two electrophoretic deposition processes.

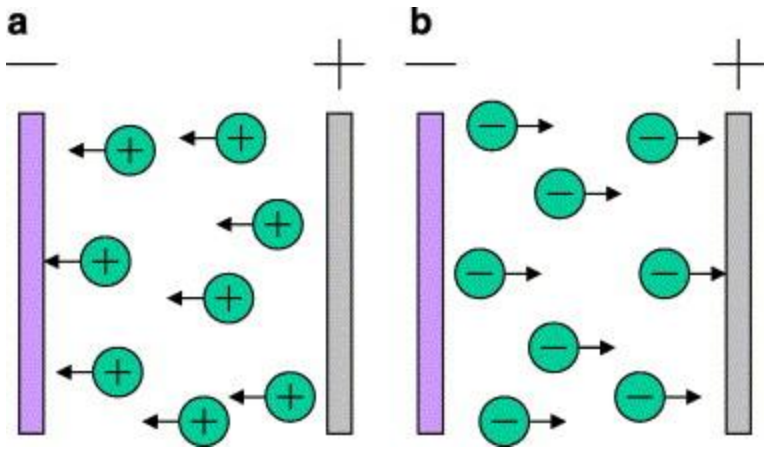

Figure 3.1. Schematic illustration of electrophoretic deposition process. (a) cathodic EPD and (b) anodic EPD [1].

Electrophoretic deposition also has advantages in the deposition of complex compounds and ceramics. The degree of stoichiometry in the electrophoretic deposit is controlled by the degree of stoichiometry of the powder used in the EPD bath. Sarkar and Nicholson [2] observed that particle/electrode reactions are not involved in EPD, and ceramic particles do not lose their charge on being deposited which can be shown from the observation that reversal of the electric field will strip of the deposited layer [3]. Therefore, it is important to use similarly charged particles and similar solvent–binder–dispersant systems for better control of layer thickness. The main driving force for EPD is the charge on the particle and the electrophoretic mobility of the particles in the suspension medium under the influence of an applied electric field. From the literature, the EPD technique has been used successfully for different materials, such as thick film of silica [4], nanosize zeolite membrane [5], hydroxyapatite coating on metal substrate for biomedical applications [6, 7], luminescent materials [8-10], high-Tc superconducting films [11, 12], gas diffusion electrodes and sensors [13, 14], multi-layer composites [15], glass and ceramic matrix composites by infiltration of ceramic particles onto fiber fabrics [16], oxide nanorods [17], carbon nanotube film [18], functionally graded ceramics [19, 20], layered ceramics [21], superconductors [22, 23], piezoelectric materials [24], etc.

3.1. Factors influencing EPD

Many parameters must be considered to gain a high quality of deposition, such as the nature of both the particles and the suspension medium, surface properties of the powder, and the influence of the type and concentration of the additives, mainly dispersants. It has to be noted that the current is carried not only by the charged particles, but by free ions co-existing in the bath. Therefore, the amount of deposited particle is not simply related to the current. However, the current carried by the free ions can be ignored when the amount of free ions is negligible. Actually, the amount of free ions is very small in typical EPD suspensions. Another thing to be

considered is that the accumulation of anionic or cationic charged particle at the electrodes during EPD can reduce the subsequent layer deposition rate. However, the effect of accumulated charged particles is negligible in the initial stage of EPD.

3.2.1. Particle size

Even though there is no general rule to define optimal particle sizes for electrophoretic deposition, decent quality of deposits have been reported in the range of 1-20 μm [25]. Recently, with increasing interest on nanostructured materials, the EPD technique is being popular for the assembly of nanoparticles. It is important that the particles remain completely dispersed and stable for homogeneous and smooth deposition. For larger particles, the main problem is that they tend to settle due to gravity. Ideally, the mobility of particles due to electrophoresis must be higher than that from gravity. Electrophoretic deposition from settling suspension will lead to a gradient in deposition. In addition, for electrophoretic deposition to occur with larger particles, either a very strong surface charge must be obtained, or the electrical double layer region must increase in size. Also the suspension may be stirred or flowed to counter settling. Particle size has also been found to have a significant influence on controlling the cracking of the deposit during drying [26].

3.2.2. Dielectric constant of liquid

Powers [27] studied beta-alumina suspensions in numerous organic media and determined the incidence of deposition as a function of the dielectric constant of the liquid and the conductivity of the suspension. A sharp increase in conductivity with dielectric constant was observed. It has to be noted that impurities affect the conductivity and that conductivity of suspension is very different to that of pure liquid, as a consequence of dissociative or adsorptive charging modes. Powers [27] obtained the optimal dielectric constant range, which was 12–25.

With too low a dielectric constant, deposition fails because of insufficient dissociative power, while with a too high dielectric constant, the high ionic concentration in the liquid reduces the size of the double layer region and the electrophoretic mobility. Therefore, the favorable ionic concentration in the suspension medium is low, in low dielectric constant suspension medium. The dielectric constant is the product of relative dielectric constant and dielectric constant in vacuum. Table 3.1. shows physical properties such as viscosity and relative dielectric constant of some solvents [28].

Table 3.1. Physical properties of non-aqueous solvents [28].

Solvents	Viscosity (cP) $= 10^{-3}$ N s m^{-2}	Relative dielectric constant
Methanol	0.557	32.63
Ethanol	1.0885	24.55
n-Propanol	1.9365	20.33
Iso-propanol	2.0439	19.92
n-Butanol	2.5875	17.51
Ethylene glycol	16.265	37.7
Acetone	0.3087	20.7
Acetylacetone	1.09	25.7

3.2.3. Conductivity of the suspension

The conductivity of the suspension is a key factor and needs to be taken into account during EPD [29]. It has been observed that if the suspension is too conductive, particle motion is very low, and if the suspension is too resistive, the particles charge electronically and the stability is lost. Conductivity of the suspension increased with both temperature and dispersant concentration. Ferrari and Moreno found the existence of a narrow band of conductivity range at varying dispersant dosage and temperature, in which the deposit is formed [29]. Higher and lower values of conductivity impeded the deposition. Aqueous Al_2O_3 suspension conductivity out of the optimal region (140–180 μS/cm) was not suitable for EPD. This suitable region of conductivity is however expected to be different for individual EPD systems.

In our system, the conductivity of various nitrate salts in IPA was measured and analyzed to determine the conductivity at infinite dilution and dissociation constants as shown in Table 3.2. [30]. The mobility of the ions can be determined with the use of the limiting conductivity and concentration of ions can be calculated from the dissociation constant [30]. The dissociation constants are very low and in the concentration range of 10^{-4} to 10^{-3} M $Mg(NO_3)_2$ typically used in EPD baths, and $MgNO_3^+$ was the predominant cation available to charge the phosphor and to form the binder.

Table 3.2. Limiting conductivities (**Λ**o) and dissociation constants (K_D) of nitrate salts in IPA [30].

Reaction	Λ_o(cm^2/mole-ohm)	K_D (M)
$NaNO_3 \rightarrow Na^+ + NO_3^-$	17	3×10^{-4}
$Mg(NO_3)_2 \rightarrow Mg(NO_3)^+ + NO_3^-$	18	6×10^{-5}
$Mg(NO_3)^+ \rightarrow Mg^{2+} + NO_3^-$	120	2×10^{-7}

3.2.4. Viscosity of suspension

Especially in the case of casting processes, the main parameter to control EPD is the viscosity. In general EPD process, the solid loading is very low and the viscosity cannot be used to evaluate the dispersion state exactly [29]. However, the desired property of the suspension medium is a low viscosity, as shown in Table 3.1. Low solids loadings are typically chosen also so that the viscosity of the suspension remains low.

3.2.5. Zeta potential

The zeta potential quantifies the electrostatic interactions, and is the most used parameter to determine particle stability. In fact, the zeta potential represents the potential developed in the shear plane of the double layer system [31] as shown in Figure 3.2. Thus, the zeta potential is a guideline of the magnitude of the electrostatic repulsive forces that keep particles distributed and suspended within the solvent. The zeta potential of particles is a key factor in the electrophoretic deposition process. It is necessary to achieve a high and uniform surface charge of the suspended particles. It plays a role in: (i) stabilization of the suspension by determining the intensity of repulsive interaction between particles, (ii) determining the direction and migration velocity of particle during EPD, and (iii) determining the green density of the deposit. The overall stability of a system depends on the interaction between individual particles in the suspension. Two mechanisms affect this interaction, which are due to electrostatic and van der Waals forces. A high electrostatic repulsion from high particle charge is required to avoid particle agglomeration. The particle charge also affects the green density of the deposit. During formation of the deposit, the particles become closer to each other and with increasing attraction force. If the particle charge is low, the particles would coagulate even for relative large inter-particle distances, leading to porous and poor quality of deposits. On the other hand, if the particles have a high surface charge during deposition, they will repulse each other, occupying positions which will

lead to high particle packing density [32]. Therefore, it is important to control the solids loading and concentration of solvents and additives in the EPD suspension in order to reach the highest possible green density of the deposit. The zeta potential can be controlled by a variety of charging agents, such as acids, bases and specifically adsorbed ions or polyelectrolytes, to the suspension [33].

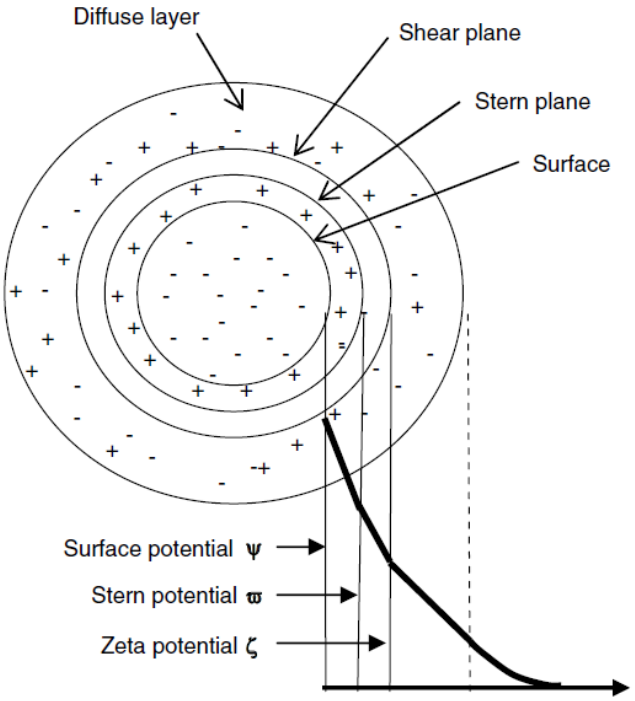

Figure 3.2. The different planes and potentials at the double layer [31].

3.2.6. Stability of suspension

Electrophoretic deposits are formed from the motion of particles in a suspension by the aid of an electric field, and the deposition occurs when the distance over which the double layer charge falls to zero is large compared to the particle size. In this condition, the particles will move relative to the liquid phase when the electric field is applied. Also, the suspension stability is

determined by the settling velocity of the particles and tendency to undergo or avoid flocculation. Therefore, stable suspension means no tendency to flocculate, settle slowly and form dense deposits at the electrode of the bath [1]. If the particles flocculate, suspensions settle quickly and form low density, weakly adhered deposits. However, if the suspension is too stable, the repulsive forces between the particles will not be overcome by the electric field, and then deposition will not occur. Therefore, it is desirable to find suitable physical/chemical parameters that enable the sufficient deposition from a suspension. Most useful parameters to determine the stability of EPD bath are zeta potential or electrophoretic mobility, but these do not guarantee the ability of a suspension to deposit. That is the particles may move to the substrate by electrophoretic force, but may not adhere to the substrate.

3.2.7. Deposition time

The deposition rate is constant during the initial time of deposition. But for longer times, the deposition rate decreases and reaches zero at long time when using a constant voltage during EPD. Figure 3.3. shows a deposition of ZnO on a copper electrode at different applied potentials with increasing time [34]. While the potential difference between the electrodes is maintained constant, the electric field influencing deposition decreases with deposition time because of the formation of an insulating layer of particles on the electrode surface as shown in Figure 3.4. [35]. But, during the initial period of EPD, there is generally a linear relationship between deposition mass and time.

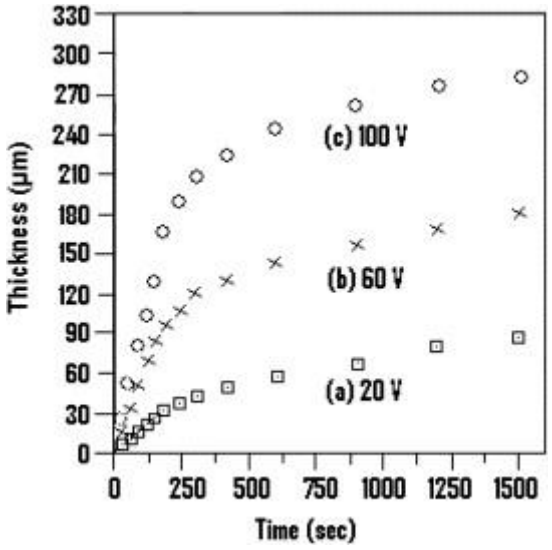

Figure 3.3. Relationship between deposit thickness and time of deposition for ZnO coatings on copper electrode at different applied potential [34].

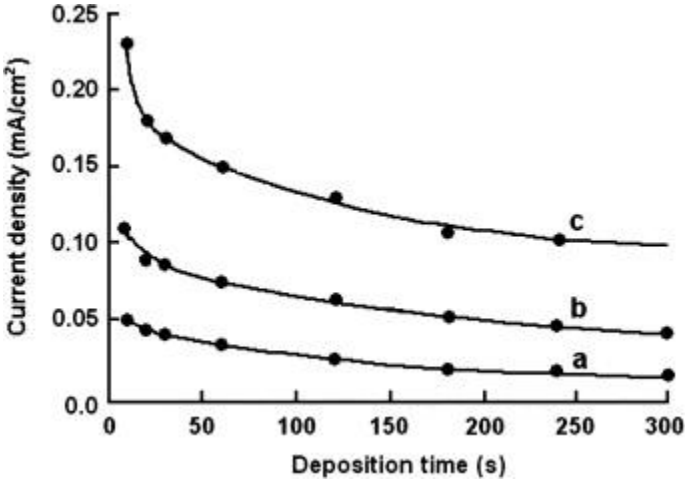

Figure 3.4. Current density versus deposition time for deposition of hydroxyapatite at different applied voltages: (a) 50 V; (b) 100 V; (c) 200 V [35].

3.2.8. Applied voltage

Generally, the amount of deposit increases in proportion to the applied potential. Basu et al. [36] found that more uniform films are deposited at moderate applied fields (25–100 V/cm), while the film quality gets poor if relatively higher applied fields (>100 V/cm) are used. Because the formation of a film on the electrode is a kinetic phenomenon, the accumulation rate of the particles influences their packing quality during EPD [36]. For a higher applied field, which may cause turbulence in the suspension, the deposition may be disturbed by flows in the surrounding medium. In addition, if the particles move too fast, the particles cannot find enough time to sit in their positions to form a close-packed layer. Finally, in a high field condition, lateral motion of the particles once deposited, are restricted on the surface of the already deposited layer, because higher applied potential exerts more pressure on particle flux and movement. Therefore, the applied field affects the deposition rate and the structure of the deposit.

3.2.9. Concentration of solids in the bath

The volume fraction of solids in the suspension plays an important role, particularly for multi-component EPD. Even if each of the particle materials has the same zeta potential, they could deposit at different rates depending on their volume fraction of solids in the suspension [1]. If the volume fraction of solids is high enough, the powders deposit at an equal rate. However, if the volume fraction of solids is low, the particles can deposit at rates proportional to their individual electrophoretic mobility [37]. Once other parameters are fixed, the most dominant parameters influencing the electrophoretic deposition are the applied voltage, deposition time and particle concentration in the suspension. Table 3.3. summarizes the range of parameters influencing successful EPD. Note that the values are a typical range of a specific system and cannot be applied to the whole system. Parameters need to be optimized corresponding to the individual EPD bath conditions.

Table 3.3. Parameters influencing EPD.

EPD parameter	Range
Dielectric constant of liquid	12–25
Viscosity of suspension	0.5–3 mPa·s
Zeta potential	± 30–70 mV
Deposition time	5 s –1 h
Applied voltage	25–100 V/cm
Concentration of solid	< 20 vol.%

3.3. EPD applied to solid state lighting

EPD has been used to deposit phosphors for information displays and more recently for LEDs, both in the conformal and remote configurations. EPD has been used for the preparation of specialized CRTs since the 1950s [38-40]. More recently, EPD has been used to prepare flat panel emissive displays [41].

EPD has the ability to coat a uniform, highly packed, conformal phosphor layer on the LED to control color and efficiency. The commercial technique typically employed for phosphor deposition on LEDs involves simply painting or dispersing phosphor powders blended in a liquid polymer onto the LED die, which is then dried or cured. However, a conformal coating improves the spatial color distribution of LEDs [42].

Several methods for coating YAG:Ce (2.7 μm) particles, such as the slurry method, the settling method, standard EPD, and a modified EPD were compared for preparing the phosphor layer on the InGaN chip [43]. For the modified EPD method, post-annealing was not done, but the deposit was sprayed with a PVA photoresist and UV cured to enhance adhesion [44]. The intensity and color of white light was dependent on the thickness of the phosphor layer. It was found that the properties of the phosphor layer, such as packing density, thickness and uniformity, could be more easily controlled by EPD than by the slurry and settling methods. Furthermore, the high packing density from EPD allowed a thinner layer to be fabricated.

In other work, YAG:Ce powder (~ 5–10 μm) was coated onto two surface mounted device (SMD) LEDs [45]: one directly and one filled with a thin epoxy layer around the LED chip in which the thickness was less than that of LED die. These LEDs were compared to the conventional method of dispersing the phosphor in the epoxy. With the thin epoxy layer, the light color was more uniform, and the white color value was well controlled; however, the luminous efficiency was lower than that without the thin epoxy layer. It was found that both EPD LEDs had a lower efficiency than the dispersed phosphor LED. It was suggested that this was due to larger

difference in refractive index between the phosphor and GaN compared to the difference between epoxy and GaN, such that blue light extraction efficiency was decreased. A patent [46] describes an EPD method for coating phosphor on a chip. An anode is place in the bath with the LED, with a voltage applied between the anode and the p-side of the LED to be positive with respect to the p-side and a second voltage applied between the p-side and the n-side to cause the suspended particles to deposit onto the LED. This allowed control over material deposition on the semiconductor device improving manufacturing efficiency by reducing material waste and providing coating only where required. This method is suitable for color-critical application compared to current phosphor deposition systems.

EPD of Ca-α-SiAlON:Eu^{2+} onto an ITO-coated glass was investigated [47]. The light emission from the deposit surfaces was characterized by comparing the intensities of the excited yellow light and the transmitted blue light, both which decreased with an increase of the film thickness. Therefore, deposit thickness greatly affected the color tone that was controllable from blue-white to yellow-white. Also, EPD of laminated and mixed SiAlON phosphor was used to tune emission colors as shown in Fig 3.5. (a) and (b) [48]. The laminated films were prepared by sequential EPD using the three types of suspensions. To tune emission colors, the thickness and the build-up order of the sequentially deposited layers of yellow, green and red phosphor was altered. The mixed films were prepared by single deposition using the suspensions that contain two or three types of phosphors. The white light emitting devices prepared by this method showed broad spectra, comparable to those of fluorescent lamps.

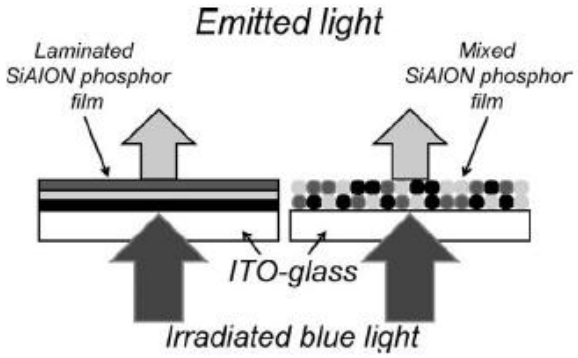

(a)

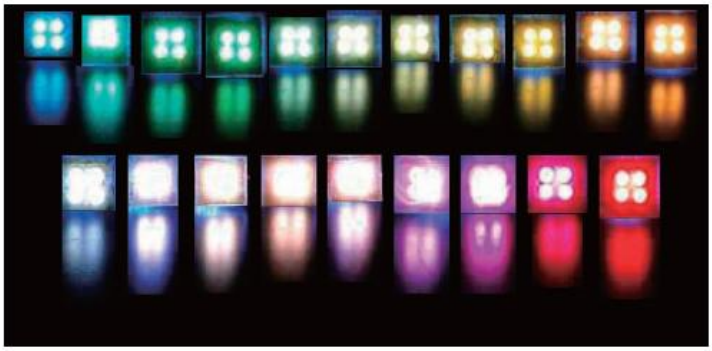

(b)

Figure 3.5. (a) Schematic illustration of flat light-emission panels with laminated or mixed SiAlON phosphor. (b) Examples of the multicolor light emitting panels prepared by laminating the three types of phosphors. [48].

3.4. Modeling of electrophoretic deposition

EPD is based on the migration and deposition of charged particles in a stable suspension by the application of an electric field between electrodes. Deposit yields depend on many factors, such as stability, solid content of the suspension, aggregation and arrangement of the particles on the electrode surface. Also, suspension properties, such as conductivity, zeta potential, viscosity are important parameters of the EPD process. The deposit mass can be estimated when the EPD bath is stable, indicating that the particles have to be dispersed well throughout the suspension medium, so the particles can move to the electrode independently without agglomerates [49, 50].

The first model of EPD kinetics was proposed by Hamaker in 1940 for electrophoretic cells with a planar geometry [51], as follows:

$$m = C_s \mu S E t \tag{1}$$

where m (g) is the deposited mass, C_s (g cm^{-3}) is the suspension concentration, μ (cm^{2}s^{-1}V^{-1}) is the electrophoretic mobility, E (V cm^{-1}) is the electric field, S (cm^2) is the deposition area, and t (s) is the deposition time,. The Hamaker equation is valid only for short times when C_s and the electric field are assumed to be constant. However, during EPD, the amount of particles removed from the suspension increases with time, thereby decreasing the concentration in the bath. To account for this, Sakar and Nicholson [52] expressed the deposited mass as:

$$m(t) = m_0\left(1 - e^{-t/\tau}\right) \tag{2}$$

where m_0 is the initial mass of powder and τ is the characteristic time scale given by:

$$\tau = \frac{V}{\mu A_s E} \tag{3}$$

where V is the volume of suspension, μ is the electrophoretic mobility, A_s is the deposition area, and E is the electric field. This equation indicates that the deposition rate is expected to decrease exponentially as a function of time due to depletion of the bath by particle deposition.

Biesheuvel et al. [53] have described a model for the growth of the deposit, based on the theory of sedimentation for planar and cylindrical geometries. This theory describes the bulk effect of the particle motion on the transport phenomena near the deposition electrode, based on the expression of the mass balance of the suspension-deposit boundary evolution, resulting in:

$$\frac{d\delta}{dt} = -v\frac{\phi_s}{\phi_d - \phi_s} \tag{4}$$

where v (cm s^{-1}) is the electrophoretic rate of particles close to the electrode, ϕ_d is the volumetric fraction of the deposit and, ϕ_s is the volumetric fraction of the suspension. The deposit thickness δ (cm) is defined as follows:

$$\delta = \frac{V_d}{S} = \frac{m/C_d}{S} \tag{5}$$

where V_d (cm^3) is the deposit volume and C_d (g cm^{-3}) is the deposit concentration. This growth theory is limited to explain the evolution of the deposit-suspension boundary, and the system was regarded as a non-stirred and electrically neutral suspension. As a consequence, some phenomena occurring during the EPD process are neglected, including the decrease of particle concentration, the movement of particles by diffusion, and the local changes of the charge on the electrodes, both on the particle surface and its surrounding ionic clouds.

To avoid the effect of the increase of the deposit resistivity in the effective electrical force acting on particles, Sarkar and Nicholson suggested working under galvanostatic or constant-current conditions [52]. In that way, the voltage drop across two electrodes increases with time, but the voltage/unit length in the suspension remains constant. Similarly, Ma and Cheng [54] determined experimentally the relationship between the kinetics parameter, k, and the applied current intensity under galvanostatic conditions:

$$k = k_0(e^{i/i_0} - 1) \tag{6}$$

where i (mA cm^{-2}) is the current density, and i_0 (mA cm^{-2}) and k_0 (s^{-1}) are considered as the reference conditions from which the expression predicts the kinetics constant from different

values of the applied current, facilitating more effective modeling and control of the process. However, most of EPD are performed under constant-voltage conditions, and hence substantial efforts have been made to model the effective electric field applied for each system [55-57].

G. Anné et al. [58] proposed a mathematical description of the kinetics based on the Hamaker model and the Biesheuvel correction for suspensions with a high solid loading considering that the suspension conductivity and the current density vary during EPD under constant voltage conditions. The expression of the electric field as a function of the conductivity of the suspension is

$$E = \frac{I}{S\sigma_s} \tag{7}$$

where the suspension conductivity is σ_s (S cm^{-1}). This model agreed with EPD results obtained from an alumina suspension prepared with ethanol and different additives as dispersants.

Ferrari et al. [59] proposed a resistivity model for the deposition kinetics considering the relationship between colloidal parameters such as suspension concentration and resistivity during the EPD process. This model describes experimental results obtained for longer deposition times and for suspensions in which resistivity changes significantly during the deposition process.

Recently, alternatives to the standard electrophoretic process have been proposed to obtain free-standing laminate nanostructures [60] or design prototyping [61] and nanopatterning films [62], or avoid bubble formation at the electrodes during aqueous EPD, by applying AC electric fields [63, 64] or a constant current pulse [65]. The kinetics of these processes could be also approximated by the equations discussed. Table 3.4. summarizes the relevant equations, corrections and experimental expressions proposed by different authors [31], highlighting the parameter on which each one is focused. Other parameters listed in this table are defined as follows: f is the efficiency factor or "sticking parameter", $f \leq 1$ (i.e. if all the particles reaching the electrode take part in the formation of the deposit $f = 1$). R′ is a constant and given by:

$$R' = \frac{\left(\frac{\rho_s}{\rho_d} - 1\right)}{C_d S} \tag{8}$$

where ρ_s and ρ_d (Ω cm) are the resistivities of the suspension and the deposit respectively. *L* (cm) is the distance between electrodes and *I* (A) is the current.

Table 3.4. Summary of different equations, corrections and experimental expressions of the EPD kinetics [31].

Kinetics equation	Characteristic time
Basic equation [55]	
$m = C_s \mu S E t$	0
Quantification of the deposition behavior: the sticking factor [57]	
$m = f \mu S E C_s t$	0
Considering the decrease of solid loading with time [57]	
$m(t) = m_0(1 - e^{-t/\tau})$	$\tau = \frac{V}{f \mu S E}$
Considering concentrated suspensions ($\phi_s > 0.2$) [67]	
$m = C_s \mu S E t \frac{\phi_d}{\phi_d - \phi_s}$	0
Considering solid loading and electric field variation with time [57]	
$R'm(t) + (R'm_0 + L)\ln(\frac{m_0 - m(t)}{m_0}) + k'\Delta\psi t = 0$	$k' = \frac{1}{\tau'} = \frac{f \mu S}{V}$
Variation of the kinetics parameter vs. applied current [69]	
$k = k_0(e^{i/i_0} - 1)$	$k = \frac{1}{\tau} = \frac{f \mu S E}{V}$
Considering suspension resistivity variation with time [108]	
$m(t) = m_0(1 - e^{-t/\tau})$	$\tau = \frac{V}{f \mu I} \rho_S(t)$
Considering the linear relationship of the suspension resistivity and solid loading, and their variation with time [109]	
$m(t) = m_0(1 - \frac{1}{1 + \frac{\rho_{s,0}}{\rho_{s,\infty}}(e^{t/\tau_\infty} - 1)})$	$\tau_\infty = \frac{V}{f \mu I} \rho_{S,\infty}$

References

1. L. Besra, M. Liu, "A review on fundamentals and applications of electrophoretic deposition (EPD)," Progress in Materials Science, 52, 1-61 (2007).

2. P. Sarkar, P.S. Nicholson. "Electrophoretic deposition (EPD): mechanisms, kinetics and application to ceramics," J Am Ceram Soc, 79(8):1987–2002 (1996).

3. S.A. Troelstra."Applying coatings by electrophoresis," Philips Tech Rev,12:293–303 (1951).

4. K. Hasegawa, S. Kunugi, M. Tatsumisago, T. Minami. "Preparation of thick films by electrophoretic deposition using modified silica particles derived by sol–gel method," J Sol–gel Sci Technol;15:243–9 (1999).

5. W. Shan, Y. Zhang, W. Yang, C. Ke, Z. Gao, Y. Ke, "Electrophoretic deposition of nano-size zeolites in non-aqueous medium and its application in fabricating thin zeolite membranes," Micropor Mesopor Mater;69:35–42 (2004).

6. M. Wei, A.J. Ruys, B.K. Milthorpe, C.C. Sorrell, J.H. Evans. "Electrophoretic deposition of hydroxyapatite coatings on metal substrate: a nano-particulate dual coating approach," J Sol–gel Sci Technol;21:39–48 (2001).

7. T.M. Sridhar, U.K. Mudali. "Development of bioactive hydroxyapatite coatings on Type 316L stainless steel by electrophoretic deposition for orthopaedic applications," Trans Ind Inst Met;56(3):221–30 (2003).

8. J.H. Yum, S.Y. Seo, S. Lee, Y.E. Sung. "$Y_3Al_5O_{12}$: $Ce_{0.05}$ phosphor coating on gallium nitride for white light emitting diodes," J Electrochem Soc;150(2):H47–52 (2003).

9. M.J. Shane, J.B. Talbot, B.G. Kinney, E. Sluzky, H.R. Hesse. "Electrophoretic deposition of phosphors: II deposition experiments and analysis," J Colloid Interface Sci;165:334–40 (1994).

10. M.J. Shane, J.B. Talbot, R.G. Schreiber, C.L. Ross, E. Sluzky, K.R. Hesse. "Electrophoretic deposition of phosphors: I conductivity and zeta potential measurements," J Colloid Interface Sci;165:325–33(1994).

11. M.T. Ochsenkuehn-Petropoulou, A.F. Altzoumailis, R. Argyropoulou, K.M. Ochsenkuehn. "Superconducting coatings of MgB_2 prepared by electrophoretic deposition," Anal Bioanal Chem;379:792–5 (2004).

12. P. Sarka, S. Mathur, P.S. Nicholson, C.V. Stager. "Fabrication of textured Bi–Sr–Ca–Cu–O thick film by electrophoretic deposition," J Appl Phys;69(3):1775–7 (1991).

13. K. Hayashi, N. Furuya. “Preparation of gas diffusion electrodes by electrophoretic deposition,” J Electrochem Soc;151(3):A354–7 (2004).

14. N. Dougami, T. Takada. “Modification of metal oxide semiconductor gas sensor by electrophoretic deposition,” Sens Actuators B;93:316–20 (2003).

15. K. Yamashita, E. Yonehara, X. Ding, M. Nagai, T. Umegaki, M. Matsuda. “Electrophoretic coating of multilayered apatite composite on alumina ceramics. HA coating on alumina ceramics,” John Wiley and sons, Inc.;. p. 46–53 (1998)

16. A.R. Boccaccini, H. Kern, H.G. Krueger, P.A. Trusty, D.M.R. Taplin. “Electrophoretic deposition of nanoceramic particles onto electrically conducting fibre fabrics,” In: Proceedings of the 43rd international scientific colloquium. Technical University of Ilmenau, September 21–24; p. 630–5 (1998).

17. S.J. Limmer, G. Cao. “Sol–gel electrophoretic deposition for the growth of oxide nanorods,” Adv Mater;15(5):427–31(2003).

18. C. Du, D. Heldbrant, N. Pan. “Preparation and preliminary property study of carbon nanotubes films by electrophoretic deposition,” Mater Lett;57:434–8 (2002).

19. S. Put, J. Vleugels, G. Anne, O. Van der Biest. “Functionally graded ceramic and ceramic-metal composites shaped by electrophoretic deposition,” Colloids Surf A: Physicochem Eng Aspects;222:223–32 (2003).

20. P. Sarkar, S. Datta, P.S. Nicholson. “Functionally graded ceramic/ceramic and metal/ceramic composites by electrophoretic deposition,” Composites Part B;28B:49–54 (1997).

21. B. Ferrari, A.J. Sanchez-Herencia, R. Moreno. “Electrophoretic forming of Al_2O_3/Y-TZP layered ceramics form aqueous suspension,” Mater Res Bull;33(3):487–99 (1998).

22. H.S. Maiti, S. Datta, R.N. Basu . “High Tc superconductor coating on metal substrates by an electrophoretic technique,” J Am Ceram Soc;72(9):1733–5 (1989).

23. S.K.F. Yau, C.C. Sorrel. “High-Jc $(Bi,Pb)_2Sr_2Ca_2CuO10^+x$ tapes fabricated by electrophoretic deposition,” Physica C;282–287:2563–4 (1997).

24. J. Van Tassel, C.A. Randall. “Electrophoretic deposition and sintering of thin/thick PZT film,” J Eur Ceram Soc;19:955–8 (1999).

25. N. Heavens. “Electrophoretic deposition as a processing route for ceramics,” In: Binner GP, editor. Advanced ceramic processing and technology, vol. 1. Park Ridge (NJ), USA: Noyes Publications; p. 255–83 [chapter 7] (1990).

26. N. Sato, M. Kawachi, K. Noto, N. Yoshimoto, M. Yoshizawa. “Effect of particle size reduction on crack formation in electrophoretically deposited YBCO films,” Physica C;357–360:1019–22 (2001).

27. R.W. Powers. “The electrophoretic forming of beta-alumina ceramic,” J Electrochem Soc;122:482–6 (1975).

28. H. Negishi, H. Yanagishita, H. Yokokawa. “Electrophoretic deposition of solid oxide fuel cell material powders,” In: Proceedings of the electrochemical society on electrophoretic deposition: fundamentals and applications, vol. 2002-21, Pennington, USA,. p. 214–21 (2002).

29. B. Ferrari, R. Moreno. “The conductivity of aqueous Al2O3 slips for electrophoretic deposition,” Mater Lett;28:353–5 (1996).

30. J. B. Talbot, E. Sluzky and S. K. Kurinec, “Electrophoretic deposition of monochrome and color phosphor screens for information displays,” J. Materials Science, 39, 771-778 (2004).

31. R. Moreno and B. Ferrari, “Nanoparticles dispersion and the effect of related parameters in the EPD kinetics,” chapter 2, Springer Book 978-1-4419-9730-2 (Online) “Electrophoretic deposition of nanomaterials,” editor: J. H. Dickerson and A.R. Boccaccini (2012).

32. H.G. Krueger, A. Knote, U. Schindler, H. Kern, A. Boccaccini. “Composite ceramic metal coatings by means of combined electrophoretic deposition,” J Mater Sci;39:839–44 (2004).

33. M. Zarbov, I. Schuster, L. Gal-Or. “Methodology for selection of charging agents for electrophoretic deposition of ceramic particles. In: Proceedings of the international symposium on electrophoretic deposition: fundamentals and applications,” The Electrochemical Society Inc, USA, Proc. vol. 2002-21, p. 39–46 (2002).

34. Y.C. Wang, I.C. Leu, M.H. Hon. “Kinetics of electrophoretic deposition for nanocrystalline zinc oxide coatings,” J Am Ceram Soc;87(1):84–8 (2004).

35. I. Zhitomirsky, L. Gal-or. “Electrophoretic deposition of hydroxyapatite,” J Mater Sci: Mater Med;8:213–9 (1997).

36. R,N. Basu, C.A. Randall, M.J. Mayo. “Fabrication of dense zirconia electrolyte films for tubular solid oxide fuel cells by electrophoretic deposition,” J Am Ceram Soc;84(1):33–40. (2001).

37. L. Vandeperre, O. Van Der Biest, W.J. Clegg. "Silicon carbide laminates with carbon interlayers by electrophoretic deposition," Key Eng Mater (Pt. 1, Ceramic and Metal Matrix Composites);127–131: 567–73 (1997).

38. N.F. Cerulli, US Patent 2851408 (1958).

39. J.D. McGee, R.W. Airey, M. Aslam "The evaluation of cascade phosphor-photocathode screens," Adv. Electr. Elect. Phys. **22A**:57 (1966).

40. P.C. Libman. US Patent 4891110 (1990).

41. J.B. Talbot, E. Sluzky, and S. K. Kurinec, *Journal of Materials Science*, 39, 771-778 (2004).

42. J.B. Talbot, "Electrophoretic Depostion of Phosphors for Information Displays and Solid State Lighting", Nanostructure Science and Technology, Part 2, p 269 (2012).

43. J.H. Yum, S.Y. Seo, S. Lee, Y.E. Sung, "$Y_3Al_5O_{12}$:$Ce^{0.05}$ phosphor coatings on gallium nitride for white light emitting diodes," J. Electrochem. Soc. **150**(2), H47 (2003).

44. J.H. Yum, K.H. Choi, Y.E. Sung, "Adhesion improvement of phosphor layer by combining electrophoretic deposition and UV curing," J. Electrochem. Soc. **150**(2), H43 (2003).

45. W.R. Chen, J.A. Bai, T.H. Meen, C.J. Huang, "Electrophoretic deposition of YAG phosphor on SMD LED," ECS Trans. 19(12), 27 (2009).

46. C.J. Summers, H. Menkara, J.B.Y. Chua. US Patent 6864110 (2005).

47. T. Kitabatake, T. Uchikoshi, F. Munakata, Y. Sakka, N. Hirosaki, "Electrophoretic deposition of Eu^{2+} doped Ca-α-SiAlON phosphor particles for packaging of flat pseudo-white light emitting devices," J. Ceramic. Soc. Jpn. **116**(6), 740 (2008).

48. T. Kitabatake, T. Uchikoshi, F. Munakata, Y. Sakka, N. Hirosaki, "Emission of color tuning of laminated and mixed SiAlON phosphor films by electrophoretic deposition," J. Ceramic. Soc. Jpn. **118**(1), 1-4 (2010).

49. C. Ji, W. Lan, P. Xiao, "Fabrication of yttria-stabilized zirconia coatings using electrophoretic deposition: packing mechanism during deposition," J. Am. Ceram. Soc. **91**, 1102–1109 (2008).

50. B. Ferrari, R. Moreno, R, "EPD kinetics: a review," J. Eur. Ceram. Soc. **30**, 1069–1078 (2010).

51. H.C. Hamaker, “Formation of a deposit by electrophoresis,” Trans. Faraday Soc. **36**, 279–287 (1940).

52. P. Sarkar, P.S. Nicholson, “Electrophoretic deposition (EPD): mechanisms, kinetics, and application to ceramics,” J. Am. Ceram. Soc. **79**, 1897–2002 (1996).

53. P.M. Biesheuvel, H. Verweij, “Theory of cast formation in electrophoretic deposition,” J. Am. Ceram. Soc. **82**, 1451–1455 (1999).

54. J. Ma,, W. Cheng, “Electrophoretic deposition of lead zirconate titanate ceramics,” J. Am. Ceram. Soc. **85**, 1735–1737 (2002).

55. L. Stappers, L. Zhang, O. Van Der Biest, J. Fransaer, “The effect of electrolyte conductivity on electrophoretic deposition,” J. Colloid Interface Sci. **328(**2), 436–446 (2008).

56. C. Pignolet, C. Filiarte, A. Foissy, “Influence of surfactant counter-ions during electrophoretic particle deposition,” Langmuir **24**, 10181–10186 (2008).

57. S.J. Ciou, K.Z. Funga, K.W. Chiang, “Behaviors and mechanism of electrolyte electrophoresis during electrophoretic deposition,” J. Power Sources **175**, 33–39 (2008).

58. G. Anné,, K. Vanmeensel, J. Vleugels,, O. Van Der Biest, “A mathematical description of the kinetics of the electrophoretic deposition process for Al_2O_3-based suspensions,” J. Am. Ceram. Soc. **88**, 2036–2039 (2005).

59. B. Ferrari, R. Moreno, J.A. Cuesta, “A resistivity model of electrophoretic deposition,” Key. Eng. Mater. **314**, 175–180 (2006).

60. S.A. Hasan, D.W. Kavich, J.H. Dickerson, “Sacrificial layer electrophoretic deposition of free-standing multilayered nanoparticle films,” Chem. Commun. **25**, 3123–3725 (2009).

61. A. Nold, J. Zeiner, T. Assion, R. Clasen, “Electrophoretic deposition as rapid prototyping method,” J. Eur. Ceram. Soc. **30**, 1163–1170 (2010).

62. Y. Chang, S. Huang, Y. Chen, “Biomolecular nanopatterning by electrophoretic printing lithography,” Small **1**, 63–66 (2009).

63. A.R. Gardeshzadeh, B. Raissi, E. Marzbanrad, H. Mohebbi, “Fabrication of resistive CO gas sensor based on SnO_2 nanopowders via low frequency AC electrophoretic deposition,” J. Mater. Sci: Mater. Electron. **20**, 127–131 (2009).

64. B. Neirinck, J. Fransaer, O. Van Der Biest, J. Vleugels, “Aqueous electrophoretic deposition in asymmetric AC electric fields (AC–EPD),” Electrochem. Commun. **11**, 57–60 (2009).

65. L. Besra,, T. Uchikoshi, T.S. Suzuki, Y. Sakka, “Application of constant current pulse to suppress bubble incorporation and control deposit morphology during aqueous electrophoretic deposition (EPD),” J. Eur. Ceram. Soc. **29**, 1837–1845 (2009).

Chapter 4. Experimental procedure for phosphor synthesis and EPD

4.1. Synthetic methods to prepare phosphor powders

There are many different methods to synthesize inorganic phosphors. The most popular method is solid state synthesis, but the sol-gel/Pechini, co-precipitation, hydrothermal, spray pyrolysis and combustion synthesis methods are often used. Less popular but still used methods include oxidation of metal particles, laser-driven reactions, high energy mechanical milling, self assembly and the deposition of combinational libraries, which are not covered in this paper. Most phosphor compositions have greater than four elements, which make fabrication of uniform, single phase powders difficult. The selection of a synthesis method depends on the requirements of the end use. Table 4.1. provides a list of popular synthetic methods. If low cost and large volume production is desired, solid state reactions are favored. However, due to the use of multiple precursors, several sintering and grinding steps may be required for a full reaction. If small, dispersed, uniformly shaped with a narrow particle size distribution is the goal, then liquid or gaseous methods should be employed. The drawbacks to these methods are high cost, complicated chemical procedures, and small production volume. If evaluation of a large number of compositions is the goal, then combinatorial synthesis or combustion reactions are preferred [1, 2]. Figure 4.1. (a)-(d) shows the procedures of solution-based methods: sol-gel, co-precipitation, hydrothermal, and combustion methods, respectively. Outlined below are descriptions of the common synthesis methods.

Table 4.1. Summary of synthesis methods in terms of the particle sizes, morphology control, chemical homogeneity, cost, time, suitable phosphors and limitations.

Synthesis method	**Solid state reaction (SS)**	**Sol gel/Pechini (SG/P)**	**Co-precipitation (CP)**	**Hydrothermal (HT)**	**Combustion (CS)**	**Spray pyrolysis (SP)**
Particle size	>5 μm	10 nm - 2 μm	10 nm-1μm	10 nm-1μm	500 nm-2μm	100 nm-2μm
Particle size distribution	Narrow – Broad	Narrow	Narrow	Narrow	Medium	Very narrow
Morphological control	Poor - Good	Medium	Very good	Good	Poor	Very good
Purity	Poor – Very Good	Good	Medium	Medium-good	Medium-good	Medium good
Cost	Low	Medium	Medium	Medium-high	Low-medium	Medium
Synthesis time	Short - Long	Medium	Medium	Very long	Short	Short
Suitable phosphors	All compounds	All compounds except nitrides	Oxides and fluorides	All compounds	All compounds except nitrides	All compounds except nitrides
Limitations	- Extensive grinding and milling required	- Requires a soluble precursor - Carbon contamination - Difficult to obtain nitrides, sulfides, other non-oxide materials	- Requires a soluble precursor - Difficult to obtain nitrides	- Requires a soluble precursor - Special equipment needed	- Requires a soluble precursor - Carbon contamination - Difficult to obtain nitrides	- Requires a soluble precursor - Difficult to obtain nitrides and other non-oxide materials

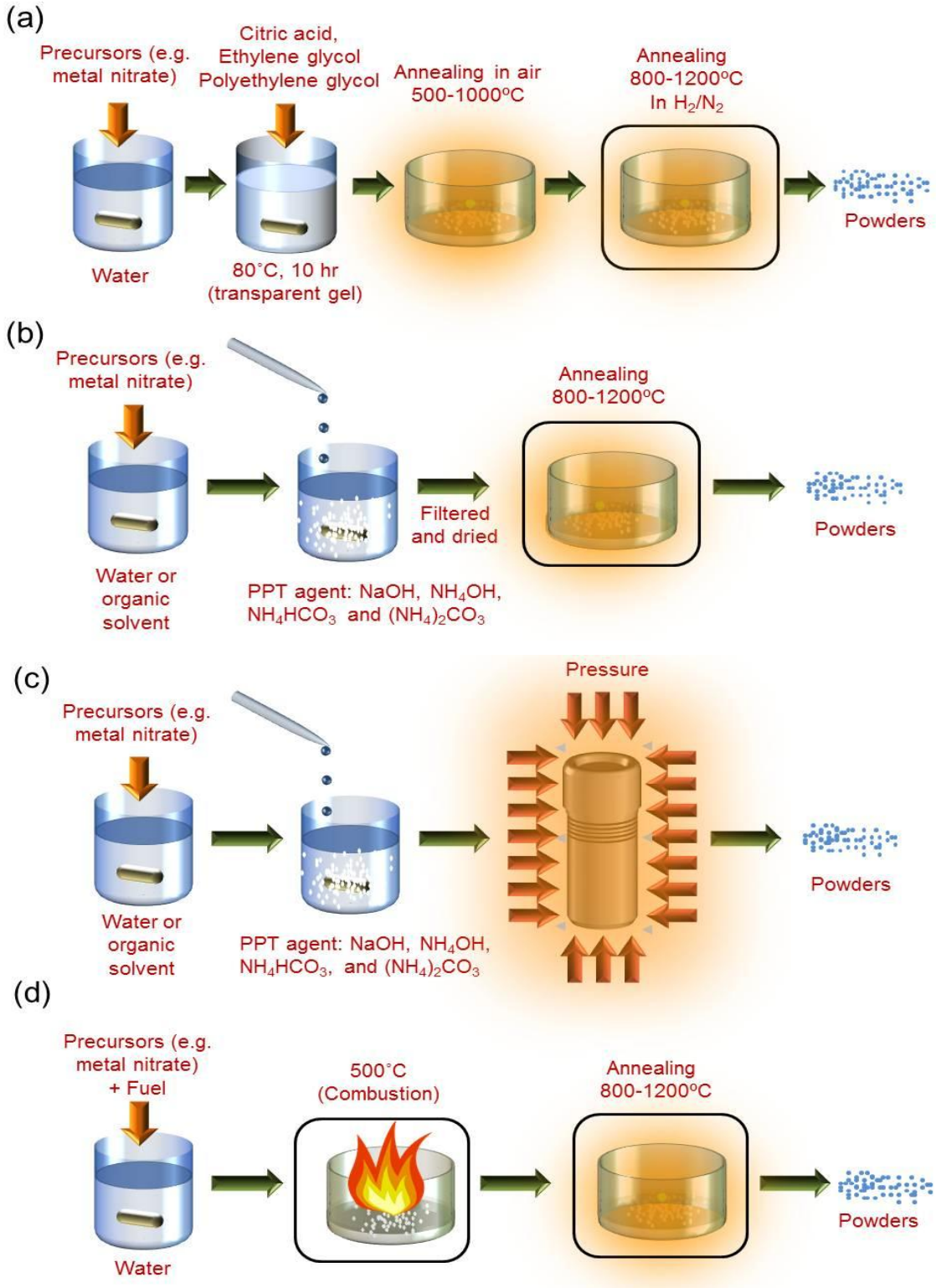

Figure 4.1. Schematic diagram of solution based synthesis (a) sol-gel, (b) co-precipitation, (c) hydrothermal, and (d) combustion synthesis. PPT agent = precipitating agent.

4.1.1. Solid state reaction (SS)

The solid state synthesis method is the most extensively used technique to prepare phosphors [2, 3]. Oxides, (oxy)fluorides, (oxy)chlorides and (oxy)nitrides are prepared by this method, which is straightforward and suitable for mass production. The precursors are usually single cation ceramic powders, which are mixed together and heated to high temperatures to promote interdiffusion and the eventual development of a single phase. This method is known to introduce impurity phases (such as unreacted intermediates between the end members in the phase diagram), which can reduce the luminous efficacy. To eliminate these intermediate phases, repeated grinding, milling and high temperature treatments are required [4]. Due to the high temperatures used during production, nonstoichiometric amounts of precursor materials maybe required to compensate for losses arising from differences in volatility. This is especially true for the manufacture of (oxy)fluorides, (oxy)chlorides, compounds containing barium or lithium and certain nitride phosphors. Furthermore, the average particle size of the phosphors prepared by this method is often larger than 5 μm, making light scattering an issue for integration with a near UV (nUV) chip.

4.1.2. Sol-gel/Pechini method (SG)

There has been an intense level of research activity on the development of luminescent materials by the sol–gel method [5, 6]. Figure 4.1.(a) presents the basic production cycle for sol-gel synthesis. Metal oxides, in the appropriate molar ratios, are dissolved in a nitric acid solution (which is less costly than buying metal nitrate powders). Citric acid, a chelating agent is then added along with ethylene glycol and polyethylene glycol (cross-linking agents). The solution is stirred at temperatures, usually below 100˚C, which produces a transparent gel. The gel is calcined at low temperature (~350˚C) to remove organics and residual water, resulting in a nanocrystalline powder. The particle size and morphology can be controlled by adjusting the

solvent and heating conditions, or by changing the precursors. A variety of stoichiometric, single phase materials can be simply prepared by this method, without the need for extensive grinding and milling. However, the phosphors can become contaminated with carbon due to the use of organic reagents and thus a pre-annealing step in air may be needed. Also, a reducing atmosphere may be required to obtain Eu^{2+} and Ce^{3+} activated phosphors.

4.1.3. Co-precipitation method (CP)

This method is widely used to prepare oxide- and (oxy)fluoride-based phosphors [7, 8]. Figure. 4.1.(b) shows the synthetic steps of this method. Precursors (e.g. metal nitrates, acetates or chlorides) are first dissolved in a solvent (e.g. water, N-N-dimethylformamide (DMF) or cyclohexane). Precipitating agents are then added and the cations form hydroxide, carbonate or fluoride compounds. Since the precursors should dissolve and the precipitate should not dissolve in the solvent, the solubility of both the precipitates and precursors in the solvent should be confirmed before starting the procedure. The precipitates are separated by filtering or centrifuging and then heat-treated to decompose the resulting hydroxide or carbonate. The powder is then annealed at high temperature to crystallize the powders. Because the use of expensive, high-purity rare-earth fluorides as starting materials are not required (as for SS reaction), this is the preferred method for producing complex fluorides. Smaller particle sizes and a homogeneous distribution of the activator ions can be achieved using this technique [7]. In addition, the particles prepared by this method have a uniform, narrow size distribution, as opposed to powders prepared by solid-state reaction synthesis. The particle size and morphology are dependent on the pH, precursor and solvent choice, precipitating agent, stirring rate and the order of addition of the compounds. The main drawbacks of this method are the difficulty in preparing chloride-based phosphors, due to the dissolution of precipitates (metal chlorides) in the solvent, and the additional high temperature annealing step required for the production of oxides.

4.1.4. Hydrothermal method (HT)

The hydrothermal method is a process that uses high temperature and pressure to precipitate materials directly from solution. A schematic representation of this method is shown in Figure 4.1.(c). This method makes use of the increased solubility of almost all inorganic substances in water at elevated temperatures and pressures and subsequent crystallization of the dissolved material from the solution [9]. By controlling the selection of the molecular precursor and other reaction parameters (time and temperature), high purity and homogeneously dispersed nanoparticles with a very narrow size distribution can be obtained. The main advantage of this technique is that despite the low synthetic temperatures, crystalline powders are obtained without the need for further heat-treatment. By changing the pH, precursor selection, and the reaction temperature, the size, phase, and morphology of the powders can be modified [9]. However, this method is generally applicable only for producing molybdates, borates and chloro(fluoro)phosphates, which can be obtained at a relatively low synthetic temperature (<800℃) [10]. In addition, special sealed vessels, which can be operated at very high temperature and pressure (usually around 500℃ and 340 atm) are required [11]. Furthermore, due to the small volume of the reaction vessels, mass production of phosphors is difficult.

4.1.5. Combustion method (CS)

Combustion synthesis is a popular method to rapidly produce multiconstituent oxides [12-14]. The products are generally chemically homogeneous, have fewer impurities, and have higher surface areas compared to solid state synthesized powders. The method involves igniting an aqueous solution of dissolved metal nitrates and a fuel (e.g. urea, carbohydrazide, glycine) at a low temperature (< 500˚C) and allowing the highly exothermic, oxidative reaction to occur, usually with an accompanying flame as shown in Figure 4.1.(d). This produces reaction temperatures of more than 1200˚C and the reaction time is usually less than 10 min [12]. Due to

the short duration at high temperatures, nanocrystalline powders are produced. However they are agglomerated into hard, sub-micron sized powders that are not easily separated. In order to improve purity, homogeneity and crystallinity of complex oxide powders, Garcia et al. [15] developed a new method using hydrazine as a fuel in a high-pressure reaction vessel. This method is superior because of: 1) increased personal safety due to the protection by the vessel; 2) total recuperation of the product; 3) more precise control of reaction parameters as it is possible to measure the temperature, pressure, and gas flow rates; and 4) a controlled atmosphere (reactive or inert). By this method, a variety of luminescent materials such as silicates, phosphates, borates, oxyflurorides, oxychlorides, and aluminates have been simply and expeditiously prepared.

4.1.6. Spray pyrolysis method (SP)

Spray pyrolysis is a technique used to synthesize a wide variety of high-purity, homogeneous ceramic powders with very uniform size and spherical morphology. The basic procedure is as follows as shown in Figure 4.2.(a). An aqueous solution with metal nitrate precursors is atomized into a series of tube furnaces. The aerosol droplets undergo evaporation and solute condensation within the droplet. They are dried, then thermolysis of the precipitate particle occurs at higher temperatures to form microporous particles. Finally, each microporous particle is sintered to form a dense particle. The particle size and morphology of the particles can be controlled by precursor selection, concentration, droplet size, and the residence time in the furnace [16]. However, this method possesses problems as hollow and porous particles often result, which will decrease the luminous intensity. To overcome this problem, a high temperature diffusion flame can be used. This new process is named flame spray pyrolysis [17, 18]. Figure 4.2.(b) shows a schematic drawing of the flame spray pyrolysis technique. Compared to conventional spray pyrolysis, flame spray pyrolysis has: 1) a higher operating temperature, 2) faster heating and cooling rates, and 3) easier introduction of the precursor into the hot reaction

zone (flame). Higher operating temperatures can potentially solve the problem of the production of microporous or hollow particles. By operating at a temperature higher than the melting point of the material, solid particles can be produced and particle homogeneity is improved. However, it is not always straightforward to produce multicomponent materials with a homogeneous chemical composition because the vapor pressure (related to reactant concentration), the thermal decomposition (chemical reaction) rate, the nucleation, and the particle-growing rate are different in the flame.

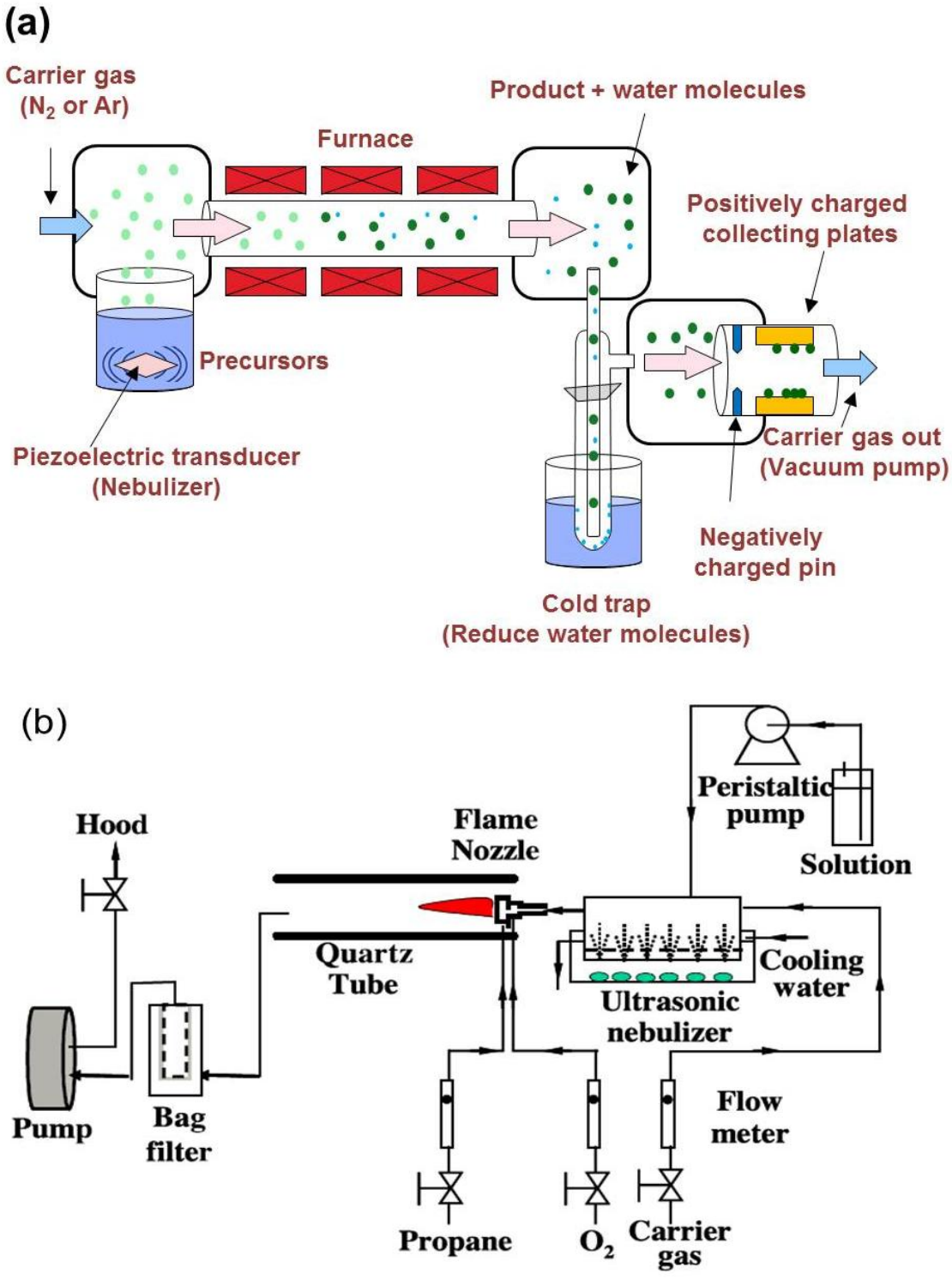

Figure 4.2. Schematic diagram of (a) conventional and (b) flame spray-pyrolysis. Taken from [17].

4.2. Characterization of luminescent materials

The crystallinity and phase identification of phosphors are analyzed by using powder X-ray diffraction (XRD). The morphology and particle size of nanophosphors were examined using field emission-scanning electron microscopy (FE-SEM). Photoluminescence (PL) measurements were taken using a Jobin-Yvon Triax 180 monochromator and Spectrum One charge-coupled device detection system, using a 450 W Xe lamp as the excitation source.

The quantum efficiency of the phosphors was measured. The DeMello method [19] was used to determine the individual quantum efficiencies as shown in Figure 4.3. A 400 nm laser diode is used as the excitation source, and is aimed through a 10 mm hole drilled in the side of a 12” sphere. The sample powders were dispersed in silicone in an approximately 3 weight percent, usually about 0.015 g of powder to 0.5 g of silicone. A small, 5 mm by 10 mm, rectangle was cut from the large piece and suspended in the center of the sphere. Three measurements are taken: one without the sample in the sphere, one with the sample in the sphere but with indirect excitation from the laser, and finally with the sample directly excited by the laser. The emission profiles from the powders are recorded, and the curves are corrected for the response of the system in photons. The curves generated by the phosphors are separated into the excitation region, encompassing the laser emission, and the emission region, containing the emission from the phosphor. These curves are then integrated and the quantum efficiency is calculated using the method described in [19].

A Janis cryostat (VPF-100) was fit into the sample chamber of the Fluorolog-3 system, and a pulsed Nano-LED was used as the excitation source. The LED was centered at 365 nm, the excitation monochromator was set to 380 nm, and the slits were opened to a 10 nm band pass. The time range was set at 3.2 μs and the pulse rate was set at 250 kHz. The emission monochromator was set at 450 nm to correspond to the peak emission, and the slits were opened to 8nm band pass. The scan was set to stop, once the peak counts reached 5000. The sample was

cooled down to 80 K with liquid nitrogen, and the first scan was started. Once the peak height was reached, the sample temperature was raised to 100 K and the second scan was started. After 100 K, the sample was then raised in 25 K increments to a final temperature of 500 K.

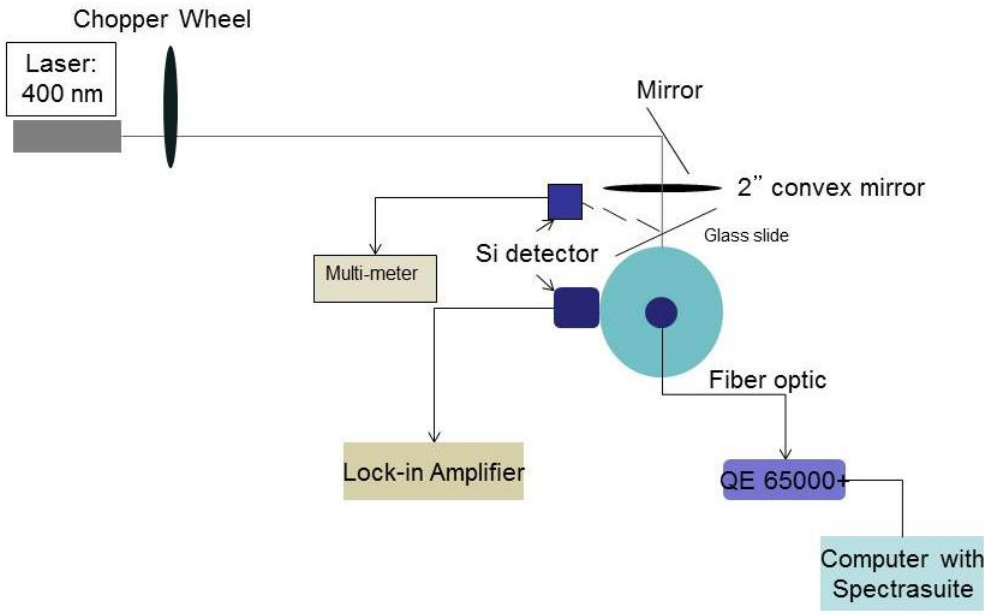

Figure 4.3. The schematic of measurement for quantum efficiency followed by DeMello method [19].

4.3. Experimental procedure for electophoretic deposition

The phosphor powders used in this study were Eu^{2+}-activated $Sr_{2-x}Ca_xSi_5N_8$, Ba_2SiO_4, $LiCaPO_4$, $(Sr_{0.75}Ba_{0.25})_2SiO_4$ and $(Sr_{0.5}Ba_{0.5})_3SiO_5$, synthesized by solid state reaction, that emit red, green, blue, yellow and orange light, respectively, under 380 nm excitation. EPD was carried out in a bath consisting of the phosphor powders, $Mg(NO_3)_2{\cdot}6H_2O$, isopropyl alcohol (IPA) and glycerin. The $Mg(NO_3)_2{\cdot}6H_2O$ concentration ranged from approximately 10^{-5} to 10^{-3} M, as determined by our previous work [20]. To enhance the dispersion of particles and adhesion strength, 2 vol.% glycerin was added to the bath. The zeta potentials of the powders were measured in a diluted suspension with various magnesium nitrate concentrations in IPA and 2 vol.% glycerin with a Zeta Plus meter (Brookhaven Instruments Corporation, Holtsville, NY).

An ITO-coated glass slide (2.5 cm × 5.1 cm × 1.1 mm, 70 ohms/sq., Bayview Optics, Dover-Foxcroft, ME) was used as the cathode, and an aluminum sheet was used as the anode. The deposition area was 2.5 cm × 2.5 cm. The electrodes were placed vertically and parallel to each other in a suspension with 1 cm separation as shown in Figure 4.4. A voltage of 50-100 V was applied by a power supply for 1 min - 8 min to give a deposit thickness ranging from ~ 10 μm - 25 μm. The maximum applied voltage was 100V because the deposited film quality was poor when a higher applied voltage was used [21]. After the deposition process, the deposited samples were removed from the bath and dried in air.

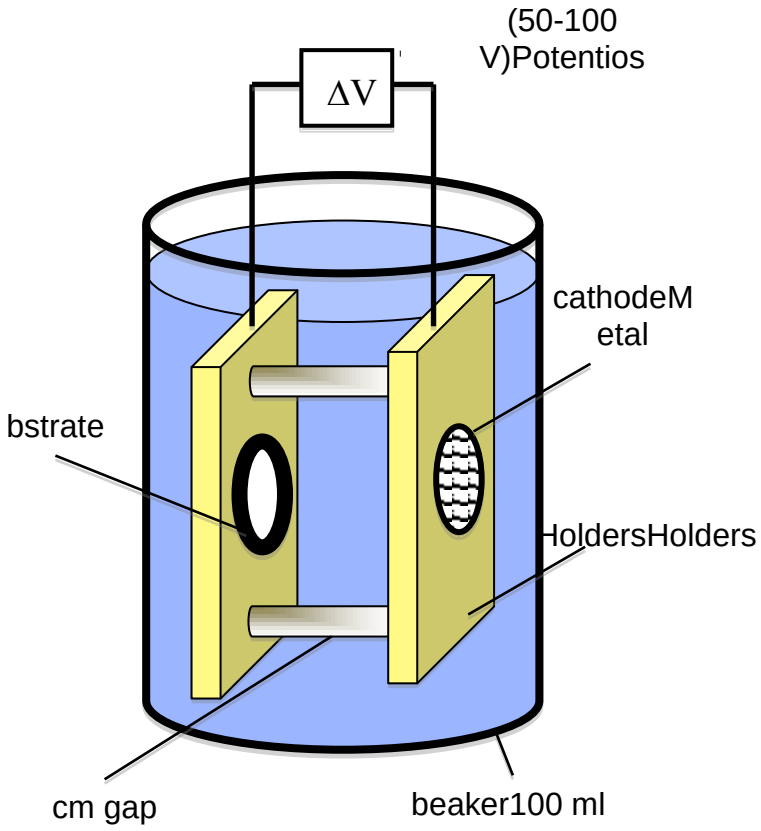

Figure 4.4. Schematic diagram of the electrophoretic bath set-up. Phosphor powders are suspended in an electrolytic solution. The application of a voltage causes the particles to migrate and deposit on the substrate.

For deposition of each phosphor composition, a 5 g/L of powder was dispersed in 100 ml of IPA with $Mg(NO_3)_2 \cdot 6H_2O$ and glycerin. The nitrate concentration was chosen to obtain a zeta potential of ~30 mV - 40 mV for each phosphor. The zeta potential was negative at a low salt concentration. As the salt concentration increased to around 10^{-4} M, the zeta potential became positive. In the case of the phosphor blends, a 5 g/L of a mixture of phosphor powders was ground lightly by a mortar and pestle and then dispersed in 100 ml of IPA. Sonication of the suspension for 1 h was used to improve the dispersion of the powders in the suspension and assure the complete dissolution of $Mg(NO_3)_2 \cdot 6H_2O$.

The blend compositions were chosen to generate white light. At first, the phosphor blend was determined by a software simulation for an initial ratio (by OSRAM-Slyvania). This blend was formulated and the resulting emission spectra of the blend by excitation from a UV LED and CIE coordinates were used to modify the blend until the formulation met the desired CCT, CRI and distance from the black body locus. Two different blends were chosen. One was a blend of three phosphor composition (blue-, yellow- and orange-emitting) and another one was a blend of four phosphors (blue-, green-, orange- and red-emitting). However, the real compositions of the blends were determined by experiments due to different deposition rates of phosphor components.

Blended phosphor films were prepared from a single deposition (5 min) using a bath with a mixture of phosphors. The three phosphor blend contained (by weight) 63 % blue-, 15 % yellow- and 22 % orange-emitting powders and the four phosphor blend contained 70 % blue-, 13 % green-, 5 % orange- and 12 % red-emitting powders.

The other approach used was sequential deposition using different individual phosphor suspensions. The light emission of the sequentially-deposited films was changed by altering the thickness and the order of the sequentially-deposited phosphors. Two sequential depositions were performed using a bath of a mixture of red- and orange-emitting phosphors and a separate bath of

green- and blue-emitting phosphors. First, red/orange (1:1 weight ratio) was deposited and then green/blue (2:3 weight ratio) was deposited. The deposition time in the first bath was for 1-3 min and the time in second bath was increased to 5-8 min to overcome the decrease of electric field on the electrode due to the resistance of the first layer.

The deposits were analyzed in terms of their thickness, PL spectra, CCT and CRI. The PL emission spectra were taken using a Jobin Yvon Triax 180 monochromator, SpectrumOne charge-coupled device (CCD) detection system and a 380 nm UV as the excitation source. The CCT and CRI were calculated from the measured PL spectrum of the phosphors using ColorCalculator software developed by OSRAM SYLVANIA Inc. (downloaded from https://www.sylvania.com). The thicknesses of the films and average particle sizes were estimated from micrographs taken by a field emission scanning electron microscope (FEI-XL30, FEI Company, Hillsboro, OR).

References

1. E. Danielson, J.H. Golden, E.W. McFarland, C.M. Reaves, W.H. Weinberg, X.D. Wu, "A combinatorial approach to the discovery and optimization of luminescent materials" Nature, 389, 944-948 (1997).

2. O. Ozuna, G.A. Hirata, J. McKittrick, "Luminescence enhancement in Eu^{3+}-doped α- and γ-Al_2O_3 produced by pressure-assisted low-temperature combustion synthesis", Appl. Phys. Lett., 84, 1296 (2004).

3. J.W.H. Van Krevel, H.T. Hintzen, R. Metselaar, A. Meijerink. "Long wavelength Ce emission in Y–Si–O–N materials", J. Alloy. Comp., 268, 272-277 (1988).

4. K. Kinsman, J. McKittrick, E. Sluzky, K. Hesse, "Phase development and luminescence in Chromium-doped yttrium aluminum garnet (YAG:Cr) phosphors, J. Am. Ceram. Soc. 77 (1994) 2866-2872.

5. J.K. Park, M.A. Lim, C.H. Kim, H.D. Park, J.T. Park, S.Y. Choi. "White light-emitting diodes of GaN-based Sr_2SiO_4 :Eu and the luminescent properties", Appl. Phys. Lett., 683, 683-685 (2004).

6. S. Yao, Y. Li, L. Xue, Y. Yan, "A promising blue–green emitting phosphor for white light-emitting diodes prepared by sol–gel method", J. Alloy. Comp. 1-2 264-267 (2010).

7. Q.Y. Zhang, X.Y. Huang, "Recent progress in quantum cutting phosphors" Prog. Mater. Sci. 55 353-427 (2010b).

8. Y. Zhou, J. Lin, M. Yu, S.Wang, H. Zhang,"Synthesis dependent luminescence properties of $Y_3Al_5O_{12}$:Re^{3+} (Re=Ce, Sm, Tb) phosphors, Mater.Lett 56 628-636 (2002).

9. X.P. Chen, X.Y. Huang, Q.Y. Zhang, "Concentration-dependent near-infrared quantum cutting in $NaYF_4$:Pr^{3+}, Yb^{3+} phosphor" J. Appl. Phys. 106 063518-063521 (2009).

10. T. Kim, S. Kang, "Hydrothermal synthesis and photoluminescence properties of nano-crystalline $GdBO_3$:Eu^{3+} phosphors", Mater. Res. Bull., 40, 1945 (2005)

11. R.J. Xie, N. Hirosaki, Y. Li, T. Takeda, "Rare-Earth Activated Nitride Phosphors: Synthesis, Luminescence and Applications", Materials 3 3777-3793 (2010).

12. J. McKittrick, L.E. Shea, C.F. Bacalski, E. J. Bosze, "The influence of processing parameters on luminescent oxides produced by combustion synthesis", Displays 19 169-172 (1999).

13. L.E. Shea, J. Mckittrick, O. A. Lopez, E. Sluzky, “Synthesis of Red-Emitting, Small Particle Size Luminescent Oxides Using an Optimized Combustion Process”, J. Am. Ceram. Soc., 79 3257-3265 (1996).

14. E.J. Bosze, J. Mckittrick, G. A. Hirata, “Investigation of the physical properties of a blue-emitting phosphor produced using a rapid exothermic reaction”, Mater. Sci. Eng. B 97 265-274 (2003).

15. R. Garcia, G. A. Hirata, J. Mckittrick, “New combustion synthesis technique for the production of $(In_xGa_{1-x})_2O_3$ powders: Hydrazine/metal nitrate method”, J. Mater. Res. 16 1059-1065 (2001).

16. H.S. Kang, Y.C. Kang, K. Y. Jung, S.B. Park, “Eu-doped barium strontium silicate phosphor particles prepared from spray solution containing NH_4Cl flux by spray pyrolysis”, Mater. Sci. Eng. B. 121 81-85 (2005).

17. Y.C. Kang, D.J. Seo, S.B. Park, H.D. Park,” Morphological and Optical Characteristics of Y_2O_3:Eu Phosphor Particles Prepared by Flame Spray Pyrolysis”, Jpn. J. Appl. Phys. 40 4083-4085 (2001).

18. D. Dosev, B. Guo, I.M. Kennedy, “Photoluminescence of Eu^{3+}:Y_2O_3 as an indication of crystal structure and particle size in nanoparticles synthesized by flame spray pyrolysis”, J. Aerosol. Sci. 37 402-412 (2006).

19. J.C. DeMello, F. Wittman, and R.H. Friend, "An improved experimental determination of external photoluminescence quantum efficiency", Adv.Mat., 9, (1997).

20. M. J. Shane, J. B. Talbot, E. Sluzky, and K. R. Hesse, Colloids and Surfaces, 96, 301 (1994).

21. R. Basu, C. Randall and M. Mayo, J. Am. Ceram. Soc., 84(1), 33–40 (2001).

Chapter 5. Comparison of luminescent properties of $Y_2O_3:Eu^{3+}$ and $LaPO_4:Ce^{3+}$, Tb^{3+} phosphors prepared by various synthetic methods

5.1. Abstract

The crystallite and particle sizes, morphology and corresponding photoluminescence (PL) properties of nanocrystalline phosphors $Y_2O_3:Eu^{3+}$ and $LaPO_4:Ce^{3+}$, Tb^{3+}, produced by combustion, co-precipitation, hydrothermal, sol-gel, and spray pyrolysis synthesis protocols, are compared. For $Y_2O_3:Eu^{3+}$, the particles made by a sol-gel method showed the highest PL emission intensity with a 26 nm crystallite size and nearly spherical morphology. Spray-pyrolysis particles have perfect spherical morphology with ~0.6 µm diameter particle size, but produced the lowest PL emission intensity with a crystallite size of 13 nm. For $LaPO_4:Ce^{3+}$, Tb^{3+}, the co-precipitation method produced particles with ~0.3 µm diameter with the highest PL emission intensity with a crystallite size of 33 nm and the synthesized powders possess a similar spherical morphology to that of $Y_2O_3:Eu^{3+}$ particles produced by the sol-gel method. The PL emission intensity increased with increasing crystallite size, but was found not to be dependent upon particle size. In general, phosphors particles with a relatively large crystallite size with a spherical and agglomerated morphology are favored for emitting the highest PL intensity.

5.2. Introduction

Understanding and enhancing the luminescence of nanophosphors is important for applications such as displays, sensors and solid-state lighting [1-3]. Among the numerous phosphors, europium-activated yttrium oxide ($Y_2O_3:Eu^{3+}$) has been widely used as a red-emitting phosphor in fluorescent lamps, high resolution projection devices and displays [4-5]. $Y_2O_3:Eu^{3+}$ phosphors show a strong 611 nm red emission from the $^5D_o \rightarrow ^7F_2$ transition and weaker emissions from the $^5D_o \rightarrow ^7F_{1,3}$ transitions of Eu^{3+} [6-7]. Cerium and terbium-activated lanthanum phosphate ($LaPO_4:Ce^{3+}$, Tb^{3+}) displays an efficient ~543 nm green emission of Tb^{3+} under deep UV radiation, which are widely used as a green-emitting phosphors in fluorescent lamps [8]. UV

excitation of Ce^{3+} occurs through a $4f^1 \rightarrow 4f^0 5d^1$ transition and then energy transfer from Ce^{3+} to Tb^{3+} arises, resulting in a Tb^{3+} emission from the $^5D_4 \rightarrow {}^7F_J$ (J = 0-6) relaxation.

$Y_2O_3:Eu^{3+}$ and $LaPO_4:Ce^{3+}$, Tb^{3+} have been synthesized through various methods such as spray pyrolysis [9-10], microemulsion [11-12], combustion [13-14], sol gel [15-16], hydrothermal [17-18], homogeneous precipitation [19-20], and co-precipitation [21-22]. Among the various routes to synthesize $Y_2O_3:Eu^{3+}$ and $LaPO_4:Ce^{3+}$, Tb^{3+}, they can be divided into two groups according to the precursor, which can be a precipitate or a gel. The microstructure and physical property of particles largely depend on the characteristics of the precursors in the controlled synthesis and thermal decomposition conditions. These conditions have an effect on the morphology, crystallite and particle size, and photoluminescence (PL) emission intensity of the resulting phosphors. A crystallite is the smallest detectable single crystal and its size is usually estimated from X-ray diffraction line broadening analysis based on the Scherrer's formula or from transmission electron microscope studies. A particle consists of multiple crystallites that are strongly bound together. These sizes are measured by scanning electron microscopy (SEM) or from light scattering methods. Agglomerates are a number of particles that are weakly or strongly held together and their size can be measured using SEM or light scattering methods.

There have been studies that report the effects of crystallite and particle size on PL emission intensity for numerous phosphors each synthesized by a sole method. Han et al. [23] studied the nano- and sub-micron sized $(Ba_{1-x}Sr_x)_2SiO_4:Eu^{2+}$ prepared by a co-precipitation method and found that the PL intensity increased with increasing crystallite size, which increased after annealing at progressively higher temperatures. Jung et al. [24] found a linear increase of emission intensity of spray pyrolyzed $Y_2O_3:Eu^{3+}$ with increasing crystallite size (25-60 nm). Wang et al. [25] prepared submicron $Y_2O_3:Eu^{3+}$ powders of different crystallite and particle sizes through spray pyrolysis by varying the synthesis temperatures, and also found a linear increase of PL emission intensity increasing crystallite sizes (9 nm to 55 nm). They also observed an increase

in PL emission intensity when particle size was increased from 200 to 500 nm with a constant crystallite size, but PL emission intensity leveled when the particle size was 500 nm and greater. However, it was concluded that the crystallite size had a more important role in affecting PL emission intensity than the particle size. Jung et al. [26] studied the effects of particle size and crystallite size on PL emission intensity for $BaMgAl_{10}O_{17}:Eu^{2+}$ phosphors prepared by spray pyrolysis and found that larger crystallite sizes led to higher PL emission intensity. They found PL emission intensity increasing for particles up to ~3 µm in size and leveled off for particle sizes of 4 µm to 12 µm, similar to results of Wang et al. [25], although the leveling off occurred at a larger particle size. From these reports, it has been demonstrated that as both the crystallite and particle size increases, the PL emission intensity increases. With smaller crystallites, the probability for non-radioactive recombination without releasing photons becomes higher due to the increased number of atoms in grain boundaries and on the surface, lowering the light generation efficiency compared to larger crystallites. The PL intensity increases up to a certain particle size and remains constant beyond that size. This is likely due to the increased scattering of incident light inside particles as the particle size becomes large and particles agglomerate.

There have been studies to compare the effect of different synthesis methods on PL emission intensity [27-34]. The PL from $SrIn_2O_4:Eu^{3+}$ synthesized by solid state and combustion reactions was compared and solid state reacted powders had a higher emission intensity, which was attributed to a larger crystallite size [27]. $Y_2O_3:Eu^{3+}$ was prepared by solid state and co-precipitation reactions annealed at different temperatures, and it was found that co-precipitated powders annealed at high temperature had the highest emission intensity due to those powders having the largest crystallite size [28]. Sol gel prepared powders of $Mg_2TiO_4:Mn^{4+}$ and $SrMoO_4:Eu^{3+}$ had a higher PL emission intensity compared to solid state reacted powders [29-30]. This was attributed to a higher purity and more uniform activator distribution in the sol gel powders. $Li_2SrSiO_4:Eu^{2+}$ phosphors prepared by the sol gel route and solid state reaction showed

that the sol gel powders had a higher emission intensity, which was assigned to defects introduced by Li volatilization during solid state reaction synthesis [31]. Nano-crystalline $Ba_3MgSi_2O_8:Eu^{2+}$, Mn^{2+} synthesized by a sol–gel method show higher color rendering and better color temperature in comparison with the samples prepared by high temperature solid-state reaction method [32]. $Y_3Al_5O_{12}:Cr^{3+}$ phosphors prepared by combustion and solid state reactions had similar emission intensities, but only after high temperature annealing of the combustion powders [33]. $Zn_3V_2O_8$ synthesized by different methods had emission intensities in the order: combustion > hydrothermal > sol-gel > solid state, which was attributed to the uniform, spherical morphology of the powders prepared by combustion synthesis [34]. These results demonstrate that the synthesis method strongly influences the PL emission intensity.

There are no direct comparisons of the luminescence properties of phosphors synthesized by a large variety of methods and their relationship to the crystallite and particle sizes and morphology. In this report, a simple oxide, $Y_2O_3:Eu^{3+}$, and a phosphate, $LaPO_4:Ce^{3+}$, Tb^{3+}, were synthesized by various methods to investigate the effect of powder morphology, crystallite and particle sizes on the PL emission intensity.

5.3. Experimental

The starting materials were yttrium(III) nitrate hexahydrate ($Y(NO_3)_3 \cdot 6H_2O$, Sigma Aldrich), europium(III) oxide (Eu_2O_3, Alfa Aesar), citric acid ($C_6H_8O_7 \cdot H_2O$, EMD Chemicals), ethylene glycol (C_2H_6OH, Fischer Scientific), polyethylene glycol (PEG, $(C_2H_4O)_nH_2O$, Sigma Aldrich), nitric acid (68 – 70%, EM Science), ammonium hydroxide (NH_4OH, Puritan Products), urea (CH_4N_2O, Fisher Scientific), terbium (III) nitrate hexahydrate ($Tb(NO_3)_3 \cdot 6H_2O$, Sigma-Aldrich), cerium (III) nitrate hexahydrate ($Ce(NO_3) \cdot 6H_2O$, Alfa Aesar), and lanthanum (III) nitrate pentahydrate ($La(NO_3)_3 \cdot 5H_2O$, Sigma Aldrich). All materials were used without further purification. The starting powders for $Y_2O_3:Eu^{3+}$ consisted of $Y(NO_3)_3 \cdot 6H_2O$ and Eu_2O_3 (molar

ratio Y/Eu = 0.95/0.05) and $LaPO_4:Ce^{3+}$, Tb^{3+} consisted of La_2O_3, Tb_4O_7, $Ce(NO_3)_3 \cdot 6H_2O$ and $(NH_4)_2HPO_4$ (molar ratio La/Tb/Ce/P = 0.9/0.025/0.075/1). Solutions for both compositions were made with a 1:1 volume ratio of water and nitric acid and stirred for 30 min until a clear solution was observed. The starting solutions for $Y_2O_3:Eu^{3+}$ and $LaPO_4:Ce^{3+}$, Tb^{3+} will be named solution A (Y molar amount = 0.95) and B (La molar amount = 0.9), respectively.

1. Sol-gel/Pechini method

Citric acid (CA) (0.93 g), which acts as chelating agent for the metal ions, and 2.5 g of polyethylene glycol (PEG), which acts as a cross-linking agent, were added to solution A. To solution B, 0.90 g of CA and 2.0 g of PEG were added. The solutions were continually stirred for 10 hours at 80 ˚C to form a transparent gel. The gels were preheated at 350 ˚C for 1 hr in air to evaporate residual water until a black powder remained. The powders from solution A was annealed at 800 ˚C for 1 hr, and from solution B was annealed at 1000 ˚C for 1 hr to remove organic materials, resulting in phosphor powders.

2. Combustion method

Urea was added as fuel in the amount of 0.88 g for solution A and 1.28 g for solution B. After the addition of urea, the beakers were directly placed inside a preheated furnace at 500 ˚C until the mixture started to boil and subsequently produced a flame that was sustained for a few seconds. The beakers were taken out of the furnace and allowed to cool to room temperature. The resulting powders were collected and transferred to ceramic crucibles. Powders from solution A were heated at 800 ˚C for 1 hr in air, and powders from solution B were heated at 1000 ˚C for 1 hr in air to produce phosphors.

3. Hydrothermal method

Solution A was heated at 100 ˚C for 10 hr until all residual acid was evaporated from the solution and a transparent solid was obtained. Water (25 ml) was added to the solid under stirring conditions until all of the solid dissolved. To produce the precipitate, NH_4OH was added dropwise until the pH was ~6. The slurry was then transferred into a closed Teflon pressure vessel and thermally treated at 130 ˚C for 24 hours. The resulting solution was then filtered, dried at room temperature, and annealed at 800˚C for 1 hour in air to further crystallize the powders. For solution B, NH_4OH was added dropwise until the pH was 5-6. The slurry was then transferred to the Teflon pressure vessel and treated at 130 ˚C for 24 hours. The heated solution was then filtered, dried at room temperature for 10 hours, and annealed at 1000 ˚C for 1 hour for further crystallization of the phosphor powders.

4. Co-precipitation method

To create precipitates for solutions A and B, the same steps were taken up to control the pH as in the hydrothermal method. Instead of annealing in the pressure vessel, both solutions were filtered and dried at room temperature for 10 hours. The resulting powders from solution A were annealed at 800 ˚C for 1 hour in air, and those from solution B were annealed at 1000 ˚C for 1 hour in air.

5. Spray-pyrolysis method

Mists were generated from solution A by a single 2.4 MHz ultrasonic nebulizer (Sonaer Ultrasonics, Farmingdale, NY) which was then directed into a tube furnace operating at 800 ˚C using argon as carrier gas. The flow rate was set to a range of 0.1 - 0.5 $Lmin^{-1}$ to control the residence time of the mist in the heating zone to 5-10 s. After passing a heat sink, the particles were collected from a charged plate at the end of the tube. The same process was used for solution B with the tube furnace operating at 1000 ˚C.

6. Characterization

All particles were slightly ground using a mortar and pestle before analysis. The crystallite sizes were determined from X-ray diffraction (XRD) peak broadening analysis. The particles were examined using a field emission scanning electron microscope (SEM) (FEI-XL30, FEI Company, Hillsboro, OR). The particle sizes were determined using the intercept method, measuring up to 50 particle diameters. PL emission spectra were taken using a Jobin-Yvon Triax 180 monochromator and SpectrumOne charge-coupled device detection system, which was shared with the PL system that uses a 450 W Xe lamp as the excitation source. An excitation wavelength of 276 nm was used for $LaPO_4:Ce^{3+}$, Tb^{3+} and 253 nm for $Y_2O_3:Eu^{3+}$. These excitation wavelengths were chosen as they produced the highest PL emission intensity.

5.4. Results and Discussion

Figure 5.1. shows the XRD patterns of the $Y_2O_3:Eu^{3+}$ powders produced using various methods, each post-annealed at 800˚C in air. All the diffraction peaks can be indexed to $Y_2O_3:Eu^{3+}$ compatible with JCPDS No. 43-1036 for Y_2O_3 with a cubic structure. The peak positions for all synthetic methods are the same, indicating the same Eu^{3+} content. Eu^{3+} substitutes for Y^{3+} and has a larger ionic radius, which would shift the XRD peaks if the Eu^{3+} concentration were not the same. Figure 5.2. shows the XRD patterns of the $LaPO_4:Ce^{3+}$, Tb^{3+} particles prepared by various methods, each post-annealed at 1000˚C in air. All five samples exhibit the characteristic diffraction peaks of the monoclinic structure of $LaPO_4$ (JCPDS No. 32-0493), with the peak positions the same, except for the spray pyrolyzed powders, which appears to have slightly higher activator content. No traces of impurity phases were observed in the XRD patterns, indicating a high purity for all the samples. However, it is clear from the XRD patterns that there are different magnitudes of peak broadening, showing that the crystallite size varied with each synthesis method.

Table 5.1. Crystallite and particle sizes and normalized photoluminescence emission intensity for each synthesis method. PL for $Y_2O_3:Eu^{3+}$ was normalized to the sol gel (SG) intensity (highest) and $LaPO_4:Ce^{3+}$, Tb^{3+} was normalized to the co-precipitated (CP) intensity (highest).

	$Y_2O_3:Eu^{3+}$			$LaPO_4:Ce^{3+},Tb^{3+}$		
Method	Crystallite size (nm)	Particle size (μm)	I/I_{SG}	Crystallite size (nm)	Particle size (μm)	I/I_{CP}
Combustion	18.0	1.64 ± 0.57	0.87	39.8	2.74 ± 0.45	0.77
Co-precipitation	28.2	0.32 ± 0.15	0.71	32.8	0.33 ± 0.07	1.00
Hydrothermal	23.7	0.95 ± 0.08	0.40	22.3	0.31 ± 0.10	0.93
Sol gel	26.3	2.19 ± 0.54	1.00	41.7	1.56 ± 0.52	0.89
Spray-pyrolysis	13.2	0.56 ± 0.18	0.32	14.1	0.76 ± 0.05	0.47

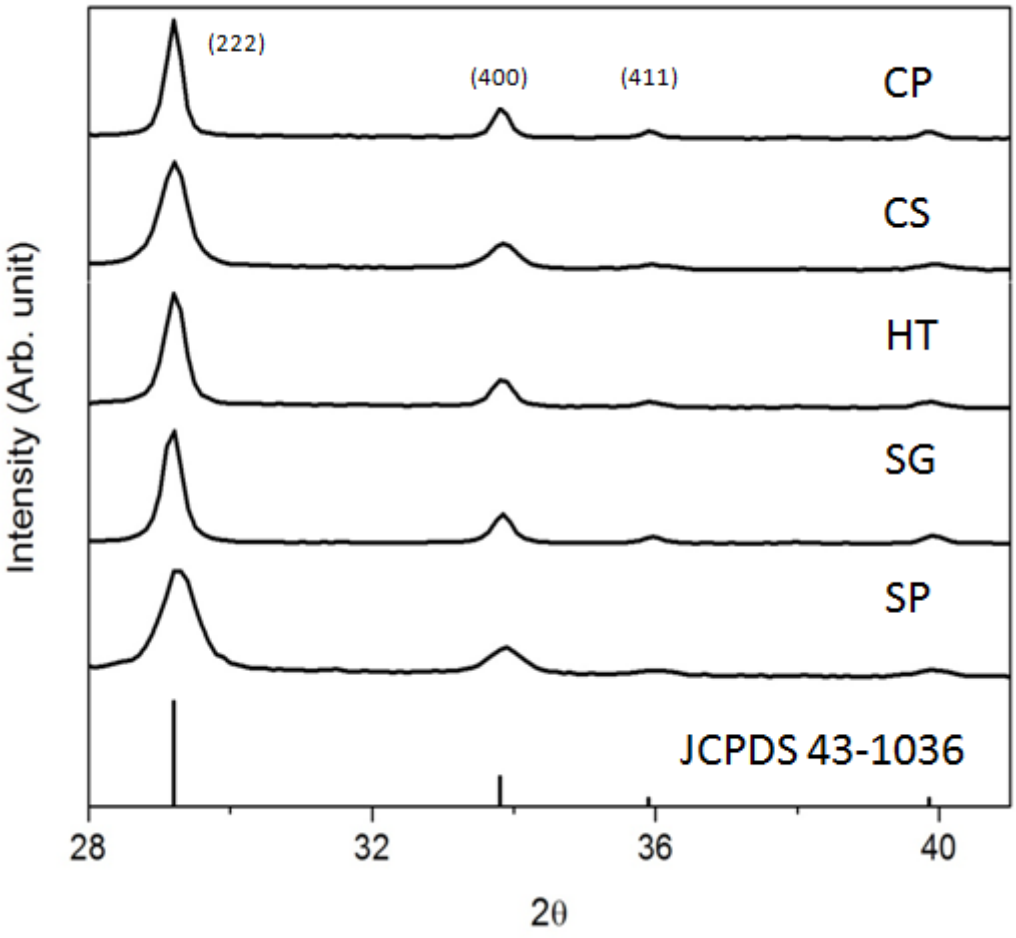

Figure 5.1. XRD of Y_2O_3:Eu^{3+} prepared by co-precipitation (CP), combustion (CS), hydrothermal (HT), sol-gel (SG), and spray pyrolysis (SP), compared with JCPDS card #43-1036 for cubic Y_2O_3.

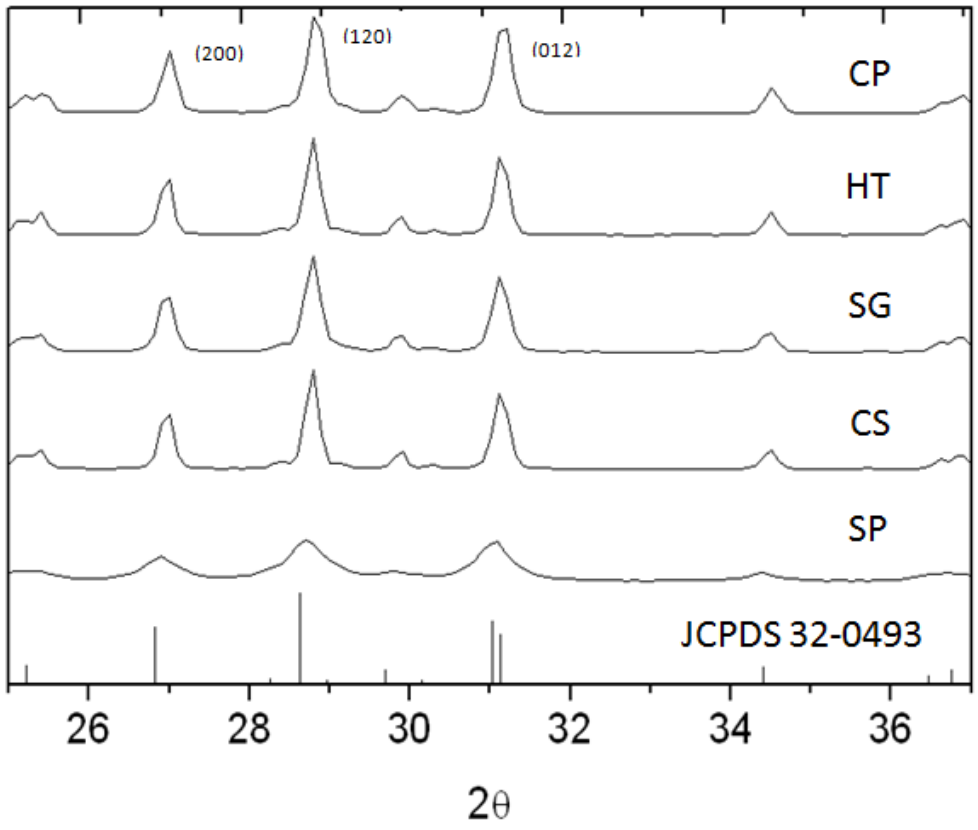

Figure 5.2. XRD patterns of $LaPO_4:Ce^{3+}$, Tb^{3+} prepared by co-precipitation (CP), combustion (CS), hydrothermal (HT), sol-gel (SG), and spray pyrolysis (SP), compared with JCPDS card #32-0493 for monoclinic $LaPO_4$

The crystallite size was calculated using the Scherrer formula:

$$D = \frac{0.9\lambda}{\beta cos\theta}$$

where λ = 0.154 nm (x-ray wavelength), β is the line broadening at full-width half-maximum intensity, θ is the Bragg angle, and D is the mean size of the crystallites. The results are shown in Table 5.1. The crystallite sizes of Y_2O_3:Eu^{3+} particles range from 13.2 nm by spray-pyrolysis to 28.2 nm by co-precipitation, whereas for $LaPO_4$:Ce^{3+}, Tb^{3+} particles, crystallite sizes ranged from 14.1 nm by spray-pyrolysis to 41.7 nm by sol-gel.

Each synthesis method produced different particle sizes and morphologies unique to the method. Figure 5.3.(a) shows a SEM micrograph of Y_2O_3:Eu^{3+} particles prepared by co-precipitation, which were agglomerated with particle diameters of ~0.3 µm. The morphology is significantly different for the particles prepared by the hydrothermal method, as shown in Figure 5.3.(b). Most of the particles are not spherical, but exhibit a needle-like morphology of ~ 900 nm in length and 40-50 nm in width. In Figure 5.3.(c) the sol-gel particles have irregular shape with an average particle size of ~2.2 µm. In Figure 5.3.(d) the particles prepared by combustion synthesis also have an irregular shape with an average size of ~1.6 µm. Figure 5.3.(e) shows the spray-pyrolysis particles with a spherical morphology with diameters of ranging from 280-640 nm.

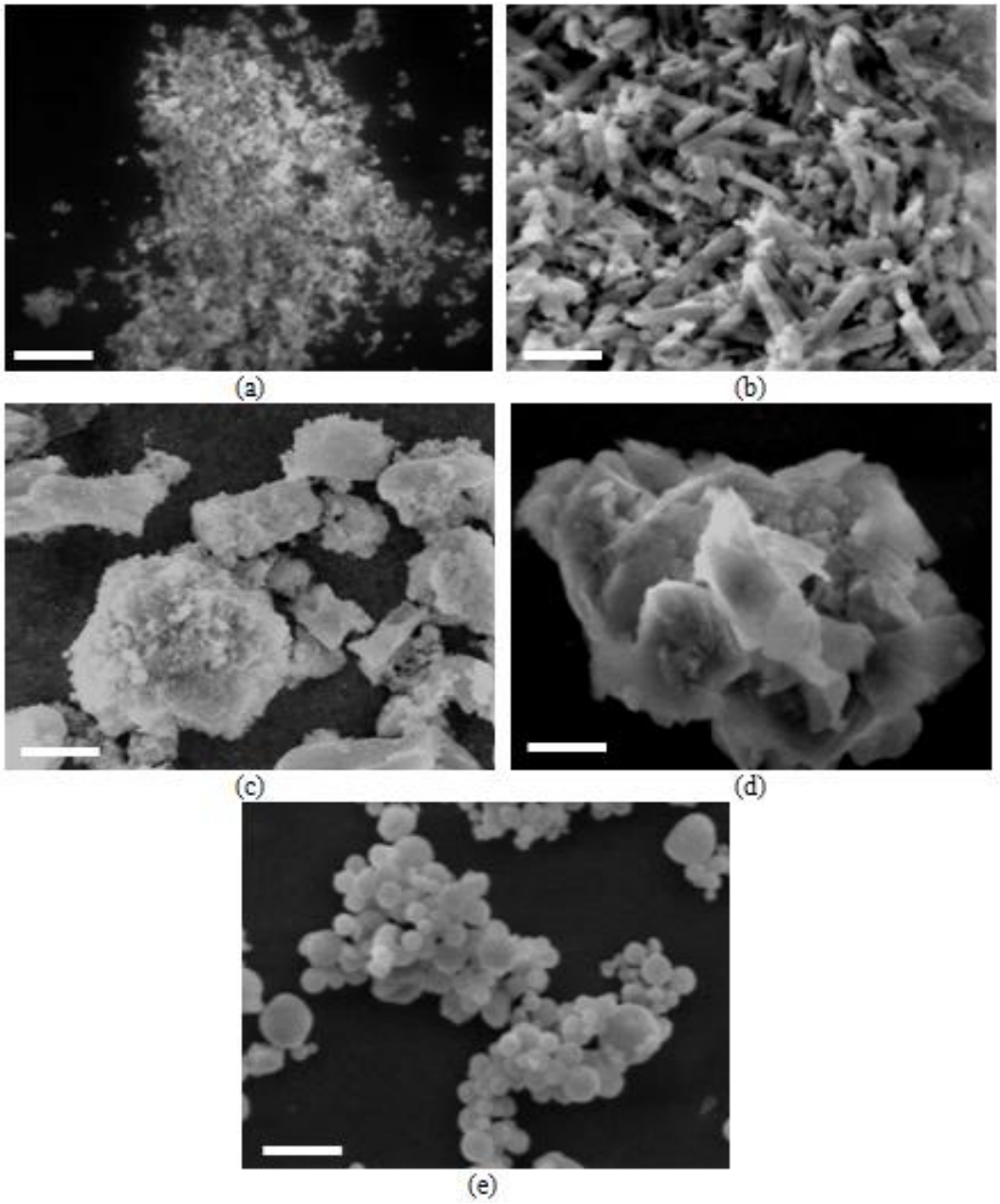

Figure 5.3. SEM micrographs of $Y_2O_3:Eu^{3+}$ produced by: (a) co-precipitation; (b) hydrothermal; (c) sol-gel; (d) combustion; (e) spray pyrolysis. Bar = 2 µm.

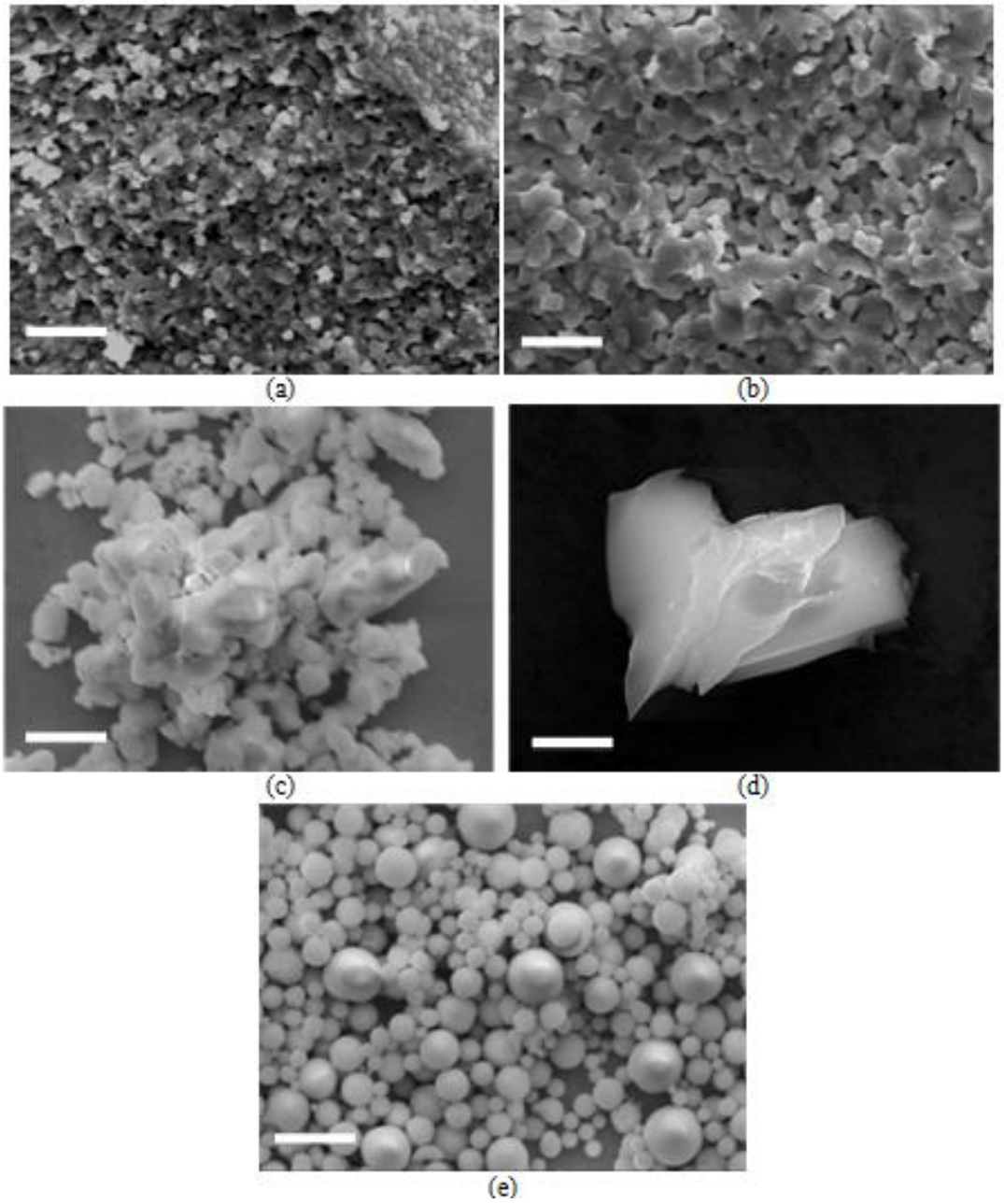

Figure 5.4. SEM micrographs of $LaPO_4$:Ce^{3+}, Tb^{3+} produced by: (a) co-precipitation; (b) hydrothermal; (c) sol-gel; (d) combustion; (e) spray-pyrolysis. Bar = 2 µm.

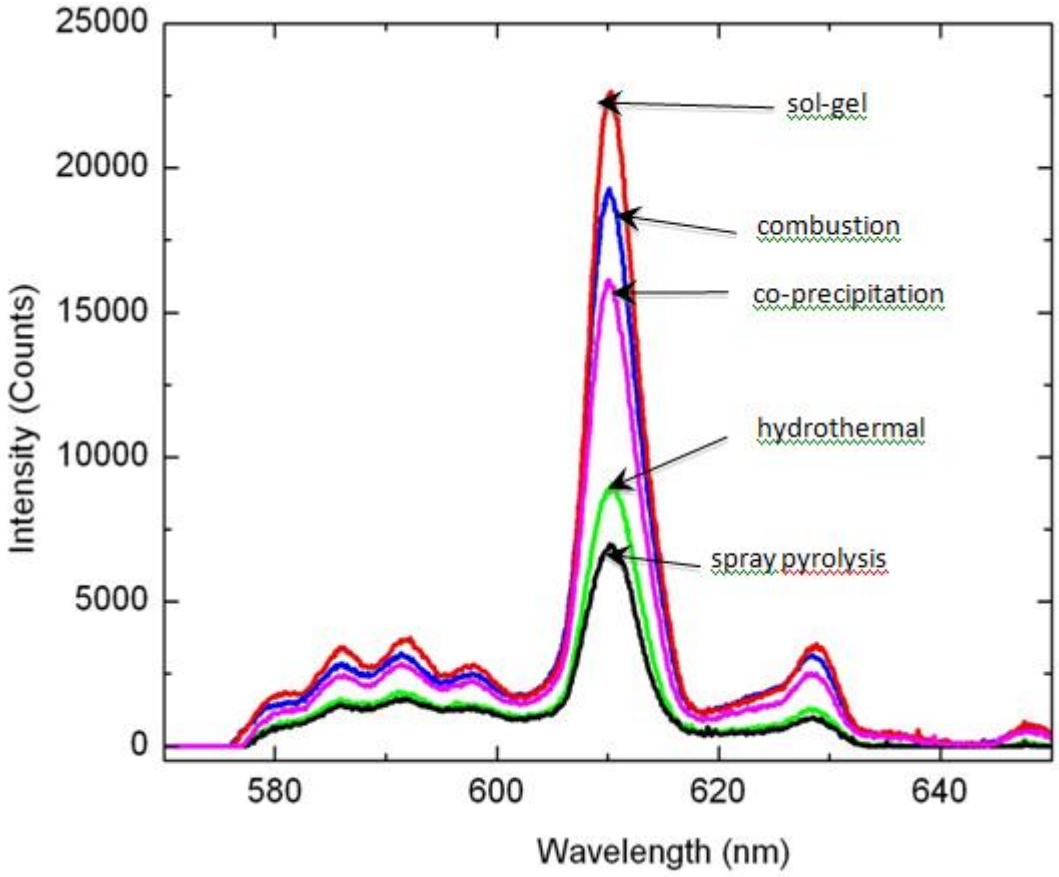

Figure 5.5. Photoluminescence emission spectra of Y_2O_3:Eu^{3+} produced by different synthesis methods.

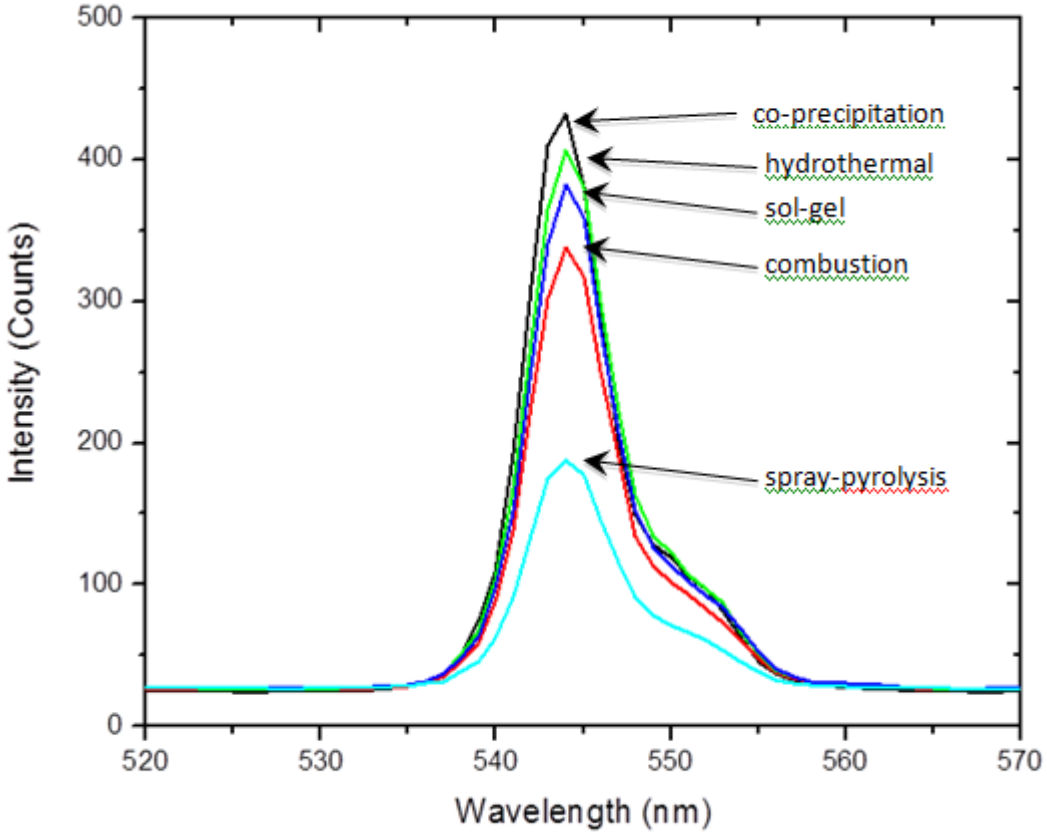

Figure 5.6. Photoluminescence emission spectra of $LaPO_4$:Ce^{3+}, Tb^{3+} produced by different synthesis methods.

Figure 5.4. shows the SEM images for $LaPO_4:Ce^{3+}$, Tb^{3+} particles prepared by the various methods. In Figure 5.4.(a) and (b), co-precipitation and hydrothermal powders, both forming precipitates under solution, are shown to have nearly spherical morphology, however being severely agglomerated. The average particle sizes from both hydrothermal and co-precipitation methods were ~0.3 µm. In Figure 5.4.(c), sol-gel particles show a nearly spherical morphology with less agglomeration compared to the particles by hydrothermal and co-precipitation methods. These sizes ranged between 1.4-2.3 µm. In Figure 5.4.(d), the combustion-synthesized particles are shown to have an irregular shape with a particle size in the range of 2.3-3.1 µm. As shown in Figure 5.4.(e), the particle size of spray-pyrolyzed powders averaged ~0.5 µm with a spherical morphology.

Different crystallite sizes and the morphologies can affect the luminescence properties of the phosphors due to different surface-volume ratio, which is critical component in the quantum efficiency of the phosphors [35]. Figure 5.5. shows the PL emission spectra of $Y_2O_3:Eu^{3+}$ powders prepared by the different synthesis methods excited at 253 nm. There are three groups of emission peaks between 580 and 626 nm, which are from the $^5D_o \rightarrow ^7F_J$ (J = 1, 2, 3) transitions of Eu^{3+}, respectively. The strongest emission peak at 611 nm corresponds to the forced electron dipole transition of Eu^{3+} from $^5D_o \rightarrow ^7F_2$ transition. The powders produced using the sol-gel method produced the highest emission intensity. This can be attributed to the larger crystallite size of the sol-gel powders relative to other methods. Sol-gel powders also had the largest particle size (~2.19 µm). Combustion synthesized powders had the second highest emission intensity, having a small crystallite size (18 nm) and a relatively large average particle size (1.64 µm). Co-precipitation powders produced the largest crystallite size (28.2 nm), but the smallest average particle size (~0.32 µm) with an intermediate PL emission intensity. Spray pyrolyzed powders had the smallest crystallite size (13.2 nm), a small average un-agglomerated particle size (~0.56 µm) and exhibited the lowest PL emission intensity. Hydrothermal powders showed a higher PL

emission intensity than spray pyrolysis powders with a larger crystallite size (23.7 nm) and an intermediate average particle size (~0.95 µm).

Figure 5.6. shows the PL emission spectra of $LaPO_4:Ce^{3+}$, Tb^{3+} powders prepared by various methods excited at 276 nm. The strong yellowish-green emission is related to the transitions between the excited $^5D_4$ state and the ^7F_J **(J = 0–6)** grounds states of Tb^{3+}, which is excited by the Ce^{3+} emission. The co-precipitated powders produced the highest intensity, which can be attributed to the relatively large crystallite size (32.8 nm), however the average particle size was relatively small (~0.33 µm). The second highest emission intensity occurred for hydrothermal synthesized powders with intermediate crystallite and particle sizes. The lowest emission intensity occurred for the spray pyrolyzed powders, despite having a slightly higher activator concentration. These powders had the smallest crystallite size (14.1 nm) and an intermediate particle size. Combustion and sol-gel synthesized powders have intermediate normalized intensities, with the largest crystallite and particle sizes.

Figure 5.7. show the influence of the crystallite size on the normalized PL emission intensity. The $Y_2O_3:Eu^{3+}$ powders were normalized to the sol-gel powder intensity (the highest) while the $LaPO_4:Ce^{3+}$, Tb^{3+} intensities were normalized to the co-precipitated powder intensity (the highest). From this plot, it can be concluded that increasing the crystallite size increases the emission intensity, in corroboration with Wang et al. [25]. In general, our combustion, co-precipitation and sol-gel synthesized powders tend to have high PL emission intensity. The spray pyrolyzed powders exhibit the lowest intensity, which is attributed to the small crystallite size. The dotted line on Figure 5.7. is a best-fit line between crystallite size and normalized intensity.

The PL intensity does not seem to be as dependent on particle size, compared to the strong relationship with crystallite size. Figure 5.8. is a plot of the normalized emission intensity as a function of particle size. Particle sizes ranging from sub-micron to 1 µm show normalized intensities ranging from 0.3 to 1. However, the larger particles (> 1 µm) show higher normalized

intensities for sol-gel and combustion synthesized powders. The dotted line shows a linear regression of the mean average sizes, demonstrating that is only a slight correlation. This is in contrast to reports that find a particle size dependence of emission intensity [24, 25].

For Y_2O_3:Eu^{3+}, sol-gel and combustion reacted powders emit the highest relative PL intensity while having the same spherical structure and agglomeration as those of relatively high intensity co-precipitation and hydrothermal. These results corroborate the findings of Wang et al. [36], who found the highest PL emission intensity for Y_2O_3:Eu^{3+} powders having a spherical morphology compared to rods or flakes.

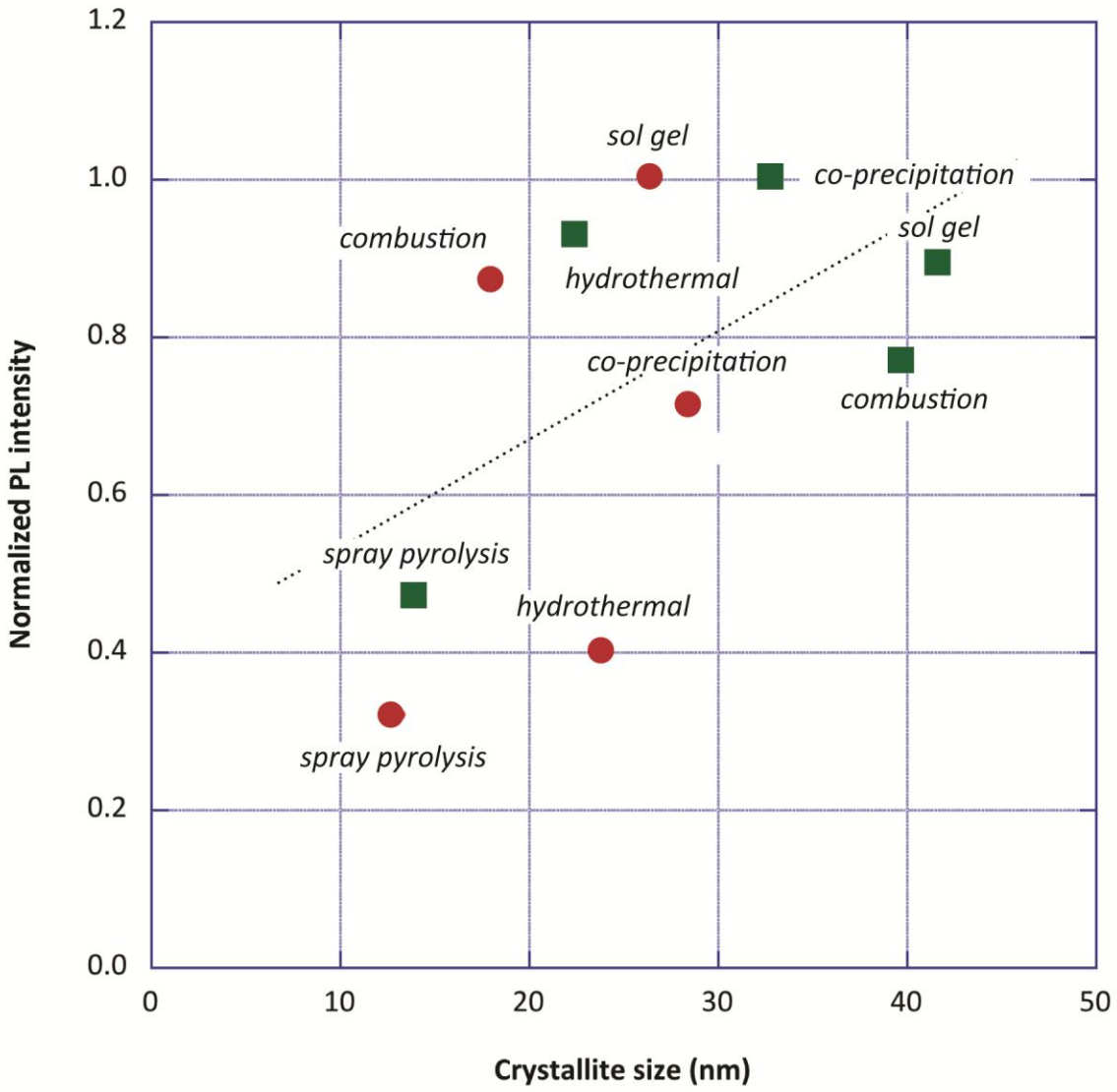

Figure 5.7. Normalized Y_2O_3:Eu^{3+} (red circles) and $LaPO_4$:Ce^{3+},Tb^{3+} (green squares) photoluminescence emission intensity as a function of crystallite size. Y_2O_3:Eu^{3+} is normalized to the sol gel intensity (highest) and $LaPO_4$:Ce^{3+}, Tb^{3+} is normalized to the co-precipitated intensity (highest).

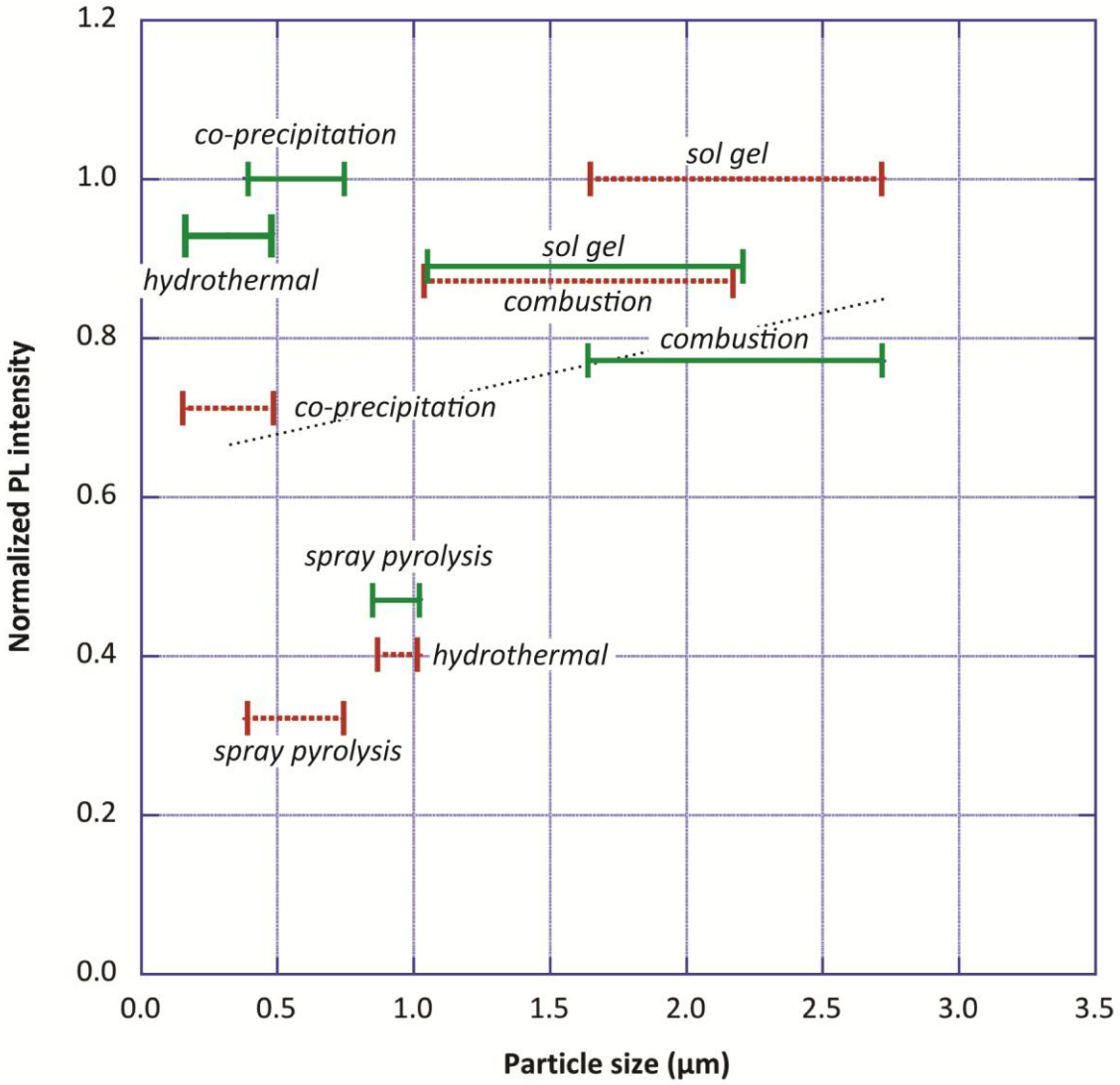

Figure 5.8. Normalized Y_2O_3:Eu^{3+} (red dashed) and $LaPO_4$:Ce^{3+}, Tb^{3+} (green solid) photoluminescence emission intensity as a function of particle size for different synthesis methods. Y_2O_3:Eu^{3+} is normalized to the sol gel intensity (highest) and $LaPO_4$:Ce^{3+}, Tb^{3+} is normalized to the co-precipitated intensity (highest).

5.5. Conclusions

This is the first study comparing the crystallite and particle sizes and morphology with the respective photoluminescence emission intensity of two phosphor compositions prepared by five methods. Y_2O_3:Eu^{3+} and $LaPO_4$:Ce^{3+}, Tb^{3+} powders were prepared by combustion reaction, co-precipitation, hydrothermal, sol-gel, and spray pyrolysis synthesis methods. For Y_2O_3:Eu^{3+}, the sol-gel method showed the highest PL emission intensity compared to other methods having a crystallite size of 26 nm and an average particle size of 2.19 µm. The spray-pyrolyzed powders have the lowest intensity with a 13 nm crystallite size and an average particle size of 0.56 µm. For $LaPO_4$:Ce^{3+}, Tb^{3+}, the co-precipitation method has the highest PL emission intensity with 33 nm crystallite size and an agglomerated morphology. The spray-pyrolysis method produces the lowest intensity with a crystallite size of 14 nm and a spherical and un-agglomerated morphology.

This study shows that a large crystallite size along with nearly-spherical and agglomerated particles tend to emit the highest PL intensity. The results show in general increasing intensity as a function of increasing crystallite size, with the exception of combustion-synthesized Y_2O_3:Eu^{3+} particles and co-precipitated $LaPO_4$:Ce^{3+},Tb^{3+} particles, which show high intensity with a relatively small crystallite size. The characteristic of producing high intensity with small crystallite size needs to be investigated further in detail. There was a slight increase in photoluminescence emission intensity with increase in particle size.

5.6. Acknowledgements

This work was supported by the U.S. Department of Energy Grant, DE-EE0002003**.** Chapter 5, in full, is a reprint of the material as it will appear in Materials Characterization, Seung-hyo Lee, Jae Ik Choi, Jinkyu Han, Youngjin Kim, Jan B. Talbot, and Joanna McKittrick. The dissertation author contributed the synthesis of the phosphors and characterization.

References

1. R.P. Rao, “Preparation and characterization of fine grain yttrium based phosphors by sol gel process,” J. Electrochem. Soc., 143, 189-197 (1996).

2. F.F. Kruis, H. Fissan, A. Peled "Synthesis of nanoparticles in the gas phase for electronic, optical, and magnetic applications - A review,” J. Aero. Sci., 29, 511-535 (1998).

3. R.N. Bhargava, "Doped nanocrystalline materials - Physics and applications,” J. Lumin. 70, 85-94 (1996).

4. C.R. Ronda, "Phosphors for lamps and displays: an applicational view," J. Alloy Comp., 225, 534-538 (1995).

5. C. He, Y. Guan, L. Yao, W. Cai, X. Li, Z. Yao, “Synthesis and photoluminescence of nano-Y_2O_3:Eu^{3+} phosphors,” Materials research bulletin, 38(6), 973-979 (2003).

6. C.R. Ronda, “Recent achievements in research on phosphors for lamps and displays,” J. Lumin. 72, 49-54 (1997).

7. G. Blasse, B.C. Grabmaier, Luminescent Materials, Springer-Verlag (1994).

8. H. Meyssamy, K. Riwotzki, A. Kornowski, S. Naused, M. Haase, "Wet-chemical synthesis of doped colloidal nanomaterials: particles and fibers of $LaPO_4$:Eu, $LaPO_4$:Ce, and $LaPO_4$:Ce, Tb," Adv. Mat., 11, 840-844 (1999).

9. K. Y. Jung, Y. C. Kang, Y. K. Park, "DMF effect on the morphology and the luminescence properties of Y_2O_3:Eu^{3+} red phosphor prepared by spray pyrolysis,” J. Ind. Eng. Chem.,14, 244-229 (2008).

10. I. Lenggoro, B. Xia, H. Mizushima, K. Okuyama, N. Kijima, "Synthesis of $LaPO_4$:Ce,Tb phosphor particles by spray pyrolysis,” Mat. Lett., 50, 92-96 (2001).

11. Q. Pang, J. Shi, Y. Liu, D. Xing, M. Gong, N. Su, "A novel approach for preparation of Y_2O_3:Eu^{3+} nanoparticles by microemulsion-microwave heating," Mat. Sci. Eng., 103, 57-61 (2003).

12. R. Chai, H. Lian, P. Yang, Y. Fan, Z. Hou, X. Kang, J. Lin, "In situ preparation and luminescent properties of $LaPO_4$:Ce^{3+}, Tb^{3+} nanoparticles and transparent $LaPO_4$:Ce^{3+}, Tb^{3+}/PMMA nanocomposite," J. Coll. Int. Science., 336, 46-50 (2009).

13. C. Waite, R. Mann, A. L. Diaz, "Measurement of host-to-activator transfer efficiency in nano-crystalline Y_2O_3:Eu^{3+} under VUV excitation," J. Sol. St. Chem., 198, 357-363 (2013).

14. N. Arul Dhas, K. Patil, "Synthesis of $AlPO_4$, $LaPO_4$, and $KTiOPO_4$ by flash combustion," J. All. Comp., 202 137-141 (1993).

15. J. Zhang, Z. Zhang, Z. Tang., Y. Lin, Z. Zheng., "Luminescent properties of Y_2O_3:Eu synthesized by sol-gel processing," J. Mater. Proc. Tech.,121, 265-268 (2002).

16. M. Yu, J. Lin, J. Fu, Y. Han, "Sol-gel fabrication, patterning and photoluminescent properties of $LaPO_4$:Ce^{3+},Tb^{3+} nanocrystalline thin films," Chem. Phys. Lett., 371, 178-183 (2003).

17. P. Tanner, L. Fu, "Morphology of Y_2O_3:Eu^{3+} prepared by hydrothermal synthesis," Chem. Phys. Lett., 470, 75-79 (2009).

18. H. Dong, Y. Liu, P. Yang, W. Wang, J. Lin, "Controlled synthesis and characterization of $LaPO_4$, $LaPO_4Ce^{3+}$ and $LaPO_4Ce^{3+}$, Tb^{3+} by EDTA assisted hydrothermal method," Sol. Stat. Sci., 9, 1652-1660 (2010).

19. C. Wang, Y. Li, W. Zhang, M. Yin, "Effect of acidity of microstructure and spectroscopic properties of Y_2O_3:Eu^{3+} powders and ceramics," Spect. Act., 75, 8-13 (2010).

20. N. Nunez, S. Liviano, M. Ocana, "Citrate mediated synthesis of uniform monazite $LnPO_4$ (Ln = La, Ce) and Ln:$LaPO_4$ (Ln = Eu, Ce, Ce+Tb) spheres and their photoluminescence," J. Coll. Int. Sci., 349, 484-491 (2010).

21. R. Yavetskiy, V. Baumer, M. Danylenko, A. Doroshenko, I. Ogorodnikov, I. Petrusha, A. Tolmachev, V. Turkevich, "Transformation-assisted consolidation of Y_2O_3:Eu^{3+} nanospheres as a concept to optical nanograined ceramics," Ceram. Int., 40, 3561-3569 (2013).

22. X. Hu, S. Yan, L. Ma, G. Wan, J. Hu, "Preparation of $LaPO_4$:Ce,Tb phosphor with different morphologies and their fluorescence properties," Pow. Tech, 192, 27-32 (2009).

23. J.K. Han, M.E. Hannah, A. Piquette, J. B. Talbot, K.C. Mishra and J. McKittrick, "Nano- and submicron sized europium activated silicate phosphors prepared by a modified co-precipitation method, " ECS J. Solid State Sci. Technol., 1, R98-R102 (2012).

24. K.Y. Jung, C.H. Lee, Y.C. Kang, "Effect of surface area and crystallite size on luminescent intensity of Y_2O_3:Eu^{3+} phosphor prepared by spray pyrolysis," Mater. Lett., 59, 2451-2456 (2005).

25. W. Wang, W. Widiyastuti, T. Ogi, I. Lenggoro, K. Okuyama, "Correlations between crystallite/particle size and photoluminescence properties of submicrometer phosphors," Chem. Mater., 19, 1723-1730 (2007).

26. K. Jung, D. Lee, Y. Kang, S. Park, "Size-dependent luminescent properties of hollow and dense $BaMgAl_{10}O_{17}$:Eu blue phosphor particles prepared by spray pyrolysis," Korean J. Chem. E., 21, 1072-1080 (2004).

27. N. Lakshminarasimhan, U. Varadaraju, "Role of crystallite size on the photoluminescence properties of $Srln_2O_4:Eu^{3+}$ phosphors synthesized by different methods," J. Solid State Chem., 181, 2418-2423 (2008).

28. L.S. Chi, R.S. Liu, B.J. Lee, "Synthesis of Y_2O_3:Eu, bi red phosphors by homogeneous coprecipitation and their photoluminescence behaviors, " J. Electrochem. Soc., 152, J93-J98 (2005).

29. T. Ye, S. Li, X. Wu, M. Xu, X. Wei, K. Wang, H. Bao, J. Wang and J. Chen, "Sol–gel preparation of efficient red phosphor $Mg_2TiO_4:Mn^{4+}$ and XAFS investigation on the substitution of Mn^{4+} for Ti^{4+}," J. Mater. Chem. C, **1**, 4327-4333 (2013).

30. Q. Wei and D. Chen, "Luminescent properties and the morphology of $SrMoO_4:Eu^{3+}$ powders synthesized via combining sol–gel and solid-state route," Cent. Eur. J. Phys., 8, 766-770 (2010).

31. H. He, R. Fu, H. Wang, X. Song, Z. Pan, X. Zhao, X. Zhang and Y. Cao, "$Li_2SrSiO_4:Eu^{2+}$ phosphor prepared by the Pechini method and its application in white light emitting diode," J. Mater. Res., 23, 3288-3294 (2008).

32. Y. Li, D. He, Y. Want, M. Fu, Y. Wu, F. Miao, "Luminescence properties of nano-crystalline $Ba_3MgSi_2O_8:Eu^{2+}$, Mn^{2+} phosphors," J. Nanosci. Nanotech., 11, 9829-9832 (2011).

33. L.E. Shea, J. McKittrick, O.A. Lopez, "Synthesis of red-emitting, small particle size luminescent oxides using an optimized combustion process," J. Am. Ceram. Soc., 79(12), 3257-3265 (1996).

34. H.N. Luitel, R. Chand, T. Torikai, M. Yada and T. Watari, "Rare earth free $Zn_3V_2O_8$ phosphor with controlled microstructure and its photocatalytic activity," Intl. J. Photoenergy, 2013, Article ID 410613 (2013).

35. J. McKittrick, M.E. Hannah, A. Piquette, J.K. Han, J.I. Choi, M. Anc, M. Galvez, H. Lugauer, J.B. Talbot, K.C. Mishra, "Phosphor selection considerations for near-UV LED solid state lighting," ECS J. Solid State Sci. Technol., 2, R3119-R3131 (2013).

36. L.S. Wang, Y.H. Zhou, Z.W. Quan, J. Lin, "Formation mechanisms and morphology dependent luminescence properties of Y_2O_3:Eu phosphors prepared by spray pyrolysis process," Mater. Lett., 59, 1130-1133 (2005).

Chapter 6. EPD of phosphors for display and solid state lighting technologies

6.1. Abstract

Electrophoretic deposition (EPD) has been used for phosphor screening for a variety of emissive information displays and more recently, for solid state lighting. EPD is well suited to deposit the fine (nanometer to micrometer diameter) phosphor particles needed for high resolution displays. The fundamentals of the EPD process in an isopropanol (IPA) bath have been characterized by the dissociation behavior of nitrate salts in IPA, measurement of the effects of pH and nitrate salt concentration on the zeta potential of the particles, studying of the processing conditions and modeling of the deposition rates. The electrochemical precipitation reactions form an adhesive agent for the particles and the adhesion strength can be enhanced by various methods to meet the requirements of these technologies.

6.2. Introduction

Phosphors are materials that emit visible light when excited by photons (photo-luminescence), electrons (cathodoluminescence), or electric fields (electroluminescence). Electrophoretic deposition (EPD) of powder phosphors, from nanometer to micron diameter size, has been used in the manufacturing of emissive displays, such as cathode ray tubes (CRTs), field emission displays (FEDs) and plasma display panels, and particularly for high-resolution screens [1]. The performance of emissive display screens depends upon the uniformity, density, and adhesion of the phosphor layer [2].

Light emitting diodes (LEDs) offer the promise of energy efficient, low cost white-emitting solid state lighting (SSL). One approach for generating white light combines UV or blue LEDs with phosphors that convert the LED emission to visible light. This results in a device that emits light with several wavelengths over the visible spectrum which is perceived as white light

by the human eye. Recently, EPD has been used to deposit phosphors onto LEDs and we are currently studying EPD for near-UV emitting phosphors for SSL applications.

6.3. Fundamentals of the Process

The fundamental steps of the EPD process are: 1) charging of the particles in suspension, 2) transport of particles under an electric field, and 3) adherence of the particles to the substrate. The steps were systematically studied in our work with phosphors by investigating the dissociation of nitrate salts in IPA [3], the effects of suspension medium chemistry on zeta potential of the particles [3, 4], and the effects of deposition conditions to model the process [5].

The dissociation of 10^{-7} to 10^{-2} M $Mg(NO_3)_2$ in IPA was studied by measuring molar conductivity [4]. Then, the mobility of the ions were determined using the limiting conductivity and the concentration of ions were calculated from the dissociation constant. In liquids of low dielectric constant such as IPA, dissociation is very small; the first and second dissociation constants were found to be 6×10^{-5} and 2×10^{-7} M, respectively. The limiting conductivities for $Mg(NO_3)^+$ and Mg^{2+} in IPA were determined to be 18 and 120 mho-cm^2/mole, respectively. In the concentration range of 10^{-4} to 10^{-3} M $Mg(NO_3)_2$ typically used in our EPD baths, $Mg(NO_3)^+$ is the predominant cation available to charge the particles.

The zeta potentials of several oxide, sulfide, and oxysulfide phosphors were measured in IPA and in IPA containing nitrate salts and water [3, 4]. The zeta potentials of phosphors in pure IPA were negative. With the addition of 5×10^{-4} M nitrate salt, the zeta potentials of nearly all the phosphors became positive. The effects of nitrate salt concentrations and pH on the zeta potentials of Zn_2SiO_4:Mn (P-1) and ZnS:Ag (P-11) phosphor particles, in particular, were studied [4]. The zeta potential was negative (~ –45 mV) at nitrate concentrations less than 10^{-7} M. As the salt concentration increased, the zeta potential increased and became positive, reaching a maximum (~50 mV) at 10^{-5} M. In IPA or IPA with 10^{-5} M $Mg(NO_3)_2$, the zeta potential was

positive at pH<6, but became negative for pH>6. At higher salt concentrations of 10^{-4} and 10^{-3} M, the zeta potential remained positive for all pH values. Therefore, the zeta potential is dependent upon both the nitrate salt concentration and pH.

During EPD, electrolysis of the water present in the IPA creates a basic environment at the cathode. Thus, $Mg(NO_3)^+$ reacts with the hydroxide ions to produce $Mg(OH)_2$ [4, 5]. By carefully controlling the amount of water in the IPA bath, it was determined that alkoxide, $Mg(C_3H_7O)_2$, formation can also occur [6]. When the water concentration in the EPD bath is low (<1 vol%), the alkoxide predominately forms, whereas at high water content (>5 vol%), the hydroxide forms. At intermediate water concentrations, a mixture of the two materials forms. Note, however, that hydrogen evolution can become a problem for EPD at the cathode with a high concentration of water in solution. The dissociation of nitrate salts and thus, conductivity of the solution also increases with increased amounts of water. Thus, the role of the $Mg(NO_3)_2$ in the EPD bath is to charge the particles positively, to maintain the positive zeta potential at a high pH at the cathode, and to form the adhesive material.

The amounts of deposited particles and magnesium hydroxide binder were simply modeled by integrating the flux of material over time [4, 6]. The deposition rates of both the phosphor and $Mg(OH)_2$ predicted from this simple model agreed with experimental results provided that the $Mg(NO_3)_2$ concentration was greater than ~10^{-4} M [5]. This minimum concentration maintains a positive zeta potential near the cathode and provides the necessary amount of binder to adhere the particles.

6.4. EPD for Information Displays

With a basic understanding of the EPD process for phosphors, our research focused on its application for emissive information displays. Phosphor screens must meet a number of requirements for use in an information display [2]. The deposit thickness must be optimized to

ensure pin-hole free coverage, yet not reduce light emission. The packing density should be optimized for the best light output. The screen must be uniform to ensure consistent optical performance. The amount of non-luminescent material needs to be minimized. Finally, the deposit must have sufficient adhesion strength to withstand handling during manufacturing, as well as during use. Sluzky and Hesse [7] studied the EPD of phosphor screens and concluded that the screen can demonstrate brightness equal to coatings made by standard settling methods and are capable of very high resolution.

To meet the requirements for display screens, we studied the adhesion of EPD phosphor particles and techniques to enhance the adhesion strength [6]. The single greatest effect on the adhesion strength was the added 2 vol.% glycerin to the deposition bath. Adhesion has been also significantly enhanced by spray coating a photoresist layer on top of the EPD phosphor film [8]. The optical performance of phosphor screens was found not to be affected by the process itself nor by the conditions that enhance phosphor adhesion under 1-4 kV excitation voltage applicable to FEDs [9]. Additionally, two new screening methods were developed, one for color displays by combining EPD and photolithography [10, 11]. Our phosphor screening process was developed to deposit triads of phosphor stripes onto an indium-tin-oxide (ITO)-covered glass substrate with a line resolution of 100 triads of 75 μm stripes per inch [11].

6.5. EPD for Solid State Lighting

White light has been obtained by mixing blue light from the emission of GaN and yellow light of a $Y_3Al_5O_{12}$:Ce (YAG:Ce) phosphor. A uniform coating and an optimized thickness of phosphor on a GaN chip are necessary for achieving an efficient white LED. Philips Limileds Lighting Company used EPD to produce a conformal phosphor coating on an LED for a uniform white light without colored rings [12].

Near UV-emitting (380-400 nm) InGaN-based diodes have comparable efficiency to blue-emitting InGaN diodes. However, they display less binning and are more efficient at higher current densities. In addition, there is the flexibility for color blending using red-, green- and blue-emitting phosphors. We are in the process of developing these phosphors for near-UV excitation. The final configuration of the light-emitting device will involve phosphors applied in a remote configuration mode with diffuse reflector-cup walls, as shown in Fig. 6.1. The LED chip in a SSL design strongly absorbs any UV light reflected back from the phosphor layer and any visible radiation emanating from the phosphor layer isotropically after down-conversion (Fig. 6.1.(a)). Thus, increasing the efficiency of light escape entails reducing back scattering of UV radiation and also reducing visible photons arriving at the chip. Both factors may be achieved by a remote phosphor configuration approach [13]. We will investigate two methods to couple the phosphor with the diode: EPD of powders onto the diode directly (Fig. 6.1.(b)) and EPD of the powders onto a transparent substrate for the remote phosphor configuration (Fig. 6.1.(c)).

Using the spectral power distribution of red, green and blue phosphors selected on the basis of fluorescence measurement, phosphor blends may achieve the desired color coordinates and color temperatures compatible with high efficacy. We have been using EPD to deposit mixtures of phosphors to obtain white light as shown in Fig. 6.2., which shows deposits of the individual phosphors (Fig. 6.2.(a)) and then a mixture of four phosphors (Fig. 6.2.(b)).

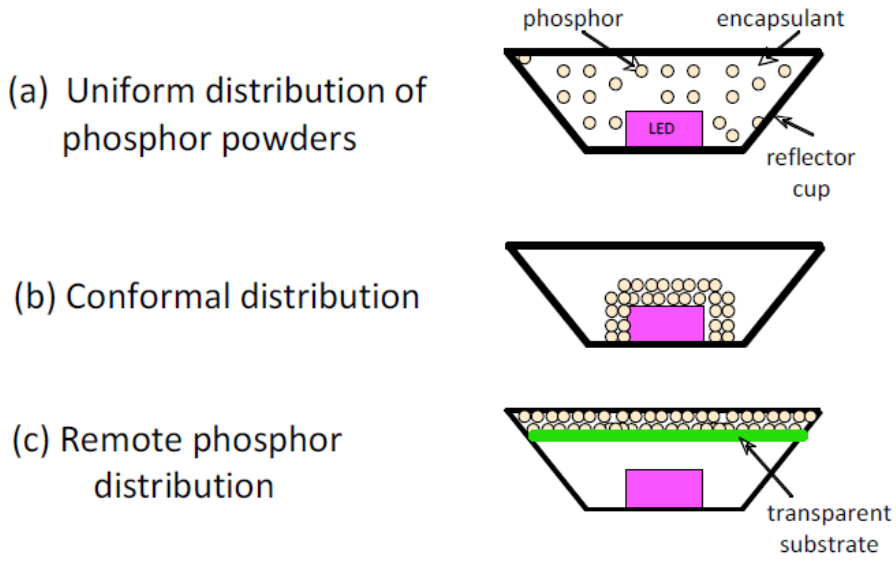

Figure 6.1. Schematic diagrams of phosphors in an encapsulant in white-emitting LEDs of (a) uniform distribution of phosphor powders dispersed above the LED, (b) conformal distribution and (c) remote phosphor distribution.

(b) $LiCaPO_4:Eu^{2+}$, $(Sr_{0.75}Ba_{0.25})_3SiO_5:Eu^{2+}$, $BaSiO_4:Eu^{2+}$ and $(SrCa)_2Si_5N_8:Eu^{2+}$ blends

Figure 6.2. Comparison of the deposits of (a) individual phosphors compositions and (b) mixture of four phosphor compositions under 365 nm excitation.

6.6. Summary

In order to electrophoretically deposit a wide variety of phosphors, the fundamentals of the process in an IPA bath were studied. By investigation of the dissociation behavior of nitrate salts in IPA, measurement of the effects of pH and nitrate salt concentration on the zeta potential of the particles, and by studying the EPD process conditions and modeling the deposition rates, the fundamentals of this EPD process have been well-characterized.

These fundamentals of the EPD process were applied to preparing screens for information displays and for solid state lighting. It was found that the color and brightness of screens made were unchanged by the processing conditions. EPD phosphor screens also only outgas H2, CO, CO2 and low level hydrocarbons under electron bombardment in FED tests [14], which make them attractive for use. Several methods that combine EPD and photolithography were developed to produce screens with a high resolution of triads of red-green-blue phosphor stripes to fabricate full-color screens. Even higher resolution could be achieved with a higher resolution mask and smaller sized phosphor particles.

A new application of EDP of phosphors is white solid state lighting which uses similar processing conditions as those for information displays. The ability to coat a uniformly thin, highly packed conformal or a remote layer phosphor layer on the LED has been the advantage of EPD for controlling color and efficiency.

6.7. Acknowledgements

The work on solid state lighting is funded by DOE Grant # DE-EE0002003. Chapter 6, in full, is a reprint of the material as it appears in Key Engineering Materials, Jae Ik Choi, Esther Sluzky, Maria Anc, Alan Piquette, Mark. E. Hannah, Kailash C. Mishra, Joanna McKittrick, and Jan B. Talbot, Vol. 507, pp. 149-153 (2012). The dissertation author contributed the experiment of electrophoretic deposition and figure formatting.

References

1. K.Y. Sasaki, J.B. Talbot, Adv. Mat., 11:2 (1999) 91.

2. L. Ozawa, Cathodoluminescence, Kodansha Ltd , Tokyo (1990).

3. M.J. Shane, J.B. Talbot, E. Sluzky, and K.R. Hesse, Colloids and Surfaces, 96 (1994) 301.

4. M.J. Shane, J.B. Talbot, R.D. Schreiber, C.L. Ross, E. Sluzky, and K. R. Hesse, J. Colloid Interface Sci., 165 (1994) 325.

5. M.J. Shane, J.B. Talbot, B.G. Kinney, E. Sluzky, and K.R. Hesse, J. Colloid Interface Sci., 165 (1994) 334.

6. B.E. Russ and J. B. Talbot, J. Electrochem. Soc., 145 (1998) 1245.

7. E. Sluzky and K. Hesse, J. Electrochem. Soc., 136 (1989) 2724.

8. J.H. Yum, K. Choi, Y.E. Sung, J. Electrochem. Soc., 150(2) (2003) H43.

9. S. Luo and J.B. Talbot, J. Electrochem. Soc., 148 (2001) H73.

10. D.C. Chang, J. B. Talbot, R.P. Rao, and C. Holland, J. Soc. Information Display, 8(1) (2000) 56.

11. J.B. Talbot, E. Sluzky, and S.K. Kurinec, J. Materials Science, 39(3) (2004) 771.

12. W.D. Collins III, M.R. Krames, G.J. Verhoeckx, N.J.M. van Leth (2003) US Patent 6,576,488.

13. N. Narendran, Y. Gu, J. P. Freyssinier-Nora and Y. Zhu, Phys. Stat. Sol. (A), 202 (2005) R60-R62.

14. M.E. Malinowski, K.D. Stewart, D.A.A. Ohlberg, T.E. Felter, A.G. Chakhovskoi, C. Hunt, L. Shea, B.E. Russ, J.B. Talbot, J. McKittrick, Proceedings of 8th Intern. Conf. on Vacuum Microelectronics, IVMC-95, Electron Device Society IEEE 202 (1995).

Chapter 7. Electrophoretic deposition of phosphors for white solid state lighting using near UV-emitting LEDs

7.1. Abstract

Electrophoretic deposition (EPD) is a method to deposit particles dispersed in a liquid onto a substrate under the force of an applied electric field, and has been applied for depositing phosphors for application in solid state lighting. The objective is to deposit phosphors in a "remote phosphor" configuration for a UV-LED-based light source for improved white light extraction efficiency. It is demonstrated that EPD can be used to deposit red-, green-, blue-, yellow- and orange-emitting phosphors to generate white light using a near UV-emitting LED by either depositing a phosphor blend or sequentially individual phosphor compositions.

7.2. Introduction

Electrophoretic deposition (EPD) is a method in which charged particles dispersed in a liquid are deposited onto a substrate using an applied electric field. The layer thickness is controlled by the applied voltage and the deposition time. As this process is simple, easy to use and often cost-effective, EPD of phosphor powders has been used in the manufacturing of emissive displays for some time [1, 2]. More recently, EPD was used to deposit $Y_3Al_5O_{12}:Ce^{3+}$ ($YAG:Ce^{3+}$) phosphors on a flexible indium tin oxide (ITO)-coated polyethylene terephthalate substrate on top of a blue-emitting light emitting diode (LED) to achieve white light [3]. EPD was used to deposit both layered and blended phosphor films, as shown in Fig. 7.1, using three types of SiAlON phosphors, Eu-activated Ca-α-SiAlON, β-SiAlON and $CaAlSiN_3$ (yellow-, green- and red-emitting, respectively) for color tuning with a blue-emitting LED [4]. The films were made from an ethanol bath with phosphate ester and polyethylenimine as dispersants and polyvinyl butyral as a binder. White light emission was observed from EPD films of blend of red-, yellow- and green-emitting phosphor, although the blend of yellow- and green-emitting phosphor with 6:4

ratio showed the best results. A higher proportion of the yellow phosphor was needed as the deposition rate of the yellow phosphor was less than for the green phosphor. When green and yellow phosphors were deposited sequentially as the first and the second layer (40 μm green + 15 μm yellow) with respect to the blue LED, the emission color was blue-white (5000 K). When the sequence was reversed (50 μm yellow + 50 μm green), a warm white (3000 K) was obtained. This was explained by stating the blue emission from the LED was mostly absorbed by the first layer regardless of the sequence of deposition.

EPD consists of three major processes: 1) charging the particles in suspension, 2) transport of the particles to an electrode under an electric field, and 3) adherence of the particles onto the substrate. Each process step was systematically investigated in previous work with EPD of phosphors in isopropyl alcohol (IPA) with nitrate salts [5], by studying the effects of the suspension medium chemistry on the zeta potential of the particles and the formation of adhesive agents [5-7] and by measuring the deposition rates of the phosphor [8]. Among the fundamentals of EPD process, the zeta potential is a key factor as it indicates the stability of the suspension and determines the direction and rate of migration of the particles during deposition. The role of nitrate salt in the bath is to charge the phosphor particle positively and to form a hydroxide binder, which acts as the adhesive material at the cathode.

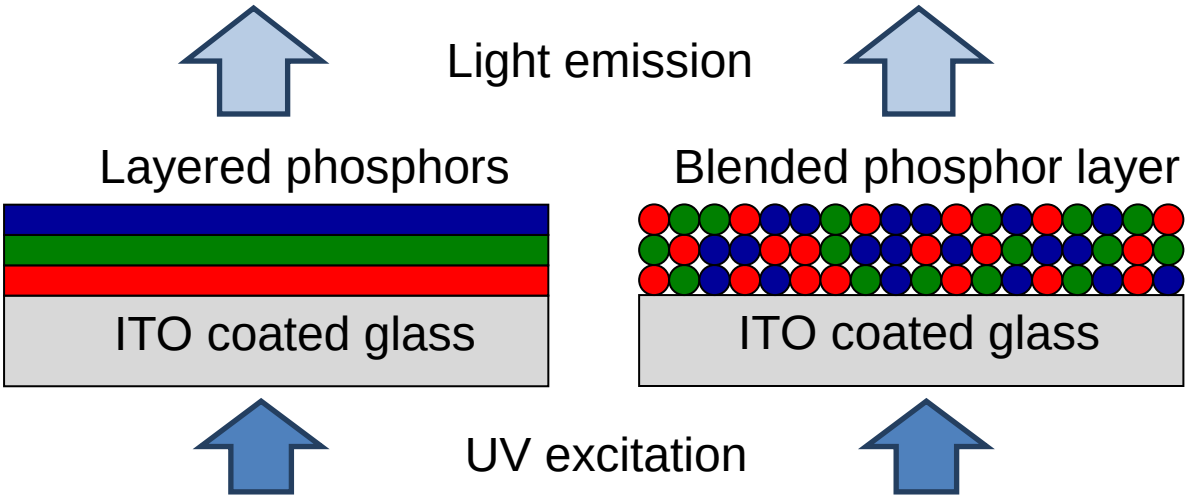

Figure 7.1. Schematic picture of electrophoretic deposition with sequentially deposited or blended phosphors (adapted from [5]).

For uniform deposition with a specified thickness, controlling the deposition process during EPD needs to be understood. Two basic but competing factors must be evaluated. Phosphors move horizontally when the electric field is applied, but they also move vertically due to the settling. The electrophoretic velocity is the product of the mobility (u) and the electric field strength (E) [9]:

$$v_{epd} = uE = (\xi\varepsilon/\mu)E \quad (1)$$

For the phosphor particles, the mobility is determined from the measured zeta potential (ξ) using the Smoluchowski equation, $u = \xi\varepsilon/\mu$, where ε is the permittivity and μ is the viscosity of solvent. The electrophoretic deposition rate, R, can be estimated using the Hamaker equation [10]:

$$R = \alpha C A v_{epd} \quad (2)$$

where C is the concentration of particles in solution, A is the area of the substrate and α is the fraction of particles adhered to the substrate (taken as 1). Thus, the rate is linearly proportional to the concentration of particles when other factors are same. On the other hand, large size phosphor powders tend to settle before smaller ones. The settling velocity, v_s, for spherical particles as given by the Stokes' law, is:

$$v_s = \frac{2}{9}\frac{(\rho_p - \rho_f)}{\mu} g r^2 \quad (3)$$

where ρ_p is the density of the particle, ρ_f is the density of fluid, g is the gravitational acceleration, and r is the radius of spherical particles. Two competing velocities, v_{epd} and v_s, play a major role in manipulating the real deposition rate during deposition.

Commercially available white-emitting LEDs are achieved with a combination of a blue-emitting InGaN LED and a yellow-emitting phosphor, YAG:Ce^{3+} [11]. Currently, a small amount of red-emitting phosphor is added for color correction. The physical location of phosphors plays an important role in the efficiency of white-emitting LEDs [12, 13]. Fig. 7.2(a) shows a schematic

diagram of the conventional white-emitting LED configuration, phosphor-in-cup. The phosphor is dispersed within an epoxy dome that surrounds the LED. Another conformal distribution is schematically shown in Fig. 7.2(b). EPD has been used to deposit YAG:Ce^{3+} phosphor conformally onto an InGaN LED [14]. Lastly, a remote phosphor configuration has been proposed [15], as shown in Figure 7.2.(c). The phosphor is located on the transparent substrate where is far away from the LED chip. The phosphor-in-cup (Fig. 7.2(a)) and conformal distribution (Fig. 7.2(b)) limit the efficiency due to the reabsorption of wavelength-converted light by the LED chip. This issue is critical in the conformal configuration due to the close proximity of the phosphor to the LED chip. The remote configuration (Fig. 7.2(c)) can reduce the reabsorption of backscattered and emitted visible radiation from both the LED and the phosphor. Also, thermal stability of the phosphor is expected to be improved since it is placed away from the LED chip.

White-emitting LEDs are evaluated by their correlated color temperature (CCT) and color rendering index (CRI). These are two major factors affecting the color quality of solid state lighting. Besides improving the phosphor configuration, white light produced from LEDs can be tuned from warm to cold (2,500 K to 6,500 K) depending on the composition of the phosphor blend. CCT is given in absolute temperature (K) and refers to the location of the light on the black body curve. The CRI represents the ability of a light source to reproduce colors of an object and is given on a scale of 0 to 100, the extent to which a series of standardized color samples differ in appearance when illuminated under a given light source, compared to a reference light source of a similar color temperature. The average shift in these color samples is expressed as CRI. The ratio of each phosphor in a blend needed to be in the white region near the black body locus on the CIE (Commission Internationale de l'Eclairage) chromaticity diagram, which can be estimated by use of their photoluminescence (PL) spectra.

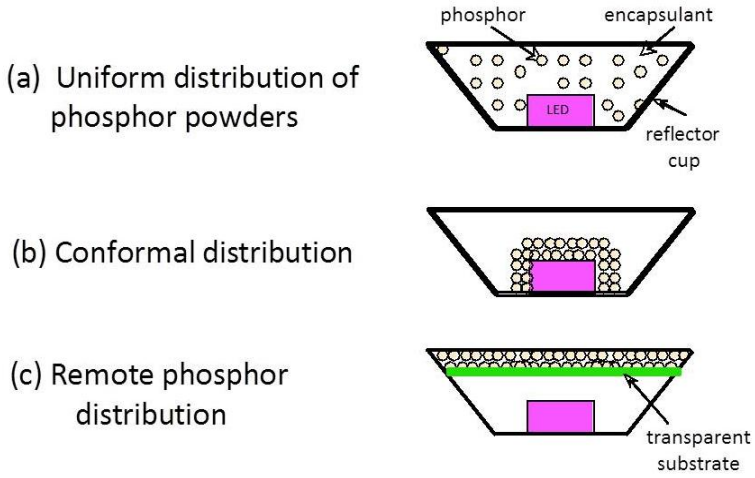

Figure 7.2. Schematic diagrams of phosphors in white-emitting LEDs: (a) uniform distribution of phosphor powders, (b) conformal distribution and (c) remote phosphor distribution.

In this work, EPD of various UV-excited phosphors and their blends was investigated with the ultimate goal of achieving white-light emission in a remote phosphor configuration. Both sequentially-deposited and blended phosphor films were fabricated.

7.3. Experimental

The phosphor powders used in this study were Eu^{2+}-activated $Sr_{2-x}Ca_xSi_5N_8$, Ba_2SiO_4, $LiCaPO_4$, $(Sr_{0.75}Ba_{0.25})_2SiO_4$ and $(Sr_{0.5}Ba_{0.5})_3SiO_5$, synthesized by solid state reaction, that emit red, green, blue, yellow and orange light, respectively, under 380 nm excitation. Individual phosphor compositions, average particle size, theoretical density and peak emission wavelength are shown in Table 7.1. EPD was carried out in a bath consisting of the phosphor powders, $Mg(NO_3)_2{\cdot}6H_2O$, isopropyl alcohol (IPA) and glycerin. The $Mg(NO_3)_2{\cdot}6H_2O$ concentration ranged from approximately 10^{-5} to 10^{-3} M, as determined by our previous work [5]. To enhance the dispersion of particles and adhesion strength, 2 vol.% glycerin was added to the bath. The zeta potentials of the powders were measured in a diluted suspension with various magnesium nitrate concentrations in IPA and 2 vol.% glycerin with a Zeta Plus meter (Brookhaven Instruments Corporation, Holtsville, NY).

An ITO-coated glass slide (2.5 cm × 5.1 cm × 1.1 mm, 70 ohms/sq., Bayview Optics, Dover-Foxcroft, ME) was used as the cathode, and an aluminum sheet was used as the anode. The deposition area was 2.5 cm × 2.5 cm. The electrodes were placed vertically and parallel to each other in a suspension with 1 cm separation as shown in Fig. 7.3. A voltage of 50-100 V was applied by a power supply for 1 min - 8 min to give a deposit thickness ranging from ~ 10 μm - 25 μm. The maximum applied voltage was 100V because the deposited film quality was poor when a higher applied voltage was used [16]. After the deposition process, the deposited samples were removed from the bath and dried in air.

Table 7.1. Individual phosphor compositions used for electrophoretic deposition.

Composition	Emission color	Average particle size	Density (g/cm^3)	Peak emission wavelength
$LiCaPO_4:Eu^{2+}$	Blue	10 ± 4	2.9	471
$(Sr_{0.25}Ba_{0.75})_2SiO_4:Eu^{2+}$	Green	5 ± 3	5.5	521
$(Sr_{0.75}Ba_{0.25})_2SiO_4:Eu^{2+}$	Yellow	8 ± 4	4.7	559
$(Sr_{0.5}Ba_{0.5})_3SiO_5:Eu^{2+}$	Orange	12 ± 5	5.2	607
$Sr_{2-x}Ca_xSi_5N_8:Eu^{2+}$	Red	7 ± 3	3.9	652

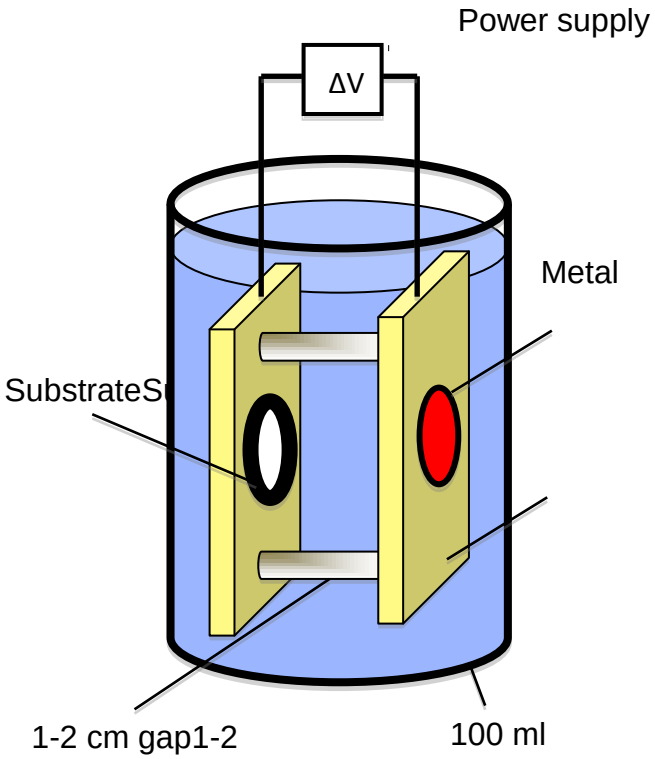

Figure 7.3. Schematic diagram of the electrophoretic bath set-up.

For deposition of each phosphor composition, a 5 g/L of powder was dispersed in 100 ml of IPA with $Mg(NO_3)_2 \cdot 6H_2O$ and glycerin. The nitrate concentration was chosen to obtain a zeta potential of ~30 mV - 40 mV for each phosphor. The zeta potential was negative at a low salt concentration. As the salt concentration increased to around 10^{-4} M, the zeta potential became positive. Magnesium nitrate concentrations and zeta potential values for each phosphor are shown in Table 7.2. In the case of the phosphor blends, a 5 g/L of a mixture of phosphor powders was ground lightly by a mortar and pestle and then dispersed in 100 ml of IPA. Sonication of the suspension for 1 hr was used to improve the dispersion of the powders in the suspension and assure the complete dissolution of $Mg(NO_3)_2 \cdot 6H_2O$.

The blend compositions were chosen to generate white light. At first, the phosphor blend was determined by a software simulation for an initial ratio. This blend was formulated and the resulting emission spectra of the blend by excitation from a UV LED and CIE coordinates were used to modify the blend until the formulation met the desired CCT, CRI and distance from the black body locus. Two different blends were chosen. One was a blend of three phosphor composition (blue-, yellow- and orange-emitting) and another one was a blend of four phosphors (blue-, green-, orange- and red-emitting). However, the real compositions of the blends were determined by experiments due to different deposition rates of phosphor components.

Blended phosphor films were prepared from a single deposition (5 min) using a bath with a mixture of phosphors. The three phosphor blend contained (by weight) 63 % blue-, 15 % yellow- and 22 % orange-emitting powders and the four phosphor blend contained 70 % blue-, 13 % green-, 5 % orange- and 12 % red-emitting powders.

Table 7.2. Magnesium nitrate concentrations and zeta potential values for each phosphor.

Phosphor composition	**$Mg(NO_3)_2$ concentration (M)**	**Zeta Potential (mV)**
$LiCaPO_4:Eu^{2+}$	1.2×10^{-5}	36 ± 3
$(Sr_{0.25}Ba_{0.75})_2SiO_4:Eu^{2+}$	1.0×10^{-5}	37 ± 3
$(Sr_{0.75}Ba_{0.25})_2SiO_4:Eu^{2+}$	1.0×10^{-5}	33 ± 3
$(Sr_{0.5}Ba_{0.5})_3SiO_5:Eu^{2+}$	1.2×10^{-5}	36 ± 4
$Sr_{2-x}Ca_xSi_5N_8:Eu^{2+}$	1.0×10^{-5}	36 ± 2

The other approach used was sequential deposition using different individual phosphor suspensions. The light emission of the sequentially-deposited films was changed by altering the thickness and the order of the sequentially-deposited phosphors. Two sequential depositions were performed using a bath of a mixture of red- and orange-emitting phosphors and a separate bath of green- and blue-emitting phosphors. First, red/orange (1:1 weight ratio) was deposited and then green/blue (2:3 weight ratio) was deposited. The deposition time in the first bath was for 1-3 min and the time in second bath was increased to 5-8 min to overcome the decrease of electric field on the electrode due to the resistance of the first layer.

The deposits were analyzed in terms of their thickness, PL spectra, CCT and CRI. The PL emission spectra were taken using a Jobin Yvon Triax 180 monochromator, SpectrumOne charge-coupled device (CCD) detection system and a 380 nm UV as the excitation source. The CCT and CRI were calculated from the measured PL spectrum of the phosphors using ColorCalculator software developed by OSRAM SYLVANIA Inc. (downloaded from https://www.sylvania.com). The thicknesses of the films and average particle sizes were estimated from micrographs taken by a field emission scanning electron microscope (FEI-XL30, FEI Company, Hillsboro, OR).

7.4. Results and discussion

For the EPD of individual phosphors, the deposit weight as a function of time is shown in Fig. 7.4.(a) and was converted to thickness as a function of time using the theoretical density of the composition and assuming a packing density of 56 % [17] in Fig. 7.4.(b). The deposition rate was ~1 μm/min for green-, yellow-, and orange-emitting phosphors and ~5 μm/min for red-emitting phosphor, estimated from the thickness of the films in Fig. 7.4. To minimize the settling of ~5-10 μm phosphor particles, the deposition time was limited to 8 min. After 8 min, stratification of the particles in the bath was clearly observed. The settling velocities estimated

from the Stokes' law in Eq. (3) ranged from 1×10^{-4} m/s - 7×10^{-4} m/s. Using the electrophoretic velocities of 1×10^{-5} m/s - 3×10^{-5} m/s estimated from Eq. (1), the deposition rates agree well with those calculated from Eq. (2), except for the nitride phosphor [9]. The nitride (red) phosphor film was thicker compared to the silicate or phosphate phosphor films. It was observed that this phosphor remained in suspension longer compared to the other phosphors thereby increasing the concentration or particles in solution during the deposition. In accordance with Eq. (2), this resulted in a thicker deposit for the same deposition time, but the reason of different state of suspension with the nitride phosphor is not understood. Fig. 7.5. shows photographs of deposits of the individual phosphor films excited by 365 nm showing the individual colors and demonstrating that a uniform coverage was achieved. The microstructure of the surface of each individual film is shown in Fig. 7.6, which also shows the range of particle sizes of the phosphor.

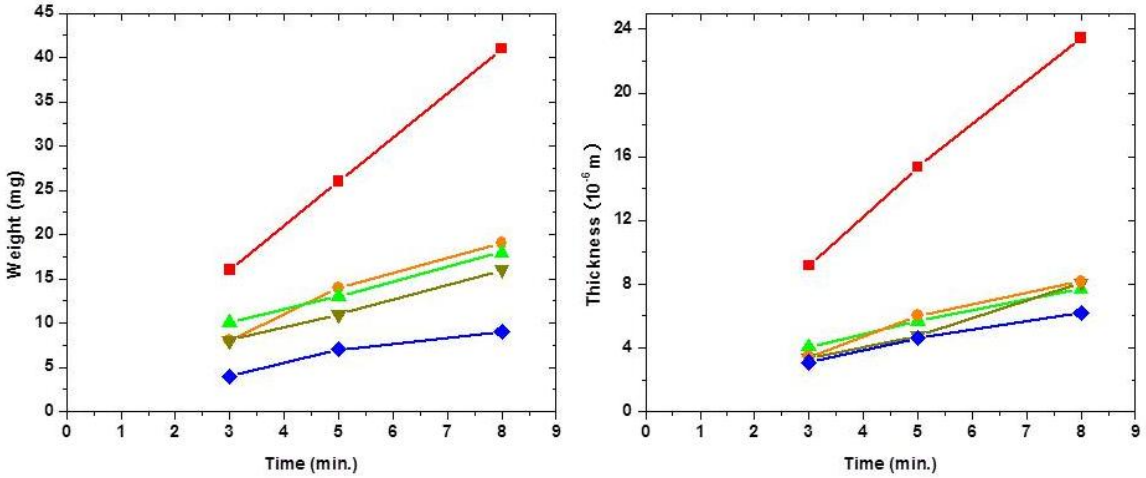

(a) (b)

Figure 7.4. (a) Deposit weight (per 6.45 cm^2) and (b) thickness of individual phosphors as a function of time. Eu^{2+}-activated $Sr_{2-x}Ca_xSi_5N_8$ (red – squares), Ba_2SiO_4 (green – triangles), $LiCaPO_4$ (blue – diamonds), $(Sr_{0.75}Ba_{0.25})_2SiO_4$ (dark yellow – inverted triangles) and $(Sr_{0.5}Ba_{0.5})_3SiO_5$ (orange – circles).

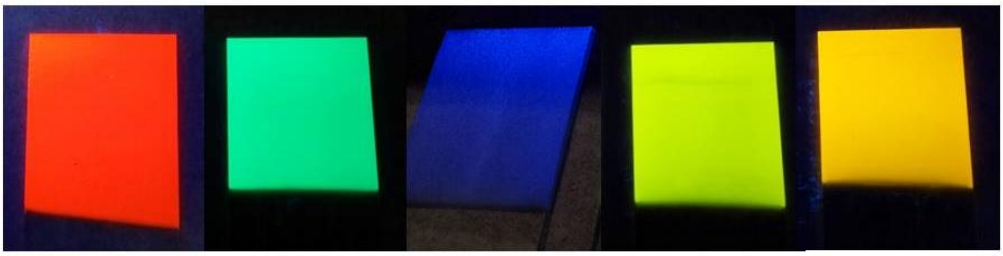

(a) (b) (c) (d) (e)

Figure 7.5. Photographs of individual phosphor deposits (2.5 × 2.5 cm^2 ITO coated substrates) excited by 365 nm, Eu^{2+}-activated (a) $Sr_{2-x}Ca_xSi_5N_8$, (b) Ba_2SiO_4, (c) $LiCaPO_4$, (d) $(Sr_{0.75}Ba_{0.25})_2SiO_4$ and (e) $(Sr_{0.5}Ba_{0.5})_3SiO_5$.

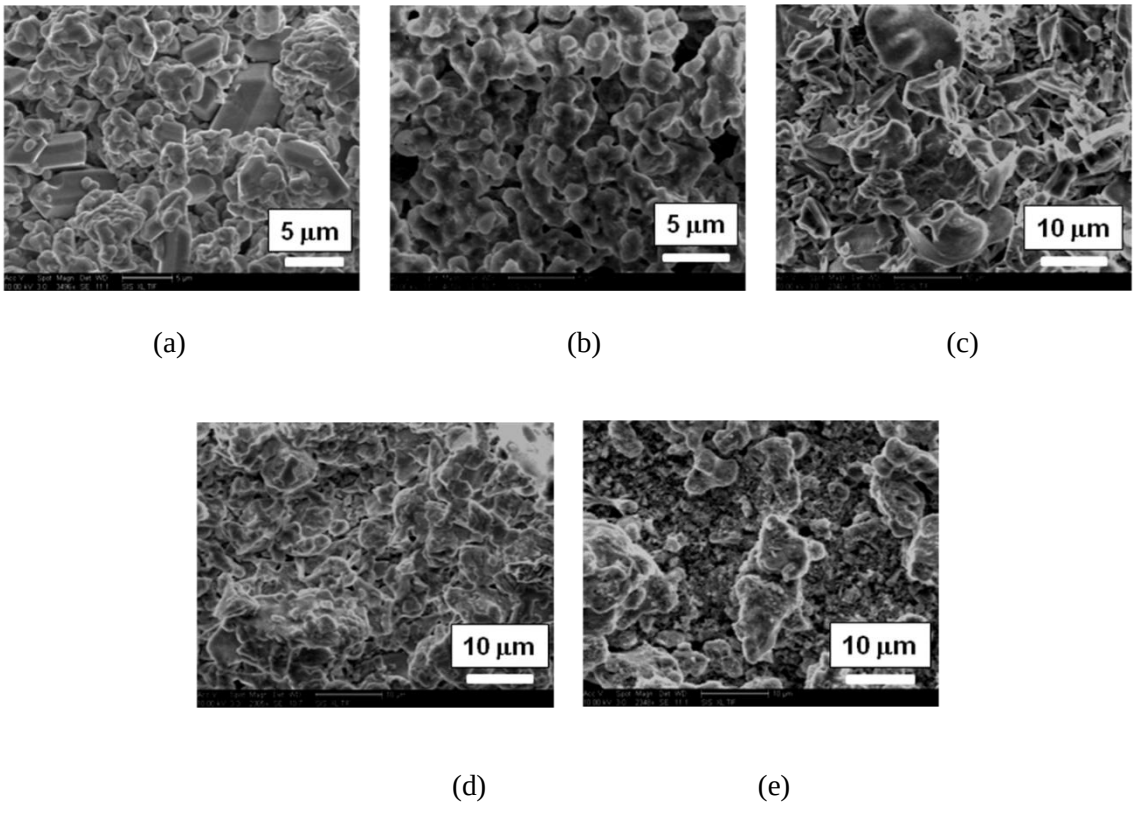

Figure 7.6. SEM micrographs of individual phosphor film surfaces, Eu^{2+}-activated (a) $Sr_{2-x}Ca_xSi_5N_8$, (b) Ba_2SiO_4, (c) $LiCaPO_4$, (d) $(Sr_{0.75}Ba_{0.25})_2SiO_4$ and (e) $(Sr_{0.5}Ba_{0.5})_3SiO_5$.

EPD was used to deposit phosphor layers either as a full blend or as a sequential deposition, as shown schematically in Fig. 7.1. with the goal of obtaining white light with a CCT of ~3000K and a high CRI (>80). Generally, the deposition rate is linear initially, as shown in Fig. 7.4.(a), but as deposition time increased over 8 min, the rate decreased due to the settling of the particles and the decrease of the electric field on the electrode due to the resistance of the film. Specifically, this effect is severe during the deposition of the second layer, since the first layer reduces the electric field strength [18]. Therefore, the range of deposition time was kept between 1 min to 8 min. Cross-sectional SEMs in Fig. 7.7. show the thicknesses (~20 μm) of (a) a four phosphor blend (5 min deposition) and (b) a layered film (the bottom layer is red/orange and the top layer is green/blue).

Fig. 7.8. shows the emission results on a CIE chromaticity diagram calculated from PL spectra of a film deposited with two different phosphor blends. The deposition rate of ~3-4 μm/min, estimated from the thickness of cross-sectional SEM micrographs of the films, was higher than that of the green-, yellow-, and orange-emitting phosphors (~1 μm/min) and lower than the red-emitting phosphor (~5 μm/min). Unlike the deposition of a single phosphor, the deposition of three or four phosphors from the same suspension is somewhat complicated. It was difficult to meet the desired color coordinates with the simulated formulation due to different deposition rates of individual phosphors. Also, it was observed that the phosphor blend remained in suspension longer than the green-, yellow-, and orange-emitting phosphors, which may then yield a thicker deposition for the same time, in accordance with Eq. (2). Fig. 7.8.(a) shows the results of a three phosphor blend (blue-, yellow- and orange-emitting) with a CCT of 3202 K and CRI of 75. Fig. 7.8.(b) shows the results of a four phosphor blend (blue-, green-, orange- and red-emitting) with a CCT of 3346 K and CRI of 94. The insets show photographs of the generated white light emitted by 365 nm excitation. Both white-emissions are well-situated near the black

body locus in the chromaticity diagram. A higher CRI was attained by blending four phosphors as expected, because of the addition of a red-emitting phosphor.

However, reabsorption of emission colors occurs among the phosphors [4, 19]. It has been shown that the luminous efficiency is improved by 8% by having a separate green-emitting layer on top of a red-emitting layer on a blue LED chip, due to a decrease of reabsorption of green light by the red-emitting phosphor [20]. In other work [21], it was found that a separate yellow-emitting phosphor on top of a red-emitting layer, with respect to the blue LED, led to an 18% increase in luminous flux compared to the blended yellow and red phosphor film. The enhanced efficiency was attributed to the reduced reabsorption of yellow light by the red-emitting phosphor [21]. Therefore, layered films were investigated and compared to the blended films to evaluate this concept.

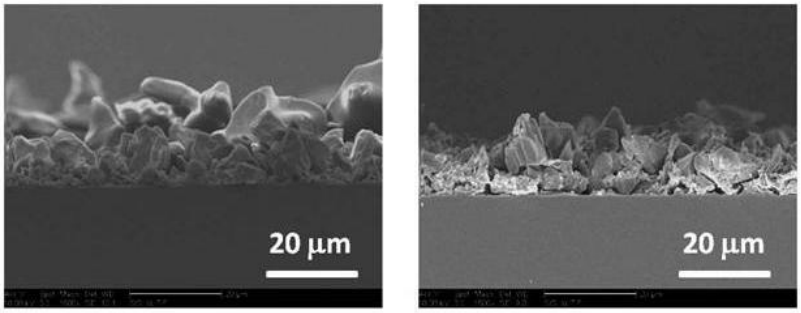

(a) (b)

Figure 7.7. Cross-sectional SEM micrographs of (a) four phosphor blend (5 min deposition) and (b) layered film (the bottom layer is red/orange and the top layer is green/blue).

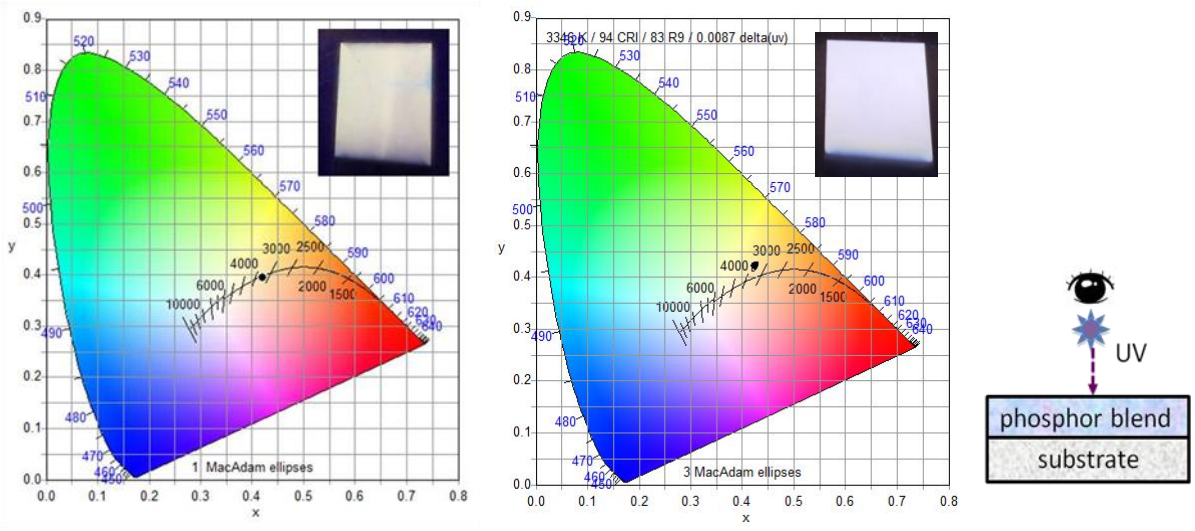

(a) (b) (c)

Figure 7.8. CIE coordinates and photographs of electrophoretically deposited phosphor blend films (λ_{ex} = 380 nm). (a) Three phosphor blend: mixture contains blue, 63 wt.%, yellow, 15 wt.% and orange, 22 wt.%. CCT = 3202 K, CRI = 75. (b) Four phosphor blend: mixture contains blue, 70 wt.%, green, 13 wt.%, orange, 5 wt.% and red, 12 wt.%. CCT = 3346 K, CRI = 94. (c) The insets show photographs of the generated white light emitted by λ_{ex}=365 nm.

Fig. 7.9.(a) shows the results of a red/orange mixture (1 min deposition time) as the first layer and a green/blue mixture (8 min deposition time) as the second layer made by sequential deposition on a CIE chromaticity diagram with a CCT of 3156 K and CRI of 90. The layered film was flipped over and illuminated, which showed approximately the same luminescence characteristics (Fig. 7.9.(b): CCT of 3159 K and CRI of 90). A film with the opposite order, green/blue as the first layer (3 min) and a red/orange as the second layer (5 min), was also fabricated by sequential deposition. The deposition times were modified in order to more closely match the ratio of the four phosphors blend described previously. The CIE chromaticity diagram in Fig. 7.10.(a) shows a CCT of 2721 K and CRI of 90. The layered film was flipped over and illuminated and was found to have the same luminescence characteristics (Fig. 7.10.(b): CCT of 2719 K and CRI of 90). Thus, two different orders of sequential deposition generated white light. Direct comparison between the layered films with the different deposition order was difficult because the thicknesses of the first and second layers of each film was different and were changed to meet the color coordinates on the black body locus.

Because the efficiency was improved by placing the red-emitting layer first with respect to the blue LED chip [20, 21], it was thought that the layering order in Fig. 7.9.(a) and Fig. 7.10.(b) with the green/blue layer farther away from UV light source may be better configuration for sequential deposition in terms of efficiency. However, the layered films showed approximately the same chromaticity coordinates, CRI and CCT when the film was flipped over and illuminated in this orientation, indicating no change in the ratio of the reabsorption occurred regardless of the order of the layers. Nevertheless, it should be noted that CRI and CCT could remain the same even when the lumen output or the photon flux changes, indicating there may be a difference in efficiency.

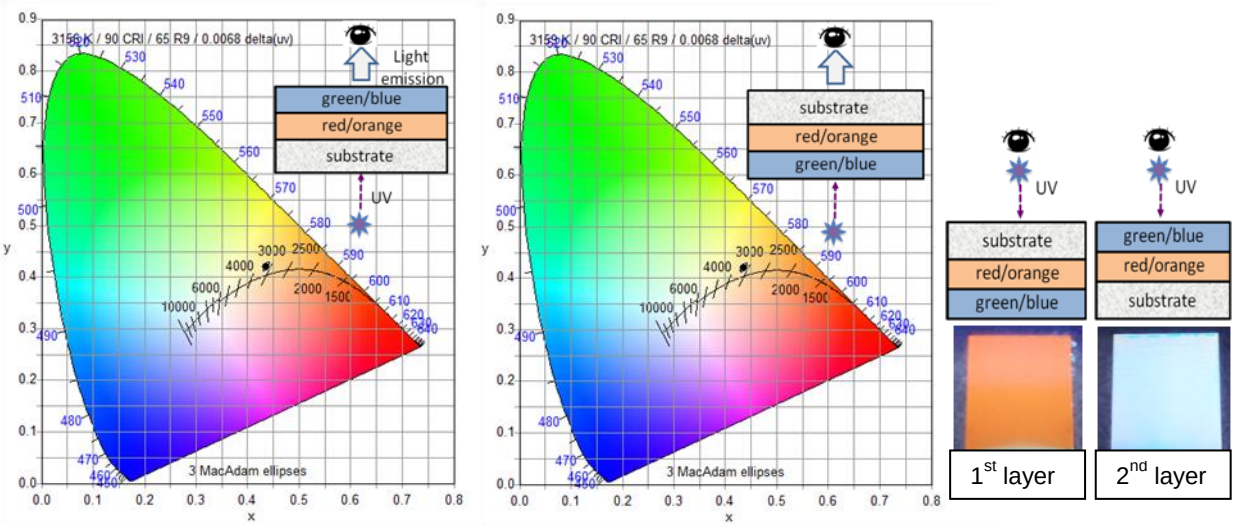

(a) (b) (c)

Figure 7.9. Four phosphor blend deposited by sequential electrophoretic deposition. First layer contains red/orange (1:1 wt. ratio), second layer contain green/blue (2:3 wt. ratio). (a) CCT = 3156 K, CRI = 90. (b) CCT = 3159 K, CRI = 90 (λ_{ex} = 380 nm). (c) 1st layer photograph (looking through the substrate) and 2nd layer photograph (looking on top of the phosphor) at λ_{ex} = 365 nm.

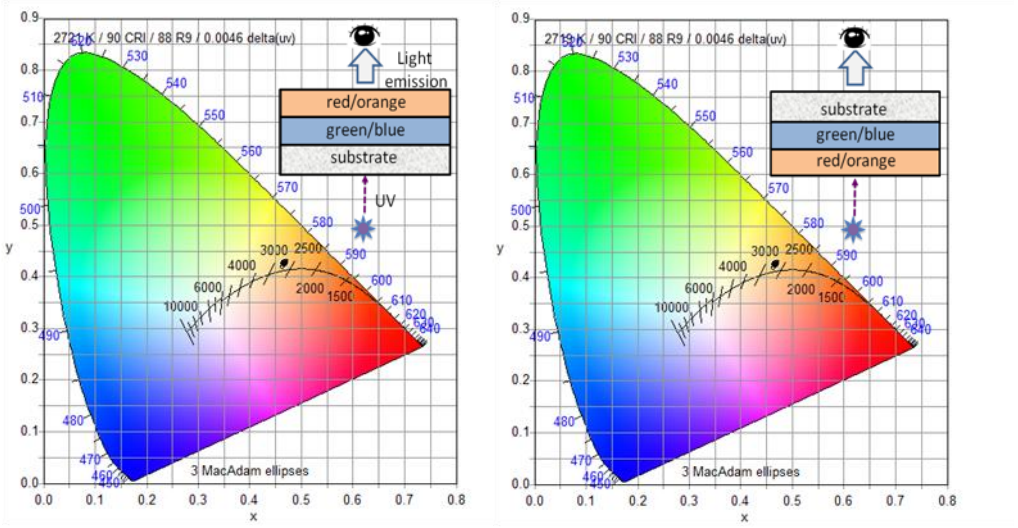

(a) (b)

Figure 7.10. Four phosphor blend deposited by sequential electrophoretic deposition. First layer contains green/blue (2:3 wt. ratio), second layer contain red/orange (1:1 wt. ratio). (a) CCT = 2721 K, CRI = 90. (b) CCT = 2719 K, CRI = 90 (λ_{ex} = 380 nm).

In other work on EPD for both blended and layered phosphor films [4], it was found that the deposition rates were higher (~55-160 μm/min) than the rates found in this work (~1-5 μm/min). This could be due to the higher concentration of particles (10 g/L) and higher zeta potential of the phosphor particles in an ethanol bath. In [4], both three-phosphor blends (red-, green- and yellow-emitting) and two-phosphor blends (green- and yellow-emitting) produced white light, which is the same result as in this work. The sequential deposition of the green and yellow phosphors showed different color temperatures according to the order of deposition. However, the first layer thickness (40 – 50 μm) was very thick, which prevented excitation of the second layer by the light from the LED. In the present work, the first layer thickness (5 – 15 μm) was thin enough so that the second layer was excited by the light from the LED. Thus, it is extremely important to deposit the appropriate thickness of each layer, when the sequential deposition method is employed so that the layers are efficiently excited by the light from the LED.

7.5. Conclusions

Individual and phosphor blend coatings were prepared by electrophoretic deposition (EPD) of red-, green-, blue-, yellow- and orange-emitting phosphors. The phosphor coverage was excellent, demonstrating that EPD is a viable method to produce phosphor layers for the "remote phosphor" white light design. The deposition rates were the same for the silicate and phosphate phosphor films but highest for the nitride phosphor film. The blend depositions, composed of both three and four phosphor compositions, emit white light located on or near the black body line on the CIE chromaticity diagram. Phosphor films were also prepared by sequential deposition of red/orange and green/blue compositions to generate white light. The layered films were flipped over and illuminated in this orientation, which showed approximately the same luminescence characteristics. No change in the ratio of the reabsorption of green/blue emission by the

red/orange phosphor was found regardless of the deposited order of the layered films. The blend deposition is better method due to easier emission color tuning. The applications of EPD of phosphors for white solid state lighting is a promising and effective method due to easy tuning of emissive color by varying the phosphor blend compositions.

7.6. Acknowledgments

This work is funded by DOE Grant # DE-EE0002003. Chapter 7, in full, is a reprint of the material as it appears in the Electrochemical Society Journal of Solid State Science and Technology, Jae Ik Choi, Maria Anc, Alan Piquette, Mark. E. Hannah, Kailash C. Mishra, Joanna McKittrick, and Jan B. Talbot, Vol. 2(7), pp. R153-R159 (2013). The dissertation author was the primary author of this paper.

References

1. K. Y. Sasaki and J. B. Talbot, *Adv. Mat*., **11**:2, 91 (1999).

2. Y. W. Jin, J. E. Jang, W. K. Yi, J. E. Jung, N. S. Lee and J. M. Kim, *J. Vac. Sci. Technol. B*, **17**(2) (1999).

3. J. Yum, S. Kim and Y. Sung, *Colloids and Surfaces A: Physicochem. Eng. Aspects*, **251**, 203-207 (2004).

4. T. Kitabatake, T. Uchikoshi, F. Munakata, Y. Sakka and N. Hirosaki, *Journal of the Ceramic Society of Japan*, **118**, 1 (2010).

5. M. J. Shane, J. B. Talbot, E. Sluzky, and K. R. Hesse, *Colloids and Surfaces*, **96**, 301 (1994)

6. M. J. Shane, J. B. Talbot, R. D. Schreiber, C. L. Ross, E. Sluzky, and K. R. Hesse, *J. Colloid Interface Sci*., **165**, 325 (1994).

7. B. E. Russ and J. B. Talbot, *J. Electrochem. Soc*. **145**(4), 1245 (1998).

8. M. J. Shane, J. B. Talbot, B. G. Kinney, E. Sluzky, and K. R. Hesse, *J. Colloid Interface Sci.*, **165**, 334 (1994).

9. J. B. Talbot, E. Sluzky and S. K. Kurinec, *J. Materials Science*, **39**, 771-778 (2004).

10. H. C. Hamaker, *Trans. Farad. Soc.*, **36**, 279-83 (1940).

11. Y. Narukawa, I. Niki, K. Izuno, M. Yamada, Y. Murazaki, and T. Mukai, *Jpn. J. Appl. Phys*. **41**, L371 (2002).

12. J. Kim, H. Luo, E. F. Schubert, J. Cho, C. Sone and Y. Park, *Jpn. J. Appl. Phys.*, **44**(21), L649-L651 (2005).

13. J. K. Han, J. I. Choi, A. Piquette, M. Hannah, M. Anc, M. Galvez, J. B. Talbot and J. McKittrick, *Solid State Sci. Technol*., **2**(2), R3138 (2013).

14. W.D. Collins III, M.R. Krames, G.J. Verhoeckx, and N.J.M. van Leth, *US Patent* 6,576,488 (2003).

15. N. Narendran, Y. Gu, J. P. Freyssinier-Nora and Y. Zhu, *Phys. Stat. Sol*. (A), **202,** R60-R62 (2005)

16. R. Basu, C. Randall and M. Mayo, *J. Am. Ceram. Soc*., **84**(1), 33–40 (2001).

17. S. Luo and J. B. Talbot, *J. Electrochem. Soc*. **14**8(7), H73 (2001).

18. I. Zhitomirsky and L. Gal-or, *J. Mater. Sci.: Mater. Med.*, **8**, 213 (1997).

19. K. Sakuma, K. Omichi, N. Kimura, M. Ohashi, D. Tanaka, N. Hirosaki, Y. Yamamoto, R. J. Xie and T. Suehiro, *Opt. Lett*. **29**, 2001 (2004).

20. Y. Won, H. Jang, K. Cho, Y. Song, D. Jeon and H. Kwon, *Opt. Lett*. **34**(1), 1-3 (2009).

21. J. You, N. T. Tran and F. G. Shi, *Optics Express*, **18**(5), 5055 (2010).

Chapter 8. Electrophoretic deposition of nano- and micron-sized $Ba_2SiO_4:Eu^{2+}$ phosphor particles

8.1. Abstract

Electrophoretic deposition (EPD) is a technique to deposit charged particles from a stable suspension under the force of an applied electric field. Although nanoparticles of a variety of materials have been coated by EPD, there have been few direct comparisons of EPD of nano- and micron-sized particles of the same material. The objective of this study is to compare EPD of nano-, nano core/SiO_2 shell and micron-sized $(Ba_{0.97}Eu_{0.03})_2SiO_4$ phosphor particles for application in a near-UV LED-based light source. EPD from an amyl alcohol bath was able to produce uniform films for all particle sizes, whereas uniform films were produced only of micron-sized particles in an isopropyl alcohol bath. A new equation was developed for predicting the deposited mass, considering the change in concentration of particles in the bath from both settling and deposition, showed good agreement with the experimental values.

8.2. Introduction

Electrophoretic deposition (EPD) is a useful method to fabricate particulate films [1]. The process is simple, scalable and often cost-effective. First, the particles are charged in a suspension, subsequently they are transported to an electrode under an electric field, and finally the particles adhere to the substrate. Each step has been systematically investigated in previous work in a bath of isopropyl alcohol (IPA) with nitrate salts, by studying the effects of the suspension medium chemistry on the zeta potential of the particles and the formation of the adhesive agents [2-4].

For producing white solid-state lighting devices, EPD has been used to deposit micron-sized phosphors placed above an LED. $Y_3Al_5O_{12}:Ce^{3+}$ phosphor was deposited onto a flexible indium tin oxide (ITO)-coated polymer substrate on top of blue light-emitting diodes (LEDs) [5]. In other work, both layered and blended phosphor films using Eu-activated Ca-α-SiAlON, β-SiAlON and $CaAlSiN_3$ (yellow-, green- and red-emitting, respectively) were deposited on an

ITO-coated substrate that was placed on top of a blue-emitting LED [6]. Recently, EPD was used to deposit both layered and blended phosphor films that generated white light using Eu^{2+}-activated $Sr_{2-x}Ca_xSi_5N_8$, Ba_2SiO_4, $LiCaPO_4$, $(Sr_{0.75}Ba_{0.25})_2SiO_4$ and $(Sr_{0.5}Ba_{0.5})_3SiO_5$ (red-, green-, blue-, yellow- and orange-emitting, respectively) with near-UV LEDs [7, 8]. The phosphor films must be ~10 to 40 µm thick for full conversion of the UV emission from the LED. Also the film thickness must be very uniform. It was determined that the deposited film quality was poor when a higher applied voltage was used [9]. This has led to the development of the EPD processes using lower voltages (~80 V) and longer deposition times up to 30 min [7, 8] than previous EPD processes [1-4].

Typically, micron-sized phosphors are being used in solid-state lighting. However, the micron-sized phosphors have higher optical scattering losses due to an increased optical path length and increased number of reflections or transmissions at interfaces [10]. The nano-phosphors (< 300 nm) with comparable quantum efficiency to typical micron-sized phosphors may be a mean to reduce the losses and improve efficiency of the white UV-based LEDs [11]. But it is well known that the emission intensity of the phosphor decreases as the crystallite size decreases [12]. This has been attributed to surface defect states that trap the emitted photons and thus quench the emission intensity. To alleviate the impact of surface defects in nanocrystalline powders, core/shell structured nanoparticles have been used to stabilize the surface of the nanoparticles [13, 14]. It was found that the luminescence intensity, chemical stability and thermal stability are improved by these inert shells [15-18].

$(Ba,Sr)_2SiO_4:Eu^{2+}$ phosphors are suitable for near-UV LED application due to their broad excitation band near 380 nm and intense green emission centered around 512 nm [19]. Han et al. [19] found that quantum efficiency of micron-sized phosphor powders was ~95% and showed good thermal stability up to 150°C. The most common method to prepare these phosphors is by a high temperature solid-state reaction, which results in larger (several microns) particle sizes [20-

22]. $(Ba,Sr)_2SiO_4:Eu^{2+}$ has been synthesized by sol-gel [23], combustion [24], spray pyrolysis [25] and hydrothermal processing [26]. However, the particles were usually micron-sized with an irregular morphology. Recently, a co-precipitation method was reported, producing nano-sized nearly spherical particles of ~100–500 nm diameter with a narrow size distribution [27]. The quantum efficiency of nano-sized powders was ~82–84%.

The EPD of nanoparticle dispersions and the effect of related parameters on the deposition kinetics have been studied [28]. In principle, kinetic random motion dominates the behavior of small particles, which will not settle, but stay as a stable dispersion. However, these small particles can collide due to their kinetic energy. Therefore, if there are strong attractive forces, the collisions might cause the growth of aggregates and the dispersion becomes unstable and settling occurs. When particle size increases, the attractive van der Waals forces and tendency for sedimentation increase. Deposition of nano-sized and sub-micron particles of SiC have been compared [29]. While a thick, dense deposit was prepared with submicron (500 nm) powders, nano-sized powders (50 nm) were not deposited under the same conditions; no explanation was given [29].

In this work, $(Ba_{0.97}Eu_{0.03})_2SiO_4$ was prepared by two methods, yielding either micron- (~5 μm) or nano-sized (~320 nm) particles. EPD was performed in isopropyl or amyl alcohol baths. This study directly compares EPD of nano- and micron-sized particles with the same composition. Additionally, EPD of core/shell nano-sized particles was compared with nano-sized and micron-sized particles to investigate the effect of the shell.

8.3. Experimental

$(Ba_{0.97}Eu_{0.03})_2SiO_4$ powders were synthesized by both a solid state reaction to make micron-size particles [20-22] and a co-precipitation method to produce nano-sized particles [27]. For the solid state reaction, the starting materials, $BaCO_3$ (99.99%, Alfa Aesar), SiO_2 (Sigma

Aldrich), and Eu_2O_3 (99.999%, Alfa Aesar), were stoichiometrically weighed and mixed thoroughly in an agate mortar, then heated to 1300 °C for 6 h in a slightly reducing atmosphere (5% H_2 and 95% N_2), followed by additional grinding. For the co-precipitation method, 1 ml tetraethyl orthosilicate (TEOS, 99.9%, Sigma Aldrich) was added to 10 ml ethanol with a few drops of nitric acid (70%, EM Science). The resultant solution was stirred for 30 min. Next, $Ba(NO_3)_2$ (99.999%, Alfa Aesar) and Eu_2O_3 (99.999%, Alfa Aesar) in a 2 ml dilute nitric acid solution of the desired molar ratios was dissolved in a 100 ml N,N-dimethylformamide (DMF) solution (99.9% EM Science) for 4 h at 90°C. After the solution became transparent, it was cooled to 25°C. Then the required amount of silica sol was added slowly (~2 ml/min) to the mixture while stirring. Next, a solution of 0.8 g NaOH in 8 ml water and 40 ml ethanol, used as a precipitating agent, was added slowly (~1 ml/min) to the mixture (molar ratio of Ba/Si/NaOH = 2:1:4.6) while stirring. After continuous stirring for another 10 min, the resulting precipitate was filtered and washed three times with ethanol. The powders were then dried at 80°C for 4 h. Finally, the powders were heated to 1000°C for 1 h in a slightly reducing atmosphere (5% H_2 and 95% N_2) at a rate of 5 °C/min and then cooled at a rate of 15°C/min.

Silica was coated onto the nano-sized particles by the Stöber process [30], as outlined in [18]. The silica shells were prepared by hydrolysis of TEOS in an alcohol suspension medium in the presence of water and ammonia. First, 0.05 g of the core particles was added into 50 ml ethanol. The mixture was agitated using ultrasonification for 1 h to disperse the particles. Then 1 ml of deionized water and 0.5 ml NH_4OH were added into the solution followed by an addition of 0.15 ml TEOS. The ratio between the concentrations of core particles and reagents (H_2O, NH_4OH and TEOS) was chosen to avoid self-nucleation of silica. In order to prevent heating of the solution and to better disperse the nanoparticles, ice was frequently added into ultrasonification bath to keep the bath temperature at 20℃. After 3 h in the bath to form the SiO_2

shell, the core/shell particles were centrifugally separated from the suspension and rinsed with ethanol.

EPD was carried out in a bath consisting of the phosphor powders, $Mg(NO_3)_2 \cdot 6H_2O$, and either amyl alcohol (viscosity, η = 3.7 mPa·s, density, ρ = 0.810 g/cm^3) or IPA (η = 2.0 mPa·s, ρ = 0.786 g/cm^3). Practically, one may not want to use amyl alcohol since it has a strong and penetrating smell, however it is only slightly soluble in water (28 g/L) compared to IPA (miscible) [31]. The $Mg(NO_3)_2 \cdot 6H_2O$ concentration ranged from approximately 10^{-5} to 10^{-3} M, as determined by previous work [2]. The zeta potentials of the powders were measured in a diluted suspension with various magnesium nitrate concentrations in amyl alcohol or IPA with a Zeta Plus meter (Brookhaven Instruments Corporation, Holtsville, NY).

A 1.1 mm thick ITO-coated glass slide (2.5 cm × 5.1 cm, 70 ohms/sq., Bayview Optics, Dover-Foxcroft, ME) was used as the cathode, and an aluminum sheet was used as the anode. The deposition area was 2.5 cm × 2.5 cm. The electrodes were placed vertically and parallel to each other in a suspension with 1 cm separation.

For EPD, a concentration of 5 g/L of powder was dispersed in 60 ml of alcohol with $Mg(NO_3)_2 \cdot 6H_2O$. The nitrate concentration was chosen to obtain the maximum positive zeta potential. The zeta potential has a negative value in the pure alcohols and then increases with magnesium nitrate concentration to a maximum positive value and then decreases. The suspension was sonicated for 1 hr prior to deposition to improve the dispersion of the powders and assure the complete dissolution of $Mg(NO_3)_2 \cdot 6H_2O$. A voltage of 80 V was applied by a power supply for 30 s - 1800 s to give a deposit thickness ranging from ~ 10 μm to 40 μm.

After the deposition process, the deposited samples were removed from the bath and dried in air. The deposits were analyzed in terms of their deposit weight, thickness and photoluminescence (PL) emission spectra. The spectra were taken using a Jobin Yvon Triax 180

monochromator, SpectrumOne charge-coupled device detection system with a 380 nm UV as the excitation source. The thicknesses of the films and average particle sizes were estimated from micrographs taken by a field emission scanning electron microscope (FEI-XL30, FEI Company, Hillsboro, OR). The thickness of film was calculated from cross-sectional SEM micrographs by averaging 20 places on the micrograph across the film.

8.4. Results and discussion

Fig. 8.1. shows SEM images of the phosphor particles. From an average of 10 particles, the size of micron-, nano- and core/shell nano-particles were determined to be 5 ± 3 μm, 320 ± 200 nm and 360 ± 170 nm, respectively. The thickness of the silica shells was 40 ± 15 nm. Magnesium nitrate concentrations and maximum zeta potential values for each phosphor in the EPD baths are shown in Table 8.1. In amyl alcohol, a higher concentration of nitrate salt was needed to obtain the maximum zeta potential value compared to the IPA bath and an even higher concentration of nitrate salt was necessary for the nano- and core/shell nano-particles compared to micron particles due to the difference in the viscosity of suspension medium and larger surface area of the nanoparticles.

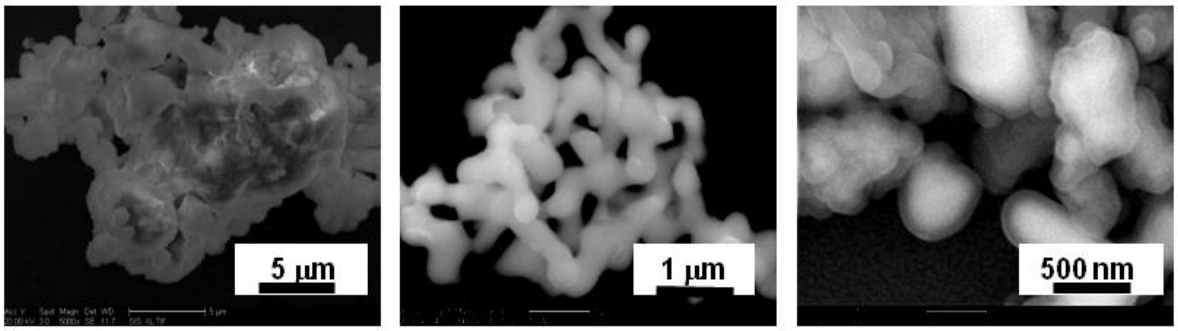

(a) (b) (c)

Figure 8.1. SEM micrographs of individual phosphor, Eu^{2+}-activated Ba_2SiO_4, (a) micron-sized particle (~5 μm) (b) nano-sized particle (~320 nm) and (c) core/shell nano-sized particle (~360 nm).

Table 8.1. Magnesium nitrate concentrations and maximum zeta potential values for each EPD bath.

Particle size	**Suspension medium**	**$Mg(NO_3)_2$ concentration (M)**	**Zeta Potential (mV)**
Micron	IPA	1.0×10^{-5}	35 ± 3
Nano	IPA	5.0×10^{-5}	34 ± 2
Micron	Amyl alcohol	1.0×10^{-4}	22 ± 3
Nano	Amyl alcohol	5.0×10^{-4}	21 ± 3
Nano (core/shell)	Amyl alcohol	1.0×10^{-3}	22 ± 3

In our previous work, micron-sized particles were deposited by EPD from a bath of IPA with 10^{-5} M $Mg(NO_3)_2$ which resulted in uniform films [8]. However, when a suspension of nano-sized particles in this bath was used, a non-uniform and porous film resulted, as shown in Fig. 8.2. The poor quality of the deposit is attributed to excessive hydrogen evolution during deposition. The increased surface area of nano-sized particle can adsorb a larger quantity of water than for micron-sized particles [32]. With that additional water in the bath, more hydrogen evolution can occur at the cathode due to water electrolysis. Thus, careful control of the amount of water in the bath is needed to prevent excessive hydrogen evolution during EPD of nano-sized phosphors. Therefore, amyl alcohol, which has low water solubility, was used as the EPD suspension medium instead of IPA.

The deposit weight and thickness deposits of nano- and micron-sized particles from a bath of amyl alcohol as a function of time are shown in Fig. 8.3. For short times (< 10 min), the deposit weight and thickness increased linearly with time. The deposit thickness for the micron-sized particle leveled to 26 µm at 15 min, whereas the deposit thickness of nano-sized particle plateaued at 33 µm at ~30 min. However, the thickness of core/shell nano-sized particles kept increasing to 30 min. Fig. 8.4. shows cross-sectional SEM micrographs of the deposits as a function of deposition time. The packing fraction of particles, Π, in an EPD film can be calculated using the following equation [33]:

$$\Pi = \frac{M}{h\rho_p} \tag{1}$$

where M is the weight of the deposited film per area of the sample, h is the thickness of the deposit, and ρ_p is the material density of Ba_2SiO_4 (5500 kg/m^3). Table 8.2. lists the measurements used to calculate the packing fraction after 10 min deposition time. The packing fraction was determined to be ~0.43–0.45 for films of all particles.

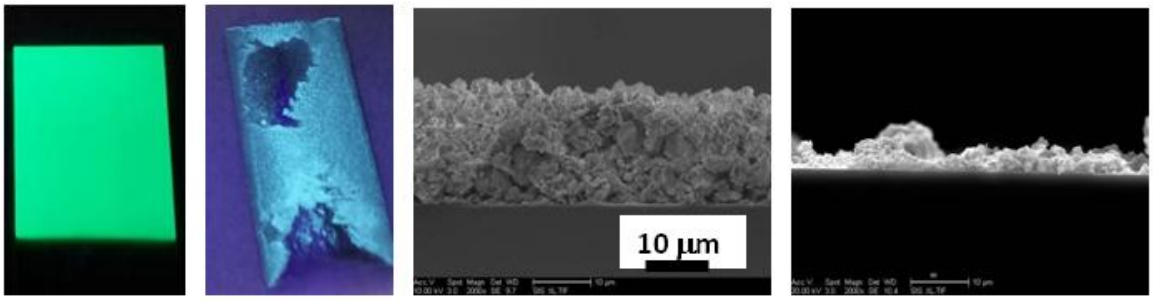

(a) (b) (c) (d)

Figure 8.2. A comparison of film quality of micron-sized and nano-sized powders deposited for 10 min from an IPA bath. Photographs of phosphor deposits (2.5×2.5 cm^2 excited by 365 nm) of (a) micron- and (b) nano-sized particles. Cross-sectional SEM micrographs of (c) micron- (d) nano-sized particles.

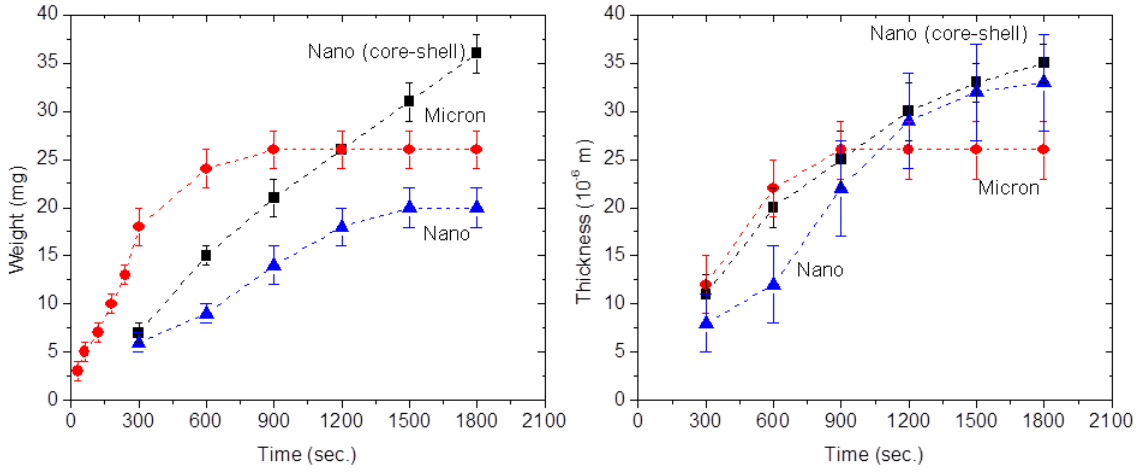

(a) (b)

Figure 8.3. (a) Deposit weight (per 6.25 cm^2) and (b) thickness taken from SEM measurement of individual phosphors as a function of deposition time.

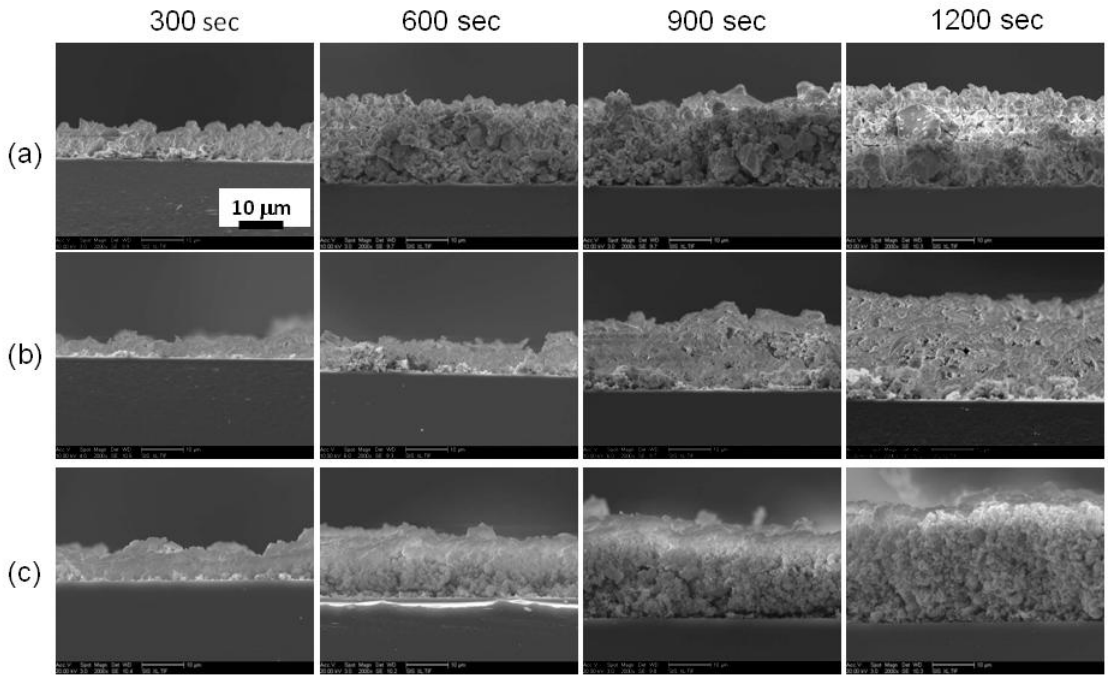

Figure 8.4. Cross-sectional SEM micrographs showing the thickness as a function of deposition time: (a) micron-, (b) nano-sized and (c) core/shell nano-sized particles.

Table 8.2. Deposit areal density and thickness from weight and SEM measurements used to estimate the packing fraction, Π (Eqn. (1)) for 10 min deposition in amyl alcohol.

Particle	**Deposit Density, *M* (**mg/cm^2)	**Thickness, *h* (**μm)
nano	2.6 ± 0.1	11 ± 6
micron	4.2 ± 0.2	17 ± 4
core/shell nano	4.0 ± 0.1	16 ± 3

The deposited mass, *m* can be estimated by the Hamaker equation [34]:

$$m = C_S v_e A_S t \tag{2}$$

where C_s is the suspension concentration, v_e is the electrophoretic velocity, A_s is the deposition area, and *t* is the deposition time. The Hamaker equation is valid only for short times when C_s and the electric field are assumed to be constant.

However, during EPD, the amount of particles removed from the suspension increases with time, thereby decreasing the concentration in the bath. To account for this, Sakar and Nicholson [35, 36] expressed the deposited mass as:

$$m(t) = m_0\left(1 - e^{-t/\tau}\right), \tag{3}$$

where m_0 is the initial mass of powder and τ is the characteristic time scale given by:

$$\tau = \frac{V}{\mu A_s E}\ , \tag{4}$$

where *V* is the volume of suspension, μ is the electrophoretic mobility, and *E* is the electric field. This equation indicates that the deposition rate is expected to decrease exponentially as a function of time due to depletion of the bath by particle deposition.

In reality, the variables C_s and v_e change with time because of loss of material from the suspension and deposition of a dielectric layer on the electrode, respectively. In order to incorporate the time dependence of C_s and v_e, one has to assume that Eq. (2) is valid for a short time, Δt only when changes in both the parameters could be assumed to be infinitesimally small. Eq. (2) can then be expressed as:

$$\Delta m(t) = C_s(t) v_e(t) A_s \Delta t \tag{5}$$

In the limit as $\Delta t \to 0$, Eq. (5) can be expressed as:

$$\frac{dm(t)}{dt} = C_s(t) v_e(t) A_s \tag{6}$$

If the time dependence of C_s and v_e is known, Eq. (6) could be integrated to obtain the deposited material, $m(t)$ as a function of time.

The electrophoretic velocity equals the product of the electrophoretic mobility, μ, and the electric field, E. The electrophoretic mobility can be estimated from the Smoluchowski equation [1]:

$$\mu = \left(\frac{\xi \varepsilon_r \varepsilon_o}{\eta}\right), \tag{7}$$

where ξ is the measured zeta potential, ε_r is the relative permittivity of the suspension medium, ε_0 is the vacuum permittivity and η is the viscosity of suspension medium. Note that the electrophoretic velocity is not dependent on particle size and does not change with time. But, the electrophoretic velocity, υ_e in Eq. (2) is given by

$$\upsilon_e = \mu E \tag{8}$$

Since the electric field will decrease as the thickness of deposit increases, this will eventually retard and even limit the deposition process. In the present formulation, it is assumed that this effect is negligible compared to change in concentration.

The settling velocity v_s, can be estimated by Stokes' law:

$$v_s = \frac{2}{9}\frac{(\rho_p - \rho_f)}{\eta} g r^2, \tag{9}$$

where ρ_f is the density of fluid, g is the gravitational acceleration, and r is the radius of a spherical particle. Note that the settling velocity will depend on size of the particles. The nanosized particles will settle more slowly than the micron size particles.

The concentration in the suspension may change due to both deposition and settling. From a mass balance, the change in suspension concentration, C_s, due to settling and deposition can be written as:

$$\frac{dC_S}{dt} = -C_S v_s \frac{A}{V} - \frac{1}{V}\frac{dm}{dt} \tag{10}$$

where A is the cross-section area of the bath and V is the volume of the bath. However, the loss of concentration associated with the deposition can be considered minimal (~0.001 g/L) compared to the initial bath concentration (5 g/L) in our experiments, so the second term in Eqn. (10) can be neglected. After integrating Eq. (10), the time-dependent concentration is:

$$C_S = C_{S,0} exp\left(-\frac{v_s A}{V} t\right) \tag{11}$$

where $C_{S,0}$ = initial bath concentration.

The parameters used to calculate v_e and v_s are given in Table 8.3. The electrophoretic velocity was determined to be v_e = 5.9 × 10^{-6} m/s from Eqn. (8). The settling velocities for a micron-size particle (~5 μm) and nano-size particle (~320 nm) were estimated to be 1.7 × 10^{-5} m/s and 7.0 × 10^{-8} m/s, respectively, from Eqn. (9). The settling velocity for micron-sized particles is about 3 times greater than the electrophoretic velocity, whereas for nano-sized it is ~100 times smaller. Larger micron-sized particles can readily settle from solution, decreasing their concentration, whereas the suspension with nano-sized particles is more stable, maintaining a nearly constant concentration for a longer time.

Using $C_s(t)$ from Eqn. (11) in Eqn. (6), one obtains

$$\frac{dm}{dt} = C_{S,0} A_S v_e exp\left(-\frac{v_s A}{V} t\right). \tag{12}$$

Integrating Eq. (12) yields the mass deposited as a function of time:

$$m(t) = \frac{C_{S,0} A_S v_e V}{v_s A}\left[1 - exp\left(-\frac{v_s A}{V} t\right)\right]. \tag{13}$$

Table 8.3. Parameters used for calculations of the electrophoretic velocity (v_e), settling velocity (v_s) and mass deposited (m) in Eqns. (2)-(13).

Parameter	Symbol	Value
Material density (Ba_2SiO_4)	ρ_p	5500 kg/m^3
Density of amyl alcohol	ρ_f	810 kg/m^3
Density of isopropyl alcohol	ρ_f	786 kg/m^3
Viscosity of amyl alcohol	η	3.7 mPa·s
Viscosity of isopropyl alcohol	η	2.0 mPa·s
Standard acceleration of gravity	g	9.81 m/s^2
Relative permittivity of amyl alcohol	ε_r	13.9
Relative permittivity of isopropyl alcohol	ε_r	18.3
Vacuum permittivity	ε_0	8.85×10^{-12} F/m
Zeta potential in amyl alcohol	ξ	22 mV
Zeta potential in isopropyl alcohol	ξ	35 mV
Electric field	E	8000 V/m
Initial bath concentration	$C_{S,0}$	5 kg/m^3
Cross-sectional area of the bath	A	1.26 x 10^{-3} m^2
Area of the deposit	A_s	6.25 x 10^{-4} m^2
Volume of bath	V	6 x 10^{-5} m^3

The mass deposited from Eq. (13) considers both the change in concentration of particles in the bath from settling and deposition. The experimental and theoretical values of deposited mass versus time from Eqns. (2), (3) and (13) are plotted in Fig. 8.5. (a) for nano-sized particles in the amyl alcohol bath. The experimental values for nano- and core/shell nano-sized particles are in good agreement with the predictions from Eq. (13).

However, there is a discrepancy between the measurements and theory for the micron-sized particles, as shown in Fig. 8.5. (b). The experimental deposited mass is higher than the theoretical values. One possible explanation is the presence of vertical concentration gradients in the bath due to Rayleigh–Taylor (R-T) instability. If particles settle through a stratified bath, instabilities may develop and the particle concentration can change locally [37]. This condition occurs when a denser higher particle concentration region is on top of a less dense, lower particle concentration. The local concentration has been found to increase up to a factor of four due to instabilities [37]. During the deposition process, the particle concentration at the bottom of the bath can be lowered locally because particles are removed by the deposition, resulting in a higher particle concentration at the top of the bath. If the suspension concentration were higher by a factor of three, the deposit weight data would agree with the Hamaker equation (Eq. (2)) for short deposition times.

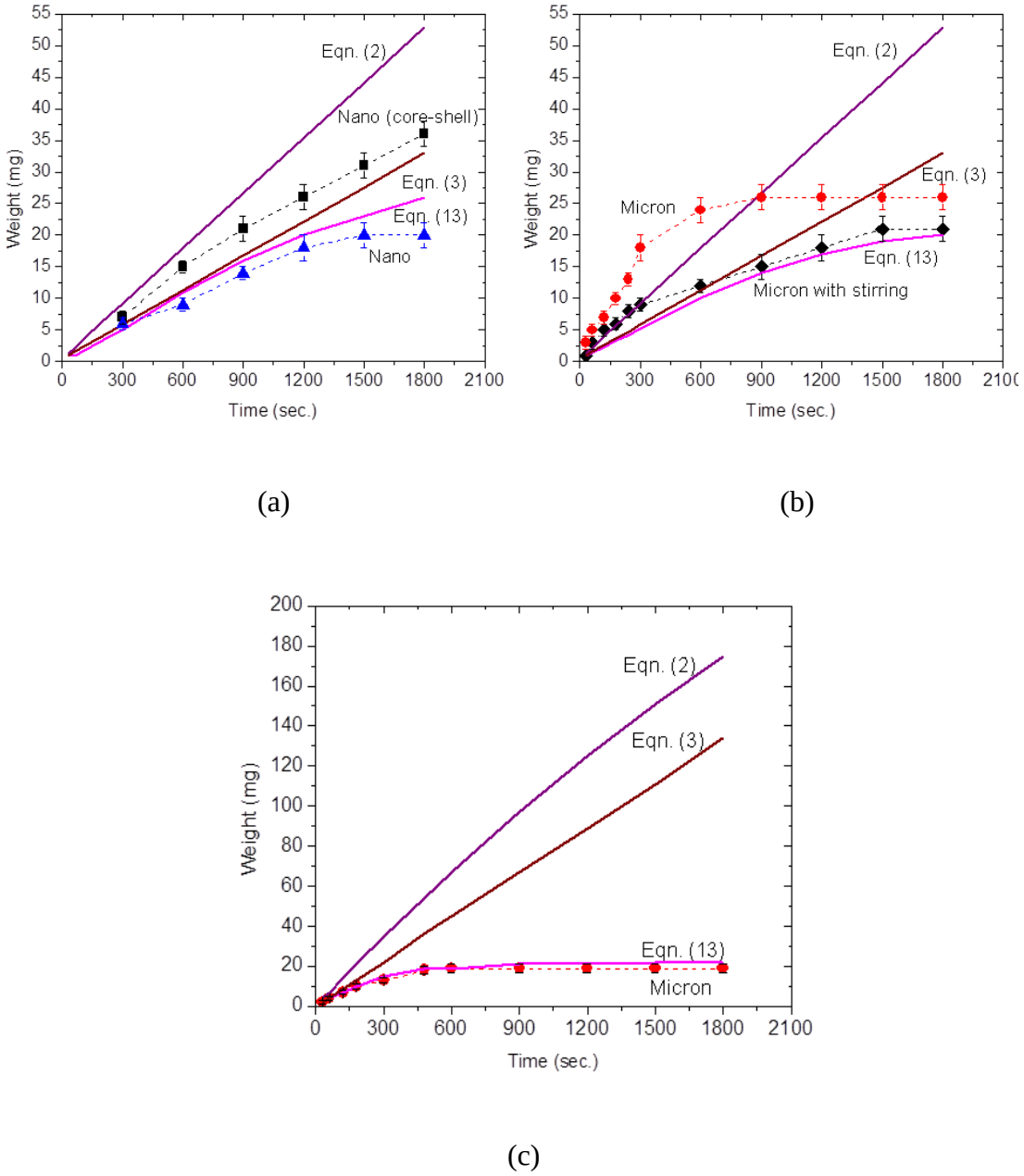

Figure 8.5. Plot of experimental and predicted deposit weight as a function of deposition time. (a) nano-sized particles in amyl alcohol bath, (b) micron-sized particles in amyl alcohol bath, (c) micron-sized particles in isopropyl alcohol bath. Eqn. (2) line is the Hamaker equation [34], Eqn. (3) is from Sakar and Nicholson [35] and Eqn. (13) is from the new equation considering the change in concentration of particles in the bath from both settling and deposition.

The R-T instability of the suspension may occur under a special set of conditions [37]. First the particle Reynolds number ($Re_p = 2v_s\rho_p r/\eta$) must be very small (Re_p <<1). For the 5 µm diameter particles, Re_p = ~ 2×10^{-5}. Note that as the volume fraction of the particles ($\phi = C_s/\rho_p$) is ~10^{-3}, settling can be assumed to unhindered. The Atwood number is a dimensionless density ratio used in the study of hydrodynamic instabilities in density-stratified flows defined as:

$$A = \frac{\rho_h - \rho_l}{\rho_h + \rho_l} \tag{14}$$

where ρ_l and ρ_h are the density at the lower and higher concentrations, respectively [38]. For *A* close to 0, RT instability flows take the form of symmetric fingers of fluid; for *A* close to 1, the much lighter fluid beneath the heavier fluid takes the form of larger bubble-like plumes [39]. The suspension density ρ_s can be estimated by a simple rule of mixtures relationship:

$$\rho_S = \phi\rho_p + (1 - \phi)\rho_f \tag{15}$$

For amyl alcohol, the maximum ρ_s = 0.814 g/cm^3, which leads to a maximum *A* = ~0.003.

If both particle and fluid Reynolds numbers are low as in this study, convection will dominate if [37]:

$$\frac{v_c}{v_s} = \frac{\Delta\rho l^2}{4(\rho_p - \rho_f)r^2} \gg 1 \tag{16}$$

where v_c is the fluid convective velocity, $\Delta\rho = \rho_h - \rho_l$ and *l* is the height of the unstable region (4.8 cm). For convective instability to occur in our experiments, $\Delta\rho$ need only to be greater than ~10^{-7}. The convective instability also would increase the particle concentration at the substrate, which will increase the deposited weight from that predicted from the Hamaker equation (Eqn. (2)). Therefore, the conditions of R-T instability are met in our experiment.

The RT instabilities should not occur if the suspension is well-mixed. Therefore, EPD was performed with gentle stirring of the bath by a small magnetic stirrer placed in the bottom of the bath under the same deposition conditions. With stirring, the experimental values showed

agreement with the Hamaker equation (Eqn. (2)) up to 5 min, and then agree with the Eqn. (13) for longer times when settling becomes significant.

To investigate if the suspension medium has an influence, the micron-sized particles were deposited without stirring in the more commonly used suspension medium, IPA. The experimental mass of the deposits and the predicted ones from Eqns. (2), (3) and (13) are shown in Fig. 8.5. (c). The predicted values from Eqns. (2) and (3) were significantly larger than the experimental values at longer deposition times. However, the experimental values fit well to the predicted ones from Eqn. (13), regardless of deposition time. No additional particles were deposited after ~10 min most likely due to decrease of the electric field on the electrode due to the resistance of the film [8]. Thus, the electric field contribution needs to be taken into account to accurately predict the deposited mass at longer deposition times.

Fig. 8.6. shows SEM micrographs and PL emission spectra of phosphors with similar thickness (~30 μm) for EPD deposits of (a) micron-, (b) nano-sized and (c) core/shell nano-sized particles. The PL intensity of the deposit of nano-sized particles was 40% of the deposit of micron-sized particles as observed in previous study [27]. The emission intensity of the film of the core/shell particles is ~20% higher than the deposit of bare core particles. This indicates that the inert shells play a significant role in reducing the surface defects that cause luminescence quenching in sub-micron sized particles, which has also been observed with other core/shell phosphor compositions [13-18].

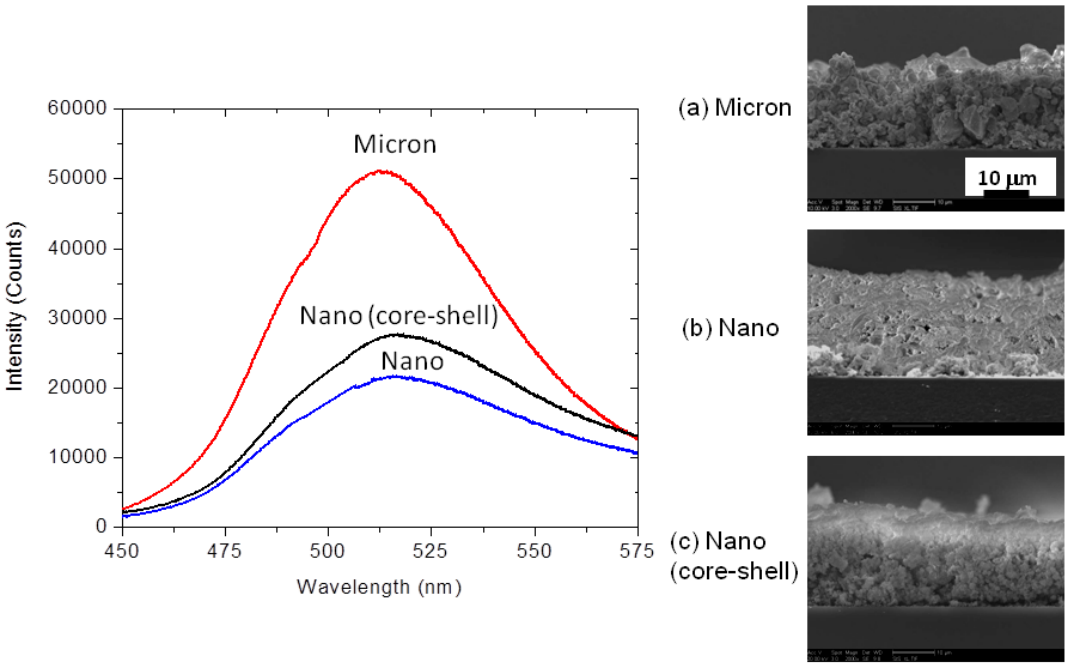

Figure 8.6. Cross-sectional SEM micrographs and PL emission spectra of EPD films with ~30 µm thickness for (a) micron-, (b) nano-sized and (c) core/shell nano-sized particles.

8.5. Conclusions

Nano-, nano core/SiO_2 shell and micron-sized $(Ba_{0.97}Eu_{0.03})_2SiO_4$ phosphors were successfully deposited by electrophoretic deposition in an amyl alcohol bath for times up to 30 min. A new equation (Eqn. (13)) was developed that accounts for the change in concentration of particles in the bath from both settling and deposition, which better predicts the deposited mass. The experimental values for deposited mass as a function of time for nano- and core/shell nano-sized particles showed good agreement with this equation, however not for the micron-sized particles. This was attributed to vertical particle concentration gradients in the bath. To eliminate these possible gradients, the bath of micron-sized particles was stirred gently, which gave deposit weights in excellent agreement with the predicted ones from Eqn. (13), verifying that instabilities occurred in the amyl alcohol bath. The deposited mass for micron-sized particles from an isopropyl alcohol bath that was not stirred showed good agreement with the theoretical values from Eqn. (13), indicating that the concentration gradients did not develop in this bath. Nano-sized particles were coated with a SiO_2 shell improved the photoluminescence emission intensity of deposited films compared to bare core particles, but both were less than films of the micron-sized particles.

8.6. Acknowledgments

This work is funded by US Department of Energy Grant # DE-EE0002003. Chapter 8, in full, is a reprint of the material as it appears in Journal of The Electrochemical Society, Jae Ik Choi, Maria Anc, Alan Piquette, Mark. E. Hannah, Kailash C. Mishra, Jan B. Talbot, and Joanna McKittrick, Vol. 161(3), pp. D111-D117 (2014). The dissertation author was the primary author of this paper.

References

1. J. B. Talbot, E. Sluzky and S. K. Kurinec, "Electrophoretic deposition of monochrome and color phosphor screens for information displays," *J. Materials Science*, **39**, 771-778 (2004).

2. M. J. Shane, J. B. Talbot, E. Sluzky, and K. R. Hesse, "Zeta potential of phosphors," *Colloids and Surfaces*, **96**, 301-305 (1995).

3. M. J. Shane, J. B. Talbot, R. D. Schreiber, C. L. Ross, E. Sluzky, and K. R. Hesse, "Electrophoretic deposition of phosphors: I. Conductivity and zeta potential measurements," *J. Colloid Interface Sci*., **165**, 325-333 (1994).

4. B. E. Russ and J. B. Talbot, "A study of the adhesion of electrophoretically deposited phosphors," *J. Electrochem. Soc*. **145**(4), 1245-1252 (1998).

5. J. Yum, S. Kim and Y. Sung, "$Y_3Al_5O_{12}$:$Ce_{0.05}$ phosphor coatings on a flexible substrate for use in white light-emitting diodes," *Colloids and Surfaces A: Physicochem. Eng. Aspects*, **251**, 203-207 (2004).

6. T. Kitabatake, T. Uchikoshi, F. Munakata, Y. Sakka and N. Hirosaki, "Emission color tuning of laminated and mixed SiAlON phosphor films by electrophoretic deposition," *Journal of the Ceramic Society of Japan*, **118**, 1-4 (2010).

7. J. I. Choi, E. Sluzky, M. Anc, A. Piquette, M. Hannah, K.C. Mishira, J. McKittrick and J. B. Talbot, "EPD of phosphors for display and solid state lighting technologies," *Key Engineering Materials*., **507**, 149-153 (2012).

8. J. I. Choi, M. Anc, A. Piquette, M. Hannah, K.C. Mishra, J. McKittrick and J. B. Talbot, "Electrophoretic deposition of phosphors for white solid state lighting using near UV-emitting LEDs," *Solid State Sci. Technol*., **2**(7), R153-R159 (2013).

9. R. Basu, C. Randall and M. Mayo, "Fabrication of dense zirconia electrolyte films for tubular solid oxide fuel cells by electrophoretic deposition," *J. Am. Ceram. Soc.*, **84**(1), 33–40 (2001).

10. N. Taskar, R. Bhargava, J. Barone, V. Chhabra, V. Chabra, D. Dorman, A. Ekimov, S. Herko, and B. Kulkarni. "Quantum-confined-atom-based nanophosphors for solid state lighting," In *Third International Conference on Solid State Lighting, Proceedings of SPIE*, **5187**, 133-141 (2004).

11. N. Narendran, "Improved performance white LED," *Proc. SPIE*, **5941**, 594108-594108-6 (2005).

12. J. K. Han, J. I. Choi, A. Piquette, M. Hannah, M. Anc, M. Galvez, J. B Talbot and J. McKittrick, "Phosphor development and integration for near-UV LED solid state lighting," *Solid State Sci. Technol*., **2** (2) R3138-R3147 (2013).

13. L. M. Liz-Marz´an, M. Giersig, and P. Mulvaney, "Synthesis of nanosized gold-silica core-shell particles," *Langmuir,* **12**, 4329-4335 (1996).

14. M. Darbandi, W. Hoheisel, and T. Nann, "Silica coated, water dispersible and photoluminescent $Y(V,P)O_4:Eu^{3+},Bi^{3+}$ nanophosphors," *Nanotechnology*, **17**, 4168-4173 (2006).

15. O. Lehmann, K. Kompe, and M. Haase, "Synthesis of Eu^{3+}-doped core and core/shell nanoparticles and direct spectroscopic identification of dopant sites at the surface and in the interior of the particles," *J. Am. Chem. Soc.*, **126**, 14935-14942 (2004).

16. P. Zhu, Q. Zhu, H. Zhu, H. Zhao, B. Chen, Y. Zhang, X. Wang, and W. Di, "Effect of SiO_2 coating on photoluminescence and thermal stability of $BaMgAl_{10}O_{17}$: Eu^{2+} under VUV and UV excitation," *Opt. Mater.*, **30**, 930-934 (2008).

17. W. B. Im, H. S. Yoo, S. Vaidyanathan, K. H. Kwon, H. J. Park, W. I. Kim, and D. Y. Jeon, "A novel blue-emitting silica-coated $KBaPO_4:Eu^{2+}$ phosphor under vacuum ultraviolet and ultraviolet excitation," *Mater. Chem. Phys.*, **115**, 161-164 (2009).

18. J. K. Han, G. A. Hirata, J. B. Talbot, and J. McKittrick, "Luminescence enhancement of $Y_2O_3:Eu^{3+}$ and $Y_2SiO_5:Ce^{3+},Tb^{3+}$ core particles with SiO_2 shells," *Mater. Sci. Eng. B*, **176**, 436-441 (2011).

19. J. K. Han, M. E. Hannah, A. Piquette, G. A. Hirata, J. B. Talbot, K. C. Mishra, and J. McKittrick, "Structure dependent luminescence characterization of green-yellow emitting $Sr_2SiO_4:Eu^{2+}$ phosphors for near UV LEDs," *J. Lumin.*, **132**, 106-109 (2012).

20. S. H. M. Poort, W. Janssen, and G. Blasse, "Optical properties of Eu^{2+}-activated orthosilicates and orthophosphates," *J. Alloys Comp.*, **260**, 93-97 (1997).

21. Z. Pan, H. He, R. Fu, S. Agathopoulos, and X. Song, "Influence of Ba^{2+}-doping on structural and luminescence properties of $Sr_2SiO_4:Eu^{2+}$ phosphors," *J. Lumin.*, **129**, 1105-1108 (2009).

22. M. Zhang, J. Wing, Q. Zhang, W. Ding, and Q. Su, "Optical properties of $Ba_2SiO_4:Eu^{2+}$ phosphor for green light-emitting diode (LED)," *Mater. Res. Bull.*, **42**, 33-39 (2007).

23. W. H. Hsu, M. H. Sheng, and M. S. Tsai, "Preparation of Eu-activated strontium orthosilicate ($Sr_{1.95}SiO_4:Eu_{0.05}$) phosphor by a sol-gel method and its luminescent properties," *J. Alloys. Comp.*, **467**, 491-495 (2009).

24. B. Lei, K. I. Machida, T. Horikawa, and H. Hanzawa, "Facile combustion route for low-temperature preparation of Sr_2SiO_4:Eu^{2+} phosphor and its photoluminescence properties," *Jpn. J. Appl. Phys.*, **49**, 095001-095001-6 (2010).

25. H. S. Kang, Y. C. Kang, K. Y. Jung, and S. B. Park, "Eu-doped barium strontium silicate phosphor particles prepared from spray solution containing NH_4Cl flux by spray pyrolysis," *Mater. Sci. Eng. B*, **121**, 81-85 (2005).

26. Sato N, Kawachi M, Noto K, Yoshimoto N, Yoshizawa M. Effect of particle size reduction on crack formation in electrophoretically deposited YBCO films. Physica C;357–360:1019–22 (2001). 25. Heavens N. Electrophoretic deposition as a processing route for ceramics. In: Binner GP, editor. Advanced ceramic processing and technology, vol. 1. Park Ridge (NJ), USA: Noyes Publications; p. 255–83 [chapter 7] (1990).

26. T. Sakamoto, K. Uematsu, T. Ishigaki, K. Toda, and M. Sato, "Development of gas-solid phase hybrid synthesis method of single crystal Ba_2SiO_4:Eu^{2+}," *Key Engineering Materials*, **485**, 325-328 (2011).

27. J. K. Han, M. E. Hannah, *A. Piqu*et**te,** J. B. Talbot, K. C. Mishra, and J. McKittrick, "Nano- and submicron sized europium activated silicate phosphors prepared by a modified co-precipitation method," *Solid State Sci. Technol*.**, 1**(3), R98-R102 (2012).

28. R. Moreno and B. Ferrari, "Nanoparticles dispersion and the effect of related parameters in the EPD kinetics," chapter 2, Springer Book 978-1-4419-9730-2 (Online) "Electrophoretic deposition of nanomaterials," editor: J. H. Dickerson and A.R. Boccaccini (2012).

29. S. Novak, K. König and A. Iveković, "Electrophoretic deposition in production of ceramic matrix composites," Chapter 8, Springer Book 978-1-4419-9730-2 (Online) "Electrophoretic deposition of nanomaterials," editor: J. H. Dickerson and A.R. Boccaccini (2012).

30. W. Stöber, A. Fink, E. Bohn, "Controlled growth of monodisperse silica spheres in the micron size range,", *J. Colloid Interface Sci*., **26**, 62-69 (1968).

31. Lide, R. David., ed. *Handbook of Chemistry and Physics* (87 ed.). Boca Raton, FL: CRC Press. (1998).

32. A. Navrotsky, "Nanoscale effects on thermodynamics and phase equilibria in oxide systems," *ChemPhysChem*, 12, 2207 – 2215 (2011).

33. S. Luo and J. B. Talbot, "Optical characterization of electrophoretically deposited phosphor," *J. Electrochem. Soc.*, **148**(7), H73-H79 (2001).

34. H. C. Hamaker, "Formation of a deposit by electrophoresis," *Trans. Farad. Soc.*, **36**, 279-287 (1940).

35. P. Sarkar. and P. S. Nicholson, "Electrophoretic deposition (EPD): mechanisms, kinetics, and application to ceramics," *J. Am. Ceram. Soc.*, **79**(8), 1987-2002 (1996).

36. B. Ferrari and R. Moreno, "EPD kinetics: A review," *Journal of the European Ceramic Society*, 30, 1069-1078 (2010).

37. F. Blanchette and J. W. M. Bush, "Particle concentration evolution and sedimentation-induced instabilities in a stably stratified environment," *Phys. Fluids*, **17**, 073302-073302-11 (2005).

38. J. Glimm, J. W. Grove, X. L. Li, W. Oh, and D. H. Sharp, "A critical analysis of Rayleigh–Taylor growth rates," *Journal of Computational Physics*, **169(2)**, 652-677 (2001).

39. S. B. Dalziel, "Rayleigh-Taylor instability: experiments with image analysis," *Dynamics of Atmospheres and Cceans*, **20(1)**, 127-153 (1993).

Chapter 9. Conclusions and recommendations for future work

The main objectives of this research focused on depositing phosphors by electrophoretic deposition in a "remote phosphor" configuration for a UV-LED-based light source for improved white light extraction efficiency. It was demonstrated that electrophoretic deposition (EPD) can be used to deposit red-, green-, blue-, yellow- and orange-emitting phosphors to generate white light using a near UV-emitting LED by either depositing a phosphor blend or sequentially individual phosphor compositions.

- For uniform deposition with a specified thickness, controlling the deposition process during EPD needs to be understood. Two basic but competing factors must be evaluated. Phosphors move horizontally when the electric field is applied, but they also move vertically due to the settling.
- The EPD blend deposits, composed of both three and four phosphor compositions, emit white light located on or near the black body line on the CIE chromaticity diagram which attained the DOE goal of obtaining white light with a CCT of ~3000K and a high CRI (>80).
- Phosphor films were prepared by sequential deposition of red/orange and green/blue compositions to generate white light. The layered films were flipped over and illuminated in this orientation, which showed approximately the same luminescence characteristics. No change in the ratio of the reabsorption of green/blue emission by the red/orange phosphor was found regardless of the deposited order of the layered films. Therefore, the order of phosphor deposition was found to be not important.
- The blend deposition is a better method of EPD than the sequential deposition as due to easier emission color tuning for the application of EPD of phosphors for white solid state lighting.

Although nanoparticles of a variety of materials have been coated by EPD, there have been few direct comparisons of EPD of nano- and micron-sized particles of the same material. The objective of another study was to compare EPD of nano-, nano core/SiO_2 shell and micron-sized $(Ba_{0.97}Eu_{0.03})_2SiO_4$ phosphor particles for application in a near-UV LED-based light source. $(Ba_{0.97}Eu_{0.03})_2SiO_4$ was prepared by two methods, yielding either micron- or nano-sized particles. EPD was performed in isopropyl or amyl alcohol baths. This study directly compares EPD of nano- and micron-sized particles with the same composition. Additionally, EPD of core/shell nano-sized particles was compared with nano-sized and micron-sized particles to investigate the effect of the shell.

- When a suspension of nano-sized particles in IPA bath was used, a non-uniform and porous film resulted. The poor quality of the deposit was due to excessive hydrogen evolution during deposition. The increased surface area of nano-sized particle can adsorb a larger quantity of water than for micron-sized particles. Therefore, more hydrogen evolution can occur at the cathode by water electrolysis. Thus, careful control of the amount of water in the bath is needed to prevent excessive hydrogen evolution during EPD of nano-sized phosphors.
- EPD from an amyl alcohol bath, which has low water solubility, was able to produce uniform films for all particle sizes, whereas uniform films were produced only of micron-sized particles in an isopropyl alcohol bath.
- A new equation was developed for predicting the deposited mass, considering the change in concentration of particles in the bath from both settling and deposition, showed good agreement with the experimental values.
- The experimental values for deposited mass as a function of time for nano- and core/shell nano-sized particles showed good agreement with a new equation, however not

for the micron-sized particles. This was attributed to vertical particle concentration gradients in the bath.

- To eliminate these possible gradients, the bath of micron-sized particles was stirred gently, which gave deposit weights in excellent agreement with the predicted ones from a new equation, verifying that instabilities occurred in the amyl alcohol bath. The deposited mass for micron-sized particles from an isopropyl alcohol bath that was not stirred showed good agreement with the theoretical values from a new equation, indicating that the concentration gradients did not develop in this bath.
- Nano-sized particles were coated with a SiO_2 shell improved the photoluminescence emission intensity of deposited films compared to bare core particles. The emission intensity of the film of the core/shell particles is ~20% higher than the deposit of bare core particles. This indicates that the inert shells play a significant role in reducing the surface defects that cause luminescence quenching in sub-micron sized particles, which has also been observed with other core/shell phosphor compositions, but the PL intensities were less than films of the micron-sized particles.

Future work for this research is as follows. First, micron-sized phosphors are typically being used in solid-state lighting. However, the micron-sized phosphors have higher optical scattering losses due to an increased optical path length and increased number of reflections or transmissions at interfaces as discussed in Chapters 4 and 8. The nano-sized phosphors with comparable quantum efficiency to typical micron-sized phosphors may be a mean to reduce the losses and improve efficiency of the white UV-based LEDs. However, the emission intensity of the phosphor decreases as the crystallite size decreases due to surface defect states that trap the emitted photons and thus quench the emission intensity. Therefore, core/shell structured nanoparticles have been used to stabilize the surface of the nanoparticles. Other promising

nanophosphors EPD besides $(Ba_{0.97}Eu_{0.03})_2SiO_4$ needs to be further studied to understand the effects of nano-sized phoshors.

Second, the influence of the emission wavelength of the excitation source can be diminished in full conversion devices, where the entire emission power of the LED is converted to visible light. Efficient full-conversion devices can be built using high efficiency near-UV emitting LEDs and UV-excited phosphors. Therefore, EPD of thicker phosphor layer was desirable to obtain full conversion. In the case of micron-sized phosphors, it is hard to get a thick layer sometimes due to the fast settling of powders at a short time. It still remains an open challenge to optimize the EPD parameters and electrode to obtain thicker layer to be used for the scale-up EPD and high efficiency LEDs product in industry. Also, studies of the packing and ways to decrease the phosphor layer thickness for full conversion are needed.

Third, the deposition rates of micron-sized phosphors agreed well with those calculated from the Hamaker equation, except for the nitride phosphor. The nitride (red) phosphor film was thicker compared to the silicate or phosphate phosphor films. It was observed that this phosphor remained in suspension longer compared to the other phosphors during the deposition. This resulted in a thicker deposit for the same deposition time, but the reason of this different state of suspension with the nitride phosphor is not understood. Therefore, more fundamental study on the different deposition rate of the phosphors with individual chemical composition would be necessary. It is desirable to search for the physical/chemical parameters such as chemical environment and particle surface topography that characterize the properties of EPD process with individual phosphors.